Kobe University Repository : Kernel

PDF issue: 2025-04-03

Quantum chemical and experimental study on halogenated copper phthalocyanine for organic photovoltaics application

Kuzumoto, Yasutaka

(Degree)
博士 (工学)
(Date of Degree)
2014-03-25
(Date of Publication)
2016-03-25
(Resource Type)
doctoral thesis
(Report Number)
甲第6085号
(URL)
https://hdl.handle.net/20.500.14094/D1006085

※ 当コンテンツは神戸大学の学術成果です。無断複製・不正使用等を禁じます。著作権法で認められている範囲内で、適切にご利用ください。

Doctoral Dissertation

博士論文

Quantum chemical and experimental study on halogenated copper phthalocyanine for organic photovoltaics application

有機太陽電池応用に向けたハロゲン化銅フタロシアニンに関する量子化学的および実験的研究

January, 2014

平成 26 年 1 月

Graduate School of Engineering, Kobe University

神戸大学大学院工学研究科

Yasutaka Kuzumoto

葛本　恭崇

Contents

1. Introduction

2. Quantum Chemical Calculation in Organic Electronics

3. Partially Fluorinated Copper Phthalocyanine toward Band Engineering for High-Efficiency Organic

Photovoltaics

4. Electronic Structure and Spectra of Fluorinated Copper Phthalocyanine Dimer: Quantum Chemical Study

5. Structural and Electrical Properties of Fluorinated Copper Phthalocyanine toward Organic Photovoltaics: Post-Annealing Effect under Pressure

Chapter 1

Introduction

1.1 Background

Today, human economic activities are based on the usage of underground resources such as coal, oil, and natural gas. As these resources are exhaustible, a human life dependent on these energy resources causes collapse of the world economy corresponding depletion of underground resources in the future. Therefore, renewable energy has recently received broad attention. Renewable energy is defined as energy that comes from resources which are continually replenished. Sunlight, wind, tides, waves, geothermal heat, etc. are included in renewable energy resources. Among the renewable energy resources, sunlight is utilized as photovoltaic power generation. The solar energy is enormous enough to cover the total energy of annual human activities by one-hour sunlight energy. Furthermore, photovoltaic generation is clean energy because carbon dioxide is not produced by solar panel during generating electricity. Owing to these features, photovoltaic generation has been drawing intense. Fig. 1.1 shows the expanding world market in photovoltaics.1) It is predicted that world market of photovoltaics continues to grow and become a ten trillion yen industry in 2020.

1.2 Organic photovoltaic cell

1.2.1 Position of organic photovoltaic cell in solar cells

In photovoltaic power generation, energy of sunlight is converted into electric energy through a photovoltaic device. There are many kinds of photovoltaics as shown in Figure 1.2. The history of best conversion efficiencies in each photovoltaic type are also shown in Fig. 1.3.2) Crystal silicon type photovoltaic device is most common type in the world. The relatively high conversion efficiency of solar power generation is achieved in crystal silicon type. On the other hand, disadvantage of crystal silicon type photovoltaic cell is requirement of usage of large amount high-purity silicon per unit area. That is, a thick absorption layer is needed to absorb solar light enough due to small absorption coefficient (about 10^3[1/cm]) of crystal silicon. In the past, although manufacturers have achieved to produce crystal silicon photovoltaic cell at low-cost by mass-production of silicon, it is hard to realize additional cost-cutting. Therefore, many manufacturers focus on development of high-efficiency crystal silicon photovoltaic cell. The bifacial photovoltaic cell with 24.7% efficiency fabricated by Panasonic Co., which is named HIT, is an excellent example.3)

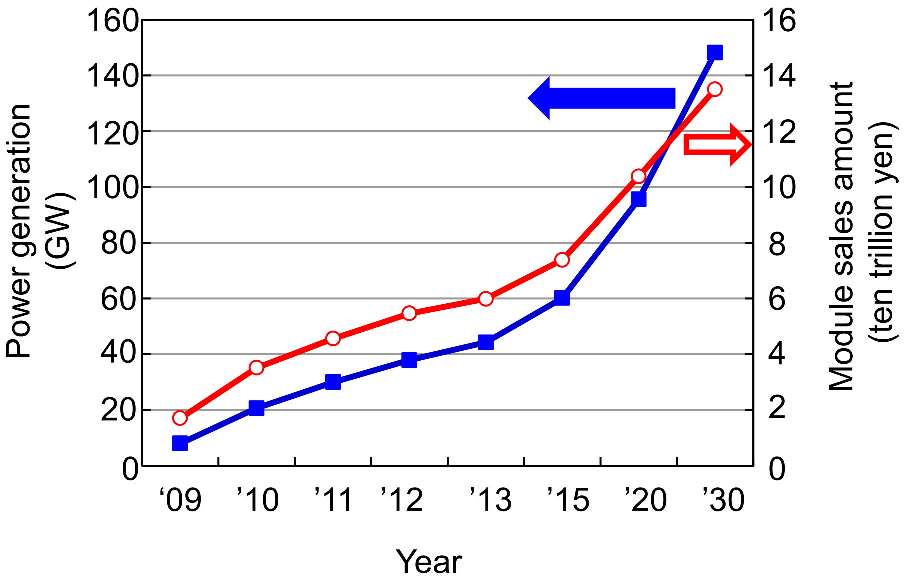

Fig. 1.1. World market in photovoltaics.1)

Thin film silicon type photovoltaic cell has the advantage of a small amount silicon usage due to enable to manufacture thin absorption layer. However, the much lower conversion efficiency (about 10%) as compared with single crystal silicon type leads to high manufacturing cost. Also, this type photovoltaic cell has a degraded behavior by light irradiation at a constant rate. Therefore, thin film silicon type is not widely used.

Among compound type photovoltaic cell, cadmium-tellurium (CdTe) type is sold at a very low price. First Solar Co., which is the manufacture of CdTe type photovoltaics, is price leader in photovoltaic cell sales companies. The manufacturing cost and conversion efficiency of CdTe photovoltaic module are 0.59 \$/W and 13.3% in the third quarter of 2013, respectively.4) Althrough CdTe type photovoltaic cell is not popular in Japan due to containing cadmium element, this type cell is popularized in the world. The Annual production in the world is more than 1 GW. The problem on CdTe type is that over several GW production per year is difficult because annual production of tellurium in the world is limited. The copper-indium-gallium-selenium (CIGS) type photovoltaic cell competes with CdTe type. The high conversion efficiency of CIGS (over 14 %) as compared with CdTe type is a merit of CIGS type. Since CIGS photovoltaic cell has the problem in shortage of indium element, indium-free copper-zinc-tin-sulfur (CZTS) type has also attracted attention.

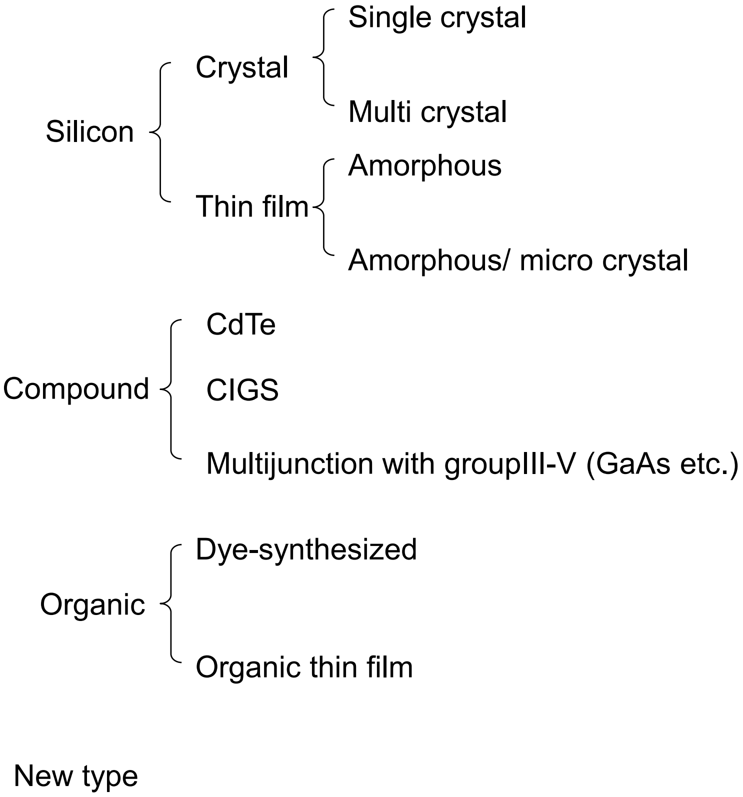

Fig. 1.2. Kinds of the photovoltaic cells.

There are two types of organic type cell. One is dye-synthesized type, and the other is organic thin film type. Dye-synthesized type is developed to improve the electric performance and durability toward commercial production. While the conversion efficiency in dye-synthesized type is about 11%, the conversion efficiency shows little improvement in these days. On the other hand, there is outstanding progress in organic thin film type as shown in Fig. 1.3. Although the conversion efficiency in organic thin film type was only about 5% in five years ago, now it has achieved 12%. Therefore, many institutions have great attention for organic thin film type photovoltaic cell. In this thesis, the photovoltaic cell of organic thin film type is described as organic photovoltaic (OPV) cell. Detail about OPV cell is described in from section 1.2.2 through 1.2.5.

Besides the photovoltaic cells mentioned above, some new type photovoltaic cells have been developed in these days. Quantum dot type is one of the typical new type photovoltaic cell. In this type, absorption layer containing the regularly-aligned quantum dots is used. Over 70% of theoretical limited efficiency is reported.5) Quantum dot type photovoltaic cell is developed in laboratories.

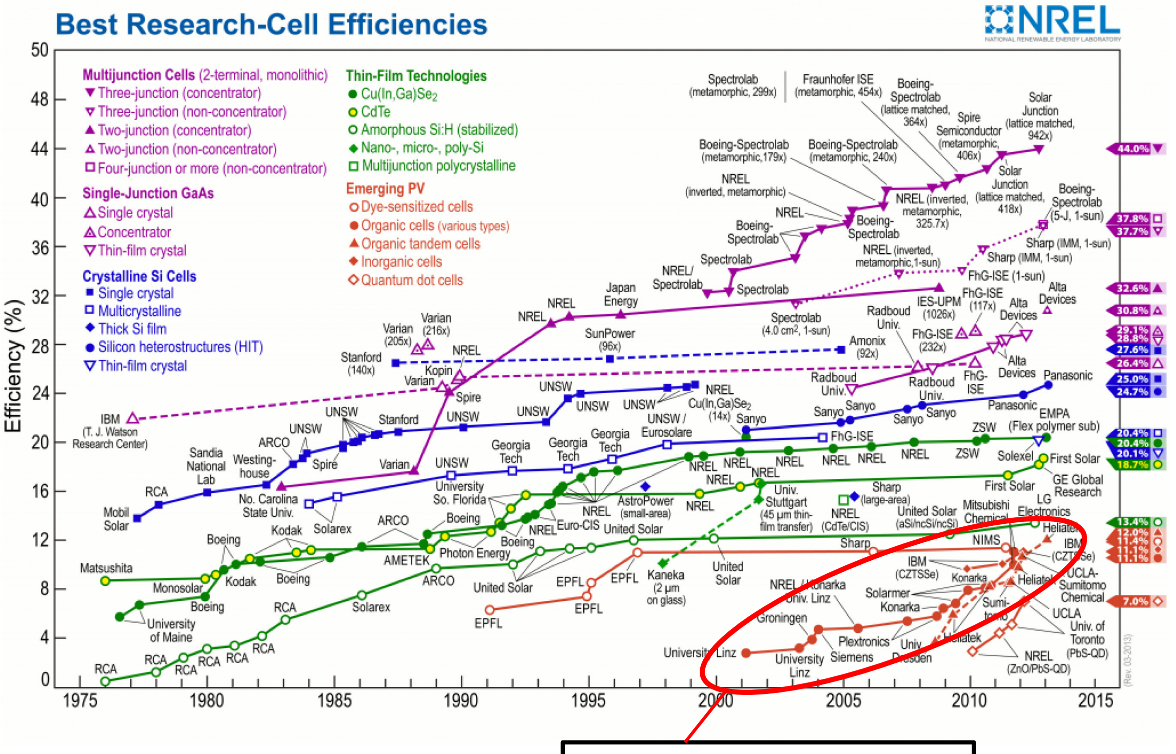

Organic thin film type

'13/01 12.0%(Heliatek, Germany)
'12/09 11.7%(Sumitomo Chemical, Japan)

Fig. 1.3. Improvement history of conversion efficiency in photovoltaic cells.2)

1.2.2 Brief development history of organic photovoltaic cell

Figure 1.4 shows brief development history of OPV cell. Photovoltaic effect by organic semiconductor material was shown by Kearns and Calvin in 1958.6) Their simple Schottky type photovoltaic system with single organic layer showed lower than 0.1% conversion efficiency. In 1968, Tang fabricated organic thin film with double organic layer consisting of a deposited copper phthalocyanine layer as electron donor (p-type) and a deposited perylene derivative layer as electron acceptor (n-type).7) The fabricated p-n heterojunction type OPV cell showed about 1% conversion efficiency. This is the first breakthrough in organic photovoltaics. Not only low-molecular-weight molecule but also polymer was adopted for p-n heterojunction type.8) Researches in the 1990s have revealed that the interdigitation of p- and n- layer is effective to increase conversion efficiency in OPV cell. Hiramoto et al. fabricated the three-layered OPV cell with an interlayer of co-deposited pigments of p-type metal-free phthalocyanine and n-type perylene derivative in between the respective pigment layers.9) This type has been called p-i-n type. P-i-n type is generally used for low-molecular-weight molecules due to make the organic layer by deposition. The electron donor and acceptor in bulk heterojunction type are also mixed together. Bulk heterojunction type is generally used for polymer organic photovoltaic cell because the organic layer is fabricated by wet process. Over 5% conversion efficiency was achieved by both p-i-n type and bulk heterojunction type OPV cells in the mid-2000s.10,11) Nowadays, the researches about improvement of durability have been studied. The introduction of TiO_x layer as an effective blocker leads to suppress the degradation of conversion efficiency in air.12) As improving of conversion efficiency and durability, there has been a growing interest in OPV cell. Furthermore, the considerable attention has leads to improve the performance of OPV cell.. Recently, the conversion efficiency of OPV cell has been improved up to about 12%.2) Toward the practical use of OPVs, further development to improve the performance of OPV cell including the manufacturing method to fabricate OPVs at low-cost is performed.

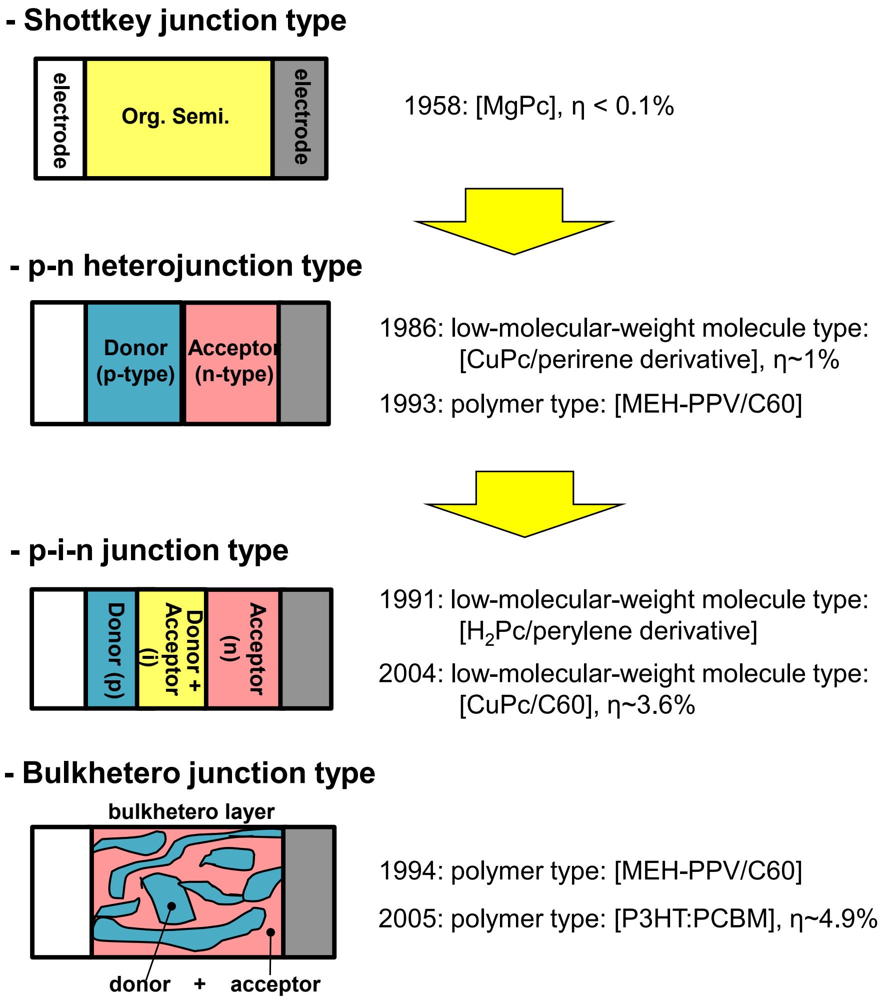

Fig. 1.4. Brief development history of organic photovoltaic cell.

1.2.3 Characteristics of organic photovoltaic cell

OPV cell is expected to realize new type device with features such as flexible, lightweight, colorful, and low-cost manufacturing. From these characteristics, future development of OPV cell as a new market developer is expected.

Organic molecules have a weak attraction for each another, known as van der Waals attraction. Therefore, organic layer composed of many organic molecules has durability for bending or stretching force. Also, as compared with silicon, the absorption coefficient of organic materials and the mass of constituent element in organic molecule are larger by about two orders of magnitude and lighter, respectively. It is possible to realize lightweight device using thin organic layer due to the light-weight property of a constituent elements. In Addition, the absorption spectra of organic materials is intrinsic to each organic material. Therefore, the realization of a novel device such as colorful photovoltaic cell is expected. Furthermore, manufacturing cost of OPV cell is expected to be inexpensive due to the low temperature in fabrication process as compared with inorganic photovoltaic cell and due to availability of wet process in organic layer fabricating.

On the other hand, the most important problem to realize a practical use of organic photovoltaics is durability. Organic materials tend to degrade rapidly than inorganic materials. This degrade is presumably due to oxidation of organic materials caused by oxygen or water in air. In the future, it is expected to develop new application using these novel characteristics of organic materials through overcoming the problem for development.

1.2.4 Operating principle of organic photovoltaic cell

The operating principle of OPV cell is fundamentally same with inorganic photovoltaic cells. In case organic semiconductor showing rectification property is used as absorption layer, current-voltage characteristics of under light irradiation in OPV cell shows current-voltage curve moved parallel of current-voltage curve under dark condition. Figure 1.5 shows working principle of OPV cell. Photoelectric conversion in OPV cell consists of 5 steps; (1) light absorption and exciton generation; (2) diffusion of exciton; (3) exciton dissociation and charge separation at hetero interface; (4) charge transfer to electrode; (5) charge collection at electrode. (1) Photovoltaic conversion in an OPV cell begins with the process of light absorption in an organic semiconductor layer. The incident light energy, which is larger than the HOMO–LUMO gap of an organic layer, causes an exciton generation in an organic semiconductor layer. (2) Generated exciton moves to the donor-acceptor (p-n) junction interface by diffusion. (3) An exciton is dissociated into a free carrier of hole and electron at the p-n hetero interface. (4) A charge carrier is moved to the electrodes by both of internal electric field and diffusion. Lastly, (5) A charge carrier is derived from electrode to external circuit.

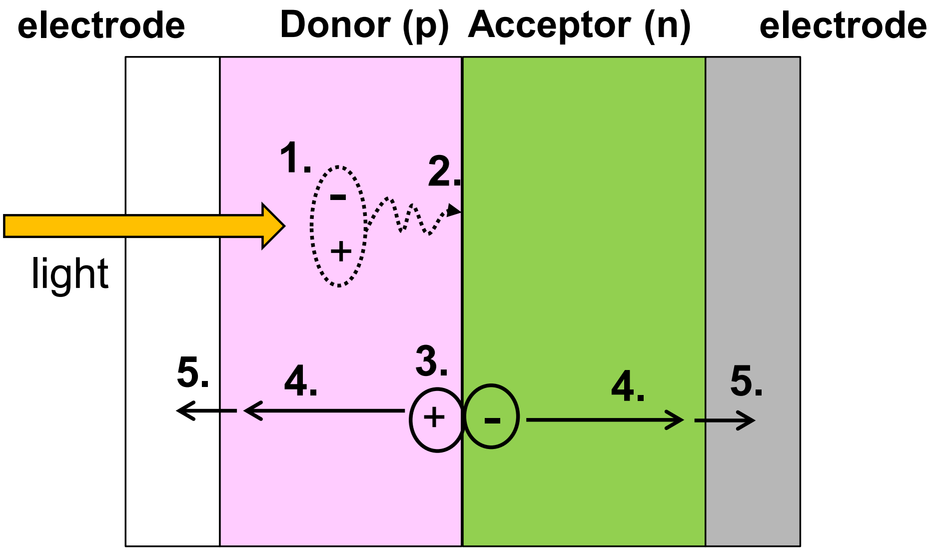

Fig. 1.5. working principle of organic photovoltaic cell.

1.2.5 Strategy for high efficiency organic photovoltaic cell

The typical problems in OPV cell are durability, high resistivity, large exciton binding energy, relatively large band gap, and insufficient energy control related to carrier injection at organic-electrode interface.

The durability is one of the most important problem to realize a practical use of OPV cell. As mentioned at section 1.2.3, organic materials tend to degrade probably due to oxidation caused by oxygen or water in air. Recently, some durable organic materials are developed to overcome the durability problem of organic devices.13-15)

The organic semiconductor materials generally have much higher resistivity than inorganic semiconductor materials. As thick organic semiconductor layer in an OPV cell leads to reduce the current derived from an OPV cell, an OPV cell with a thicker organic layer leads to decrease the performance. The typical organic layer thickness is around 100 nm. The organic materials with large intermolecular or intramolecular interaction are possible to lead to increase the conductivity.

On the other hand, an exciton in an organic layer has much larger binding energy than a inorganic layer because of the low permittivity of organic materials. Due to the large exciton binding energy, an exciton in an organic layer is not able to dissociate at room temperature and the diffusion length is generally shorter than 10 nm. Therefore, an exciton is often inactivated in an organic layer before an exciton reaches to the p-n junction interface. To solve this problem, besides the development of organic materials with low permittivity, there is structural solution method. The structure toward a resolution has large amount of p-n junction interface within the diffusion length of an exciton. Typical structures are p-i-n junction type and bulkhetero junction type structures. The structure with further large amount of p-n junction interface is possible to lead to further improvement of the OPV cell's performance.

There are few organic materials having small HOMO-LUMO band gap corresponding to red or infrared wavelength region. This is because of the instability of small band gap organic materials. The donor-accepter type molecular structure is expected to increase the stability with small band gap molecule due to the separation of the donor part, which has the most orbital coefficients of LUMO, from the acceptor part, which has the most orbital coefficients of HOMO.

The interface between an organic layer and an electrode plays an important role in OPV device performance. Typically, energy control of metal to improve the charge carrier injection is very important problem. Since the modification of a metal electrode with polar molecules leads to change the work function of a metal electrodes,16-21) electrode modification in organic devices by organic monolayer has been often used to improve the charge carrier injection between an organic layer and a metal electrode.22-27)

1.2.6 Organic semiconductor materials and fabrication methods in organic photovoltaic cell

Organic semiconductor materials can be grouped into low-molecular-weight molecular materials and polymer materials. Figure 1.6 shows the typical organic semiconductor materials for OPVs. For low-weight molecular materials, phthalocyanine series materials such as metal-free phthalocyanine (H_2Pc) and copper phthalocyanine (CuPc) are typical p-type materials. Phtalocyanine series molecules generally have high thermal and chemical stability due to π-conjugated system, which is spread throughout the molecule. Thiophene oligomer, such as dicaynovinyl oligothiophene (DCV6T),28) or dinaphthothienothiophene (DNTT) derivatives are also sometimes used as p-type low-molecular-weight molecular materials.29) Fullerene C_{60} or C_{60} derivatives such as phenyl-C_{61}-butyric acid methyl ester (PCBM) are generally used for n-type low-weight molecular materials.[10,11)] Other examples of n-type low-molecular-weight molecular materials are halogenated phthalocyanines such as hexadecafluoro copper phthalocyanine ($F_{16}CuPc$) and perylene derivatives such as 3,4,9,10-perylenetetracarboxylic bis-benzimidazole (PTCBI).[7,30,31)]

On the other hand, for polymer materials, poly(3-alkylthiophene) (P3AT) as typified by poly(3-hexylthiophene) (P3HT) and 2-methoxy-5-(2-ethylhexyloxyl)-1,4- phenylenevinylene (MEH-PPV) and 2-methoxy-5-(3',7'-dimethyloctyloxy)-1,4-phenylenevinylene (MDMO)-PPV are often used as p-type materials.[8,32,33)] C_{60} derivatives are generally used instead of n-type polymer because C_{60} derivatives show excellent n-type performance and are capable of use of wet process.

The fabrication methods of organic semiconductor can be grouped into dry process and wet process. Thermal deposition is the common dry process method of thin-film fabrication for low-molecular-weight molecular materials. In thermal deposition, a source of materials is evaporated under vacuum. The pressure and the heating temperature of sources during deposition are generally lower than 10^{-2} Pa and lower than 500°C, respectively. The vapor of particles of organic materials is not interrupted the transfer from a material source to a target object due to vacuum condition. The patterning of an organic semiconductor layer is enabled to use shadow mask. The substrate heating during deposition often enables to improve the quality of a deposited thin-film due to the migration of objective materials. For polymer materials, wet process is generally used to fabricate thin-film. In wet process, there are several kinds of methods such as spin-coat method, screen printing, cast method, etc. Since spin-coat method often used in basic research, it is described here about spin-coat method. Organic materials are dissolved in solvent. Then, after a small amount of solution is applied on the center of a substrate, the substrate is rotated at high speed in order to spread the organic material in solution by centrifugal force. Lastly, the spin-coated layer is dried to remove the solvent. After spin-coat process, the substrate heating is often performed to improve the quality of spin-coated organic layer. A rotational speed during substrate spinning and a concentration of organic solvent lead to control of the thickness and the quality of organic layer. The pattering of an organic layer is performed by conventional photolithography technique or sometimes using the difference of the substrate surface tension between the coated region and the uncoated region.

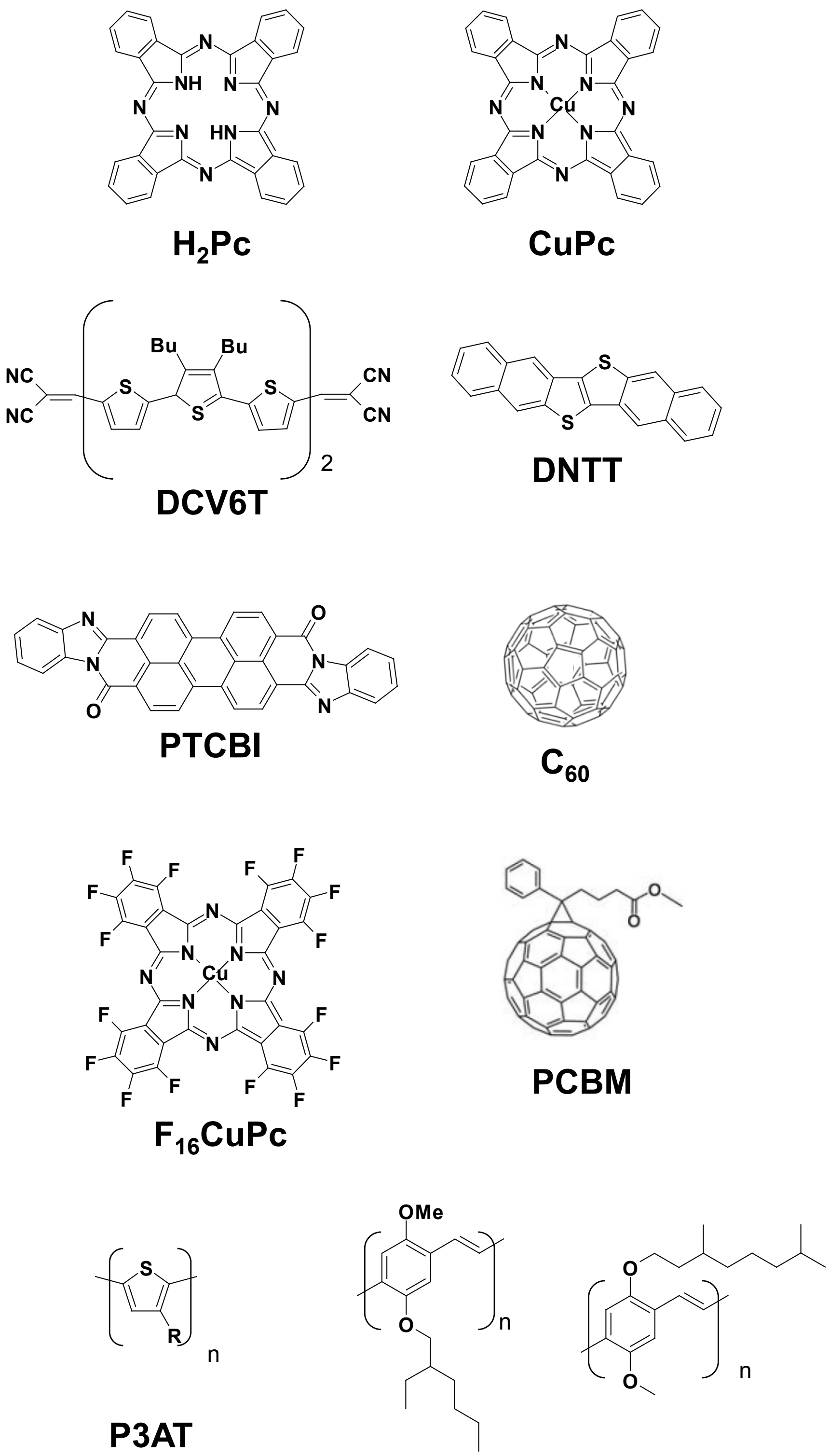

H_2Pc **CuPc**

DCV6T **DNTT**

PTCBI **C_{60}**

$F_{16}CuPc$ **PCBM**

P3AT
(P3HT: R = hexyl) **MEH-PPV** **MDMO-PPV**

Fig. 1.6. Typical organic semiconductor materials for organic photovoltaic cell.

1.3 Phthalocyanine series materials

1.3.1 Characteristics of phthalocyanine series materials

Unsubstituted phthalocyanine series molecules, such as H_2Pc, CuPc, zinc phthalocyanine (ZnPc), lead phthalocyanine (PbPc), tin phthalocyanine (SnPc), etc. are typical p-type material. Phtalocyanine series molecules generally have high thermal and chemical stability due to the π-conjugated system, which is spread throughout the molecule. This is a great advantage of phthalocyanine series molecules for organic devices because the important problem in organic devices is stability of organic materials. The unsubstituted phthalocyanines are generally colored with blue or green due to the large light absorption coefficients between 600 and 700 nm. Therefore, phthalocyanines are used as pigments or dyes with blue or green color. A Color filter is an application example as dyes. Furthermore, phthalocyanines are used for optical information recording media, nonlinear optical materials, sensors, recording material, organic thin film transistor, OPVs, etc. In phthalocyanines, Copper phthalocyanine is a well-known p-type semiconductor material.[7,34)] Due to its relatively high carrier mobility and durability, CuPc has been studied for thin film transistors and OPVs.

Figure 1.7 shows one of typical synthesis route of phthalocyanines.[35)] In this method, phthalonitrile is used for starting material. The phthalocyanine is synthesized by reaction of phthalonitrile with metal salt. The fine phthalocyanine is obtained in this method though it is expensive to produce because the price of phthalonitrile is relatively high. Therefore, phthalocyanines, which are synthesized by this method, are mainly used for research application.

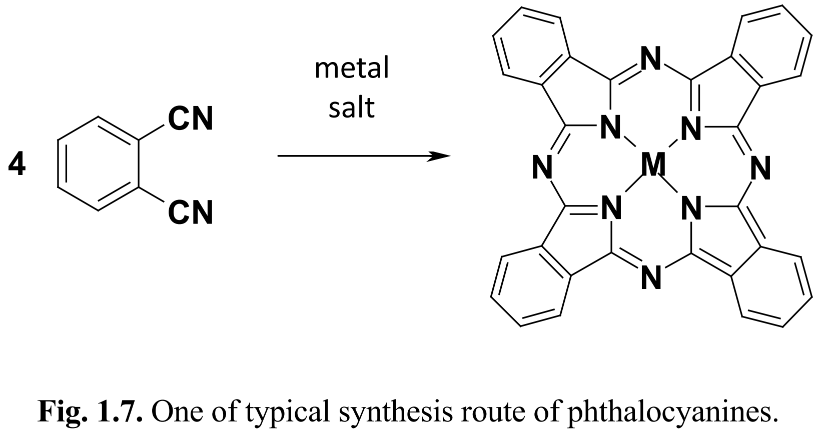

Fig. 1.7. One of typical synthesis route of phthalocyanines.

1.3.2 Halogenation of phthalocyanine

A modification of phthalocyanine is effective technique to change its properties. A substitution of the peripheral hydrogen of phthalocyanines by alkyl chain has been reported to improve the solubility of phthalocyanines in organic solvent.36) On the other hand, halogenation of phthalocyanines is very effective technique to improve the electronic properties of phthalocyanines. While CuPc shows blue color, hexadecachlorinated CuPc is known as green pigment.37) This indicates that the HOMO-LUMO band gap is changed by chlorine substitution. Furthermore, halogenation at the benzene ring leads to a decrease in the energy level.38-42) Figure 1.8 shows the calculation results about the HOMO and LUMO energy level dependence in copper phthalocyanine molecule by halogenation. In this calculation, the peripheral hydrogens in a copper phthalocyanine are fully substituted by halogen atoms. The HOMO and LUMO energy values are obtained from quantum chemical calculation with B3LYP/LanL2DZ level. The result indicates that each halogenation leads to decrease the HOMO and LUMO energy level as compared with unsubstituted phthalocyanines and also indicates that fluorination is the most effective to decrease the energy level in halogenation. Additionally, it is reported that the HOMO and LUMO energies of partially halogenated copper phthalocyanine are intermediate between unsubstituted and fully halogenated copper phthalocyanines, respectively.43) This calculation result indicates that fluorination is the most effective technique to tune the energy levels extensively. In this thesis, we focus on the halogenated copper phthalocyanine, especially fluorinated copper phthalocyanine.

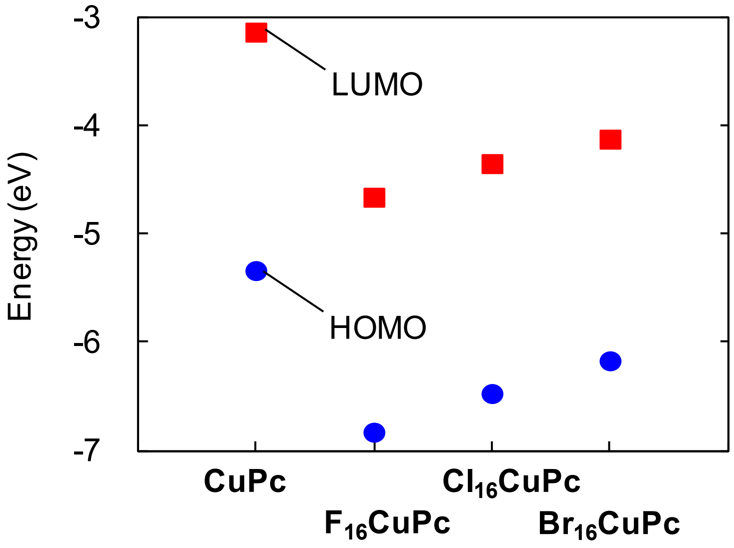

Fig. 1.8. Calculated HOMO and LUMO energy levels of halogenated copper phthalocyanine.

There are two basis methods to synthesize halogenated phthalocyanines. One approach is to modify an already existing phthalocyanine core, and the other is to perform condensation reaction of an already substituted phthalocyanine precursors. The latter is generally used due to the facility of controlling number of substituents on target phthalocyanines. The reported synthesis methods of fluorinated ZnPc are shown in Fig. 1.9.44) Tetra-, octa-, and hexadeca-fluorinated ZnPc have been synthesized by cyclotetramerization of mono-, di-, and tetra-fluorinated phthalonitriles with zinc salts, respectively. The number and the position of chlorine atoms in chlorinated zinc phthalocyanine are controlled by the number and the position of chlorine atoms in chlorinated phthalonitriles. For phthalocyanines with other central metal and halogen atoms, it is expected that tetra-, octa-, and hexadeca-halogenated phthalocyanices are similarly obtained. On the other hand, the synthesis of dodecafluoro ZnPc has not been shown in literature. This is presumably due to the instability of tri-fluorinated phthalonitriles. It is possibly associated with difficulty in synthesis of dodeca-halogenated phthalocyanines.

1.4 Purpose and outline of the thesis

The practical realization of OPV cell is expected due to their notable features. One of the issues for practical use of OPV cell is the durability of organic semiconductor materials. Therefore, development of stable organic materials including the improvement of their physical properties effectively contributes to a development of organic photovoltaics. However, although halogenated copper phthalocyanine is known as one of stable n-type organic semiconductor, the electrical properties of a device with them have been low level. The main purpose of this thesis is to investigate the potential of halogenated copper phthalocyanines, expecially fluorinated copper phthalocyanines, toward organic photovoltaics application. Additionally, electrode energy level tuning by electrode modification has been also investigated because the improvement of charge carrier transfer between an organic layer and an electrode is also important issue in OPV cells.

This thesis is structured in seven chapters. The simple outline of this thesis is shown in Fig. 1.10.

Chapters 1 and 2 are the introductory part in this thesis. In chapter 1 “Introduction”, brief introduction of OPV cells and phthalocyanine materials were presented as research background. Then, purpose and outline of the thesis were described.

In chapter 2 “Quantum Chemical Calculation in Organic Electronics”, the introduction of quantum chemistry and quantum chemical calculation are presented. Then, the methods of calculation used for this thesis are briefly explained. The correlation between calculation accuracy and calculation cost is also presented.

Chapters 3 through 6 are the main part in this thesis. The main part is divided into two parts. One is about an organic semiconductor for OPV cell and the other is mainly related the interface between an organic semiconductor and an electrode in OPV cell. The former is described in chapters 3, 4, and 5, and the latter is described in chapter 6. In chapter 3 “Partially Fluorinated Copper Phthalocyanine toward Band Engineering for High-Efficiency Organic Photovoltaics”, the electronic and vibrational structures of fluorinated CuPc have been investigated by quantum chemical calculation. It is revealed that the HOMO and LUMO energies, which play an important role for the efficiency of OPV cell, are systematically shifted with an increase or decrease in the number of fluorine atoms. The degree of the shift depends on the position of substitution of a hydrogen with a fluorine. The energies of a HOMO and a band-gap are also obtained spectroscopically. The spectroscopic energy values are compared with the calculated results.

In chapter 4 “Electronic Structure and Spectra of Fluorinated Copper Phthalocyanine Dimer: Quantum Chemical Study”, for fluorinated CuPc dimer, the electronic structures have been investigated. The influence of dimerization of a fluorinated CuPc molecule for spectroscopic properties has been also examined. The calculated results are compared with experimental properties.

In chapter 5 “Structural and Electrical Properties of Fluorinated Copper Phthalocyanine toward Organic Photovoltaics: Post-Annealing Effect under Pressure”, the structural and electrical properties of films with a fluorinated CuPc prepared under different conditions have been investigated. The results suggest that adequate substrate heating condition and post-annealing under additional pressure lead to improve the electrical properties of devices with a fluorinated CuPc layer.

In chapter 6 “Work Function of Gold, Silver, and Copper Surfaces Modified using Substituted Benzenethiols”, the work function of Au, Ag, and Cu surfaces modified with various substituted benzenethiols has been systematically investigated toward efficient design of organic electronic devices. The work function of each metal surface has varied according to a dipole moment of the substituted benzenethiol. The dependence of the reaction time and the concentration of a substituted benzenethiol for Au work function difference and the influence of substrate heating to a modified Au surface are also investigated.

In chapter 7 “Conclusions”, the results in thesis are summarized, and the conclusions of this thesis are described.

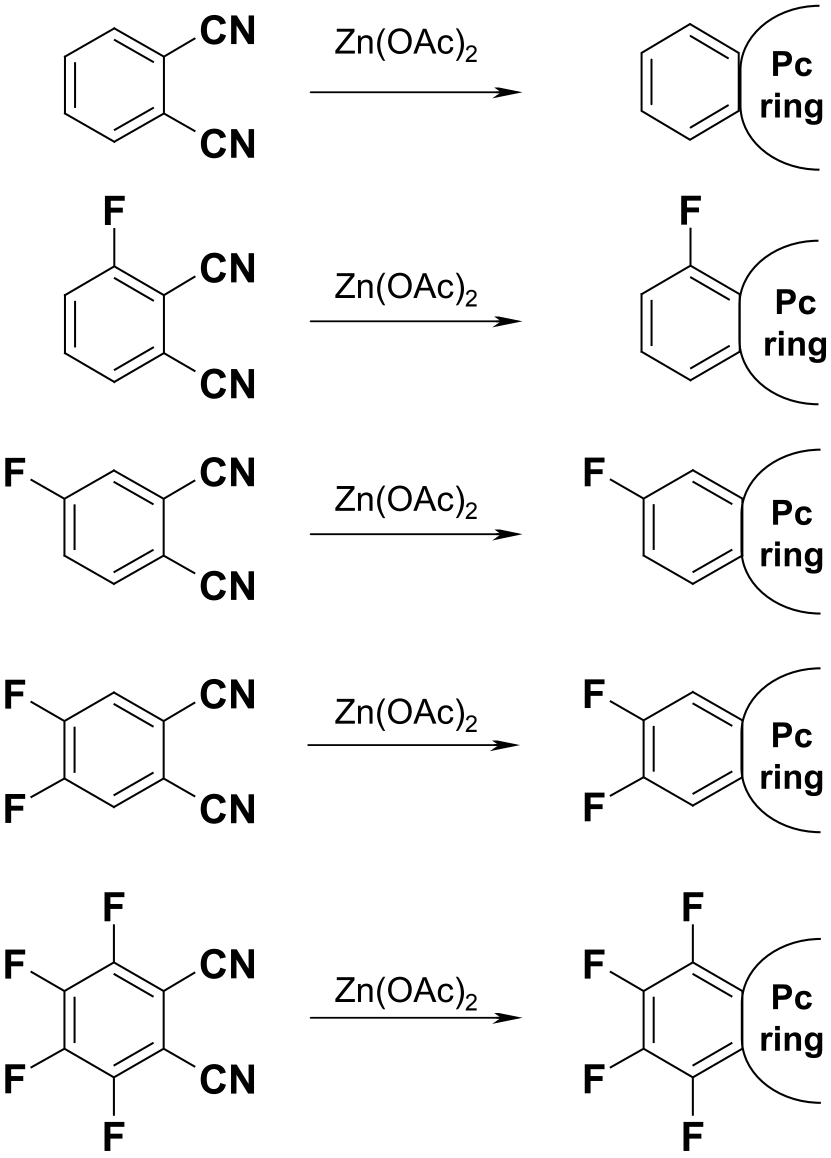

Fig. 1.9. Synthesis methods of zinc phthalocyanine and tetra-, octa-, hexadeca-fluorinated zinc phthalocyanines.[44)]

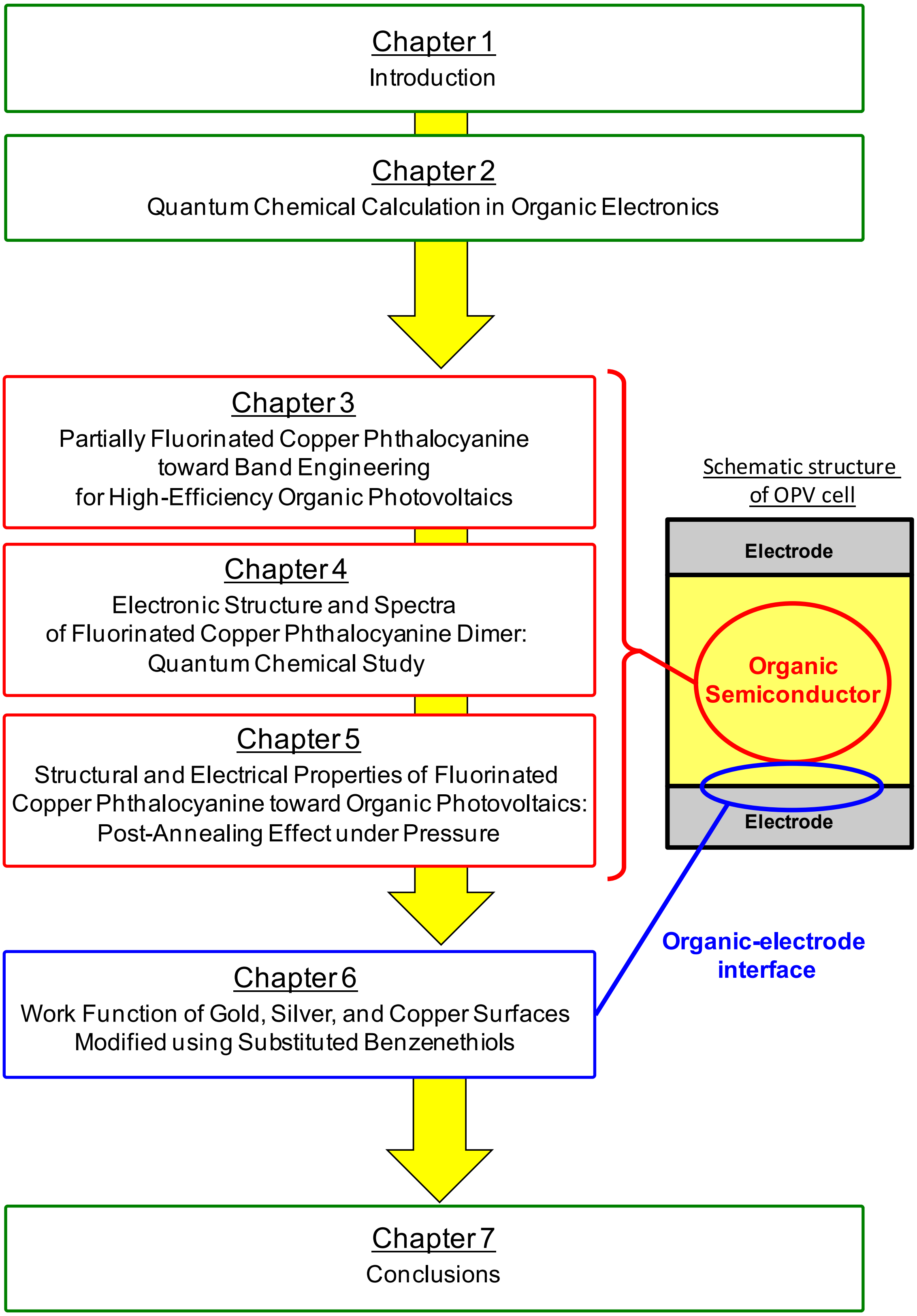

Fig. 1.10. Simple outline of this thesis.

1.5 References

1) S. Okubo: *Taiyoudenti 2012* (solar cell 2012) (Nikkei BP, Tokyo, 2012) pp.84 [in Japanese].
2) National Renewable Energy Laboratory., “Best research cell efficiency record”, http://www.nrel.gov/ncpv/
3) M. A. Green, K. Emery, Y. Hishikawa, W. Warta, and E. D. Dunlop: Prog. Photovolt: Res. Appl. **21** (2013) 827.
4) First Solar, Inc. Announces Third Quarter 201 Financial Results, http://investor.firstsolar.com/releasedetail.cfm?ReleaseID=803279
5) T. Nozawa and Y. Arakawa: Appl. Phys. Lett. **98** (2011) 171108.
6) D. Kearns and M. Calvin: J. Chem. Phys. **29** (1958) 950.
7) C. W. Tang: Appl. Phys. Lett. **48** (1986) 183.
8) N. S. Sariciftci, D. Braun, C. Zhang, V. I. Srdanow, A. J. Heeger, G. Stucky, and F. Wudl: Appl. Phys. Lett. **62** (1993) 585.
9) M. Hiramoto, H. Fujiwara, and M. Yokoyama: Appl. Phys. Lett. **58** (1991) 1062.
10) J. Xue, B. P. Rand, S. Uchida, and S. R. Forrest: Adv. Mater. **17** (2005) 66.
11) M. R-. Reyes, K. Kim, and D. L. Carroll: Appl. Phys. Lett. **87** (2005)083506.
12) A. Hayakaywa, O. Yoshikawa, T. Fujieda, K. Uehara, and S. Yoshikawa: **90** (2007) 163517.
13) K. Takimiya, H. Ebata, K. Sakamoto, T. Izawa, T. Otsubo, and Y. Kunugi: J. Am. Chem. Soc. **128** (2006**)** 12604.
14) T. Yamamoto and K. Takimiya: J. Am. Chem. Soc. **129** (2007) 2224.
15) M. J. Kang, I. Doi, H. Mori, E. Miyazaki, K. Takimiya, M. Ikeda, and H. Kuwabara: Adv. Mater.**23** (2011) 1222.
16) S. H. Kim, J. H. Lee, S. C. Lim, Y. S. Yang, T. Zyung: Jpn. J. Appl. Phys. **43** (2004) L60.
17) B. H. Hamadani, D. A. Corley, J. W. Ciszek, J. M. Tour, and D. Natelson: Nano Lett. **6** (2006) 1303.
18) X. Cheng, Y.-Y. Noh, J. Wang, M. Tello, J. Frisch, R.-P. Blum, A. Vollmer, J. P. Rabe, N. Koch, and H. Sirringhaus: Adv. Funct. Mat. **19** (2009) 2407.
19) P. Marmont, N. Battaglini, P. Lang, G. Horowitz, J. Hwang, A. Kahn, C. Amato, and P. Calas: Org. Electron. **9** (2008) 419.

20) B. de Boer, A. Hadipour, M. M. Mandoc, T. van Woudenbergh, and P. W. M. Blom: Adv. Mater. **17** (2005) 621.
21) L. Zhu, H. Tang, Y. Harima, K. Yamashita, D. Hirayama, Y. Aso, and T. Otsubo: Chem. Commun. **18** (2001) 1830.
22) D. J. Gundlach, L. Jia, and T. N. Jackson: IEEE Electron Device Lett. **22** (2001) 571.
23) S. K. Park , T. N. Jackson, J. E. Anthony, D. A. Mourey: Appl. Phys. Lett. **91** (2007) 063514.
24) M. Kitamura, Y. Kuzumoto, S. Aomori, M. Kamura, J. H. Na, and Y. Arakawa, Appl. Phys. Lett. **94** (2009) 083310.
25) J.-P. Hong, A.-Y. Park, S. Lee, J. Kang, N. Shin, and D. Y. Yoon, Appl. Phys. Lett. **92** (2008) 143311.
26) M. Kitamura, Y. Kuzumoto, W. Kang, S. Aomori, and Y. Arakawa, Appl. Phys. Lett. **97** (2010) 033306.
27) L.-W. Chong, Y.-L. Lee, T.-C. Wen, and T.-F. Guo, Appl. Phys. Lett. **89** (2006) 233513.
28) M. Riede, C. Uhrich, J. Widmer, R. Timmreck, D. Wynands, G. Schwartz, W. –M. Gnehr, D. Hildebrandt, A. Weiss, J. Hwang, S. Sundarraj. P. Erk, M. Pfeiffer, and K. Leo: Adv. Funct. Mater. **21** (2011)3019.
29) H. Mori and K. Takimiya: Appl. Phys. Express **4** (2011) 061602.
30) R. Ye, M. Baba, and K. Mori: Jpn, J. Appl. Phys. **44** (2005) L581.
31) Z. Bao, A. J. Lovinger, and J. Brown: J. Am. Chem. Soc. **120** (1998) 207.
32) G. Li, V. Shrotriya, J. Huang, Y. Yao, T. Moriarty, K. Emery, and Y. Yang: Nature Materials: **4** (2005) 864.
33) C. J. Brabec, F. Padinger, N. S. Sariciftci, and J. C. Hummelen: **85** (1999) 6866.
34) P. E. Fielding and F. Gutman: J. Chem. Phys. **26** (1957)411
35) P. Gregory: J. Porphyrins Phthalocyanines **3** (1999) 468.
36) E. A. Cueller and T. J. Marks: Inorg. Chem. **20** (1981) 3766.
37) M. –M. Ling, Z. Bao, and P. Erk: Appl. Phys. Lett. **89** (2006) 163516.
38) X. Cai, Y. Zhang, X. Zhang, and J. Jiang: J. Mol. Struct.: THEOCHEM **801** (2006) 71.
39) U. Weiler, T. Mayer, W. Jaegermann, C. Kelting, D. Schlettwein, S. Makarov, and D. Wöhrle: J. Phys. Chem. B **108** (2004)19398.

40) W. Chen, H. Huang, S. Chen, Y. L. Huang, X. Y. Gao, and A. T. S. Wee: Chem. Mater. **20** (2008) 7017.

41) C. Shen and A. Kahn: J. Appl. Phys. **90** (2001) 4549.

42) H. Peisert, M. Knupfer, and J. Fink: Appl. Phys. Lett. **81** (2002) 2400.

43) R. Murdey, N. Sato, and M. Bouret: Mol. Cryst. Liq. Cryst. **455** (2006) 211.

44) T. Mayer, U. Weiler, C. Kelting, D. Schlettwein, S. Makarov, D. Wohrle, O. Abdallah, M. Kunst, and W. Jaegermann: Sol. Energy Mater. Sol. Cells **91** (2007) 1873.

Chapter 2

Quantum Chemical Calculation in Organic Electronics

2.1 Introduction

2.1.1 Position of quantum chemical calculation in development of organic device

There are many kinds of organic compounds even as organic compounds are composed of a few kinds of element such as carbon, hydrogen, oxygen, nitrogen, and sulfur. This is attributed to a multitude of the chemical bonding pattern in organic compounds. Also, physical properties of an organic compound differ from others and even from the similar organic compounds with the exception of the chemical bonding pattern. This suggests that small molecular structural change in organic compounds have possibility to leads to excellent physical properties. Therefore, organic compounds have potential to realize remarkably useful materials or organic devices. To develop organic compounds and organic devices, the prediction of physical properties of organic compounds is very important. However, there has been a difficulty to predict the physical properties of unknown organic compounds. Recently, quantum chemical calculation, which is the calculation based on quantum chemistry, plays a role to reduce the difficulty in the prediction of organic compounds. In the past, it is difficult to perform the quantum chemical calculation with a high degree of accuracy because of lack of the performance of computer for calculation. However, recent computer development makes it possible for higher accuracy calculation than in the past. Also, the development of software technique leads to facilitate a usage of quantum chemical calculation. Therefore, to develop the organic materials and organic devices, quantum chemical simulation has been used by many institutions and it is almost indispensable for researcher in these days.

Figure 2.1 shows the simple flow image of the development using quantum chemical calculation in an organic compound and/or an organic device. An organic compound/device is designed on the basis of a theory. Then, the objective properties are predicted by calculation.

In case the expected properties are roughly obtained, the organic compound/device is once fabricated. Property evaluation and analysis of a fabricated compound/device are implemented. Then, improved organic compound/device based on the analysis results is designed again. After that, the property prediction by calculation is performed again. The development of organic compound/device is proceeded in this way.

In this chapter, the brief history of quantum chemistry is introduced. Then, the examples of physical properties of organic compounds obtained by quantum chemical calculation are presented. The relationship between calculation cost and calculation accuracy is also described. Lastly, the calculation methods used in this thesis are briefly explained.

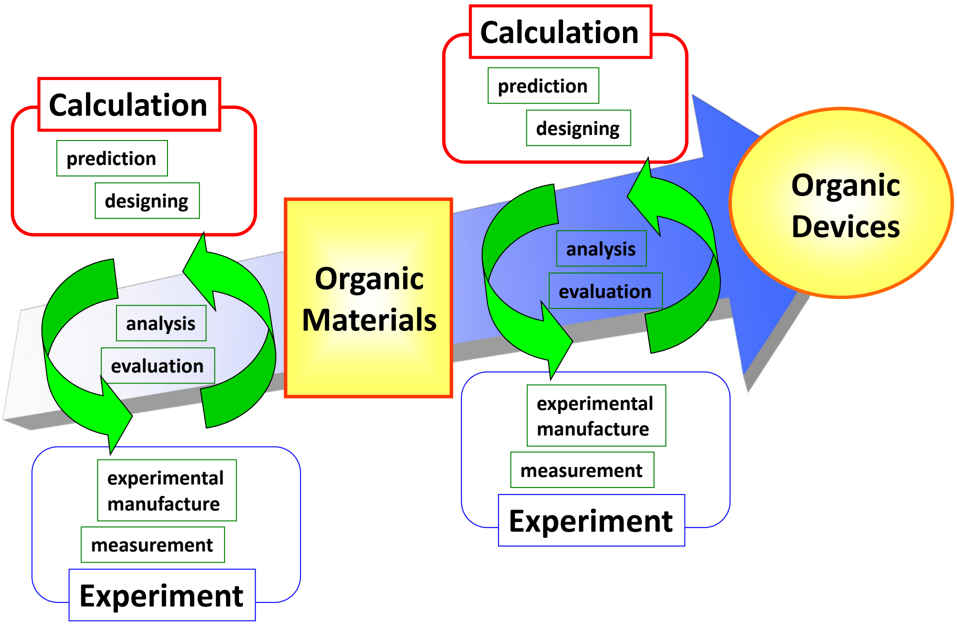

Fig. 2.1. Simple organic materials/devices development flow using quantum chemical calculation.

2.1.2 Brief development history of quantum chemistry

Figure 2.2 shows the brief history in quantum chemistry. Quantum chemistry, which is applied the quantum mechanics for chemistry, has been developed to clarify the chemical event based on the quantum mechanical principle. Therefore, quantum chemistry has its roots in shrödinger equation published by shrödinger in 1926. The following year, Heitler and

London explained the covalent bond in hydrogen molecule quantum mechanically.(1) This success is said to be the beginning of the quantum chemistry. Then, basic theories of calculation and analysis methods in quantum chemistry were developed by about the 1960's. For calculation method, Slater and Pauling much further developed the valence bond theory,(2,3) which has its roots in Heitler and London theory.(1) In valence bond theory, the electron pair is assigned at individual bond in molecule. At roughly the same time, Mulliken, Hund, Huckel developed the molecular orbital theory.(4-7) In contrast to valence bond theory, the electrons in the molecule are not assigned to individual bonds but moving in the whole molecule in molecular orbital theory. In 1964, Hohenberg-Kohn theorems, which serve as a foundation for density functional theory, was published.(8) In the density functional theory, the properties of a many-electron system can be determined by using electron density in ground state. For analytical method, Fukui published the frontier orbital theory in 1952.(9) In frontier orbital theory, the frontier orbitals (the highest occupied molecular orbital, HOMO, and the lowest unoccupied molecular orbital, LUMO) have an especially important role in two molecules interaction. Also, in 1965, Woodward and Hoffmann devised the Woodward-Hoffmann rule.(10) This rule is applied to explain the stereospecificity in chemical reaction based upon conservation of symmetry in chemical reaction. Quantum chemistry was developed by these theories. Furthermore, not only the progression of theories but also computer advancement greatly contributed to the development of the quantum chemistry. In quantum chemistry, even in case of very simple system, it is difficult to perform the quantum chemical calculation by hand due to heavy computational effort. The advancement of the computer performance in these days has enabled to handle a lot of amount of calculation in large and complicated system in short time. Today, quantum chemistry makes further progress by development of theories in quantum chemistry and advancement of computer performance.

2.1.3 Properties of organic materials obtained from quantum chemical calculation

Various physical properties of organic materials are obtained by quantum chemical calculation. From among the physical properties, a stable molecular structure on ground state, the molecular orbital on a stable molecular structure, an electric dipole moment, and an absorption spectra are briefly explained in this section. These properties are calculated and discussed in this thesis.

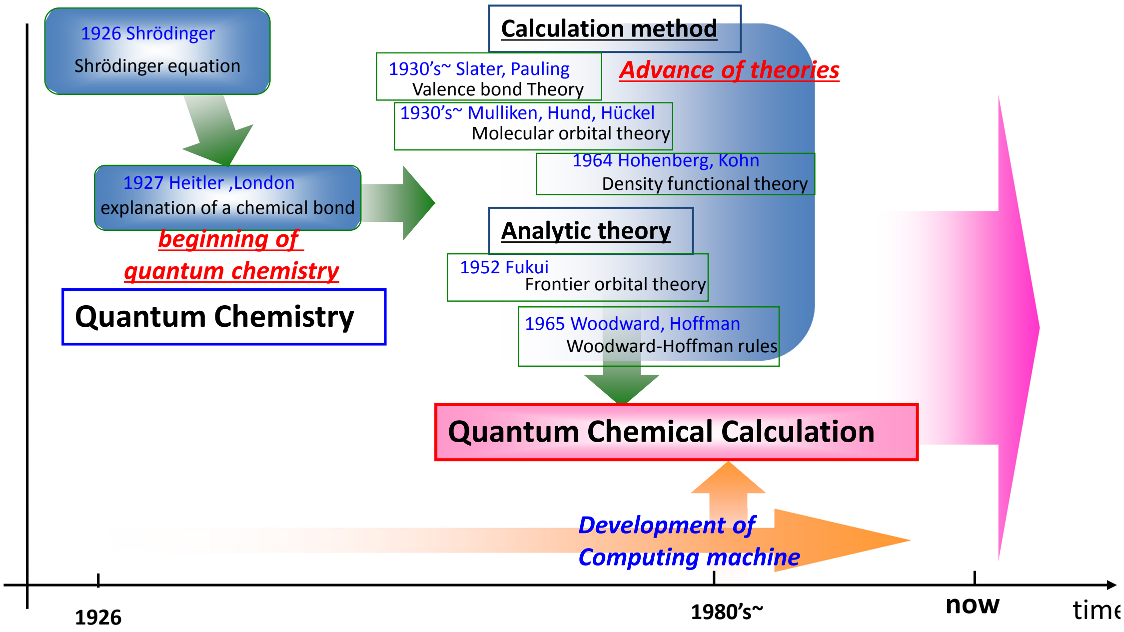

Fig. 2.2. Brief history of quantum chemistry.

A stable molecular structure, the molecular orbital in the stable molecular structure, and the electric dipole moment are obtained by calculation about molecular structure in the ground state. Figure 2.3 shows the brief flow chart to obtain a stable molecular structure. The process to obtain a stable molecular structure is described briefly as follows. First, input the initial coordinates of the atomic nuclei. The initial Hamiltonian and the initial wave functions (the molecular orbitals) are generated by the initial coordinates. Using self-consistent field (SCF) method, the optimal energy and the molecular orbital coefficients about the initial coordinates are solved by iterative procedure. The force, $\delta E/\delta Q$ is calculated by the obtained energy, where Q is the nuclei coordinates. In case the force is not zero, the nuclei coordinates are moved in the direction to decrease the force. Then, the newly nuclei coordinates are obtained. The cycle from input of the atomic nuclei coordinates to determination of the new coordinates is repeated until the force converges to zero. The nuclei coordinates with $\delta E/\delta Q = 0$ for all Q constitute the stable molecular structure. Also, the molecular orbitals in the stable molecular structure are correspondingly obtained because the molecular orbital coefficients about the provided coordinates are also solved in SCF process. The electric dipole moment μ are classically defined as

$$\mu = \sum_i q_i r_i,$$

where q_i and r_i are the charge amount of the charged particle numbered i and the coordinates of the charged particle numbered i, respectively, and quantum mechanically written as

$$\mu = -\int \Psi^* \sum_i \boldsymbol{r_i} \Psi \, d\boldsymbol{r} + \sum_A Z_A R_A \;\; ,$$

where Ψ, $-\sum_i \boldsymbol{r_i}$, Z_A, and R_A are the wave function of a molecule, the electron dipole moment operator, the charge amount of a nucleus numbered A, and the coordinates of a nucleus numbered A. Therefore, the electric dipole moment is calculated using the wave function of the molecule and the nuclei coordinates in the stable molecular structure.

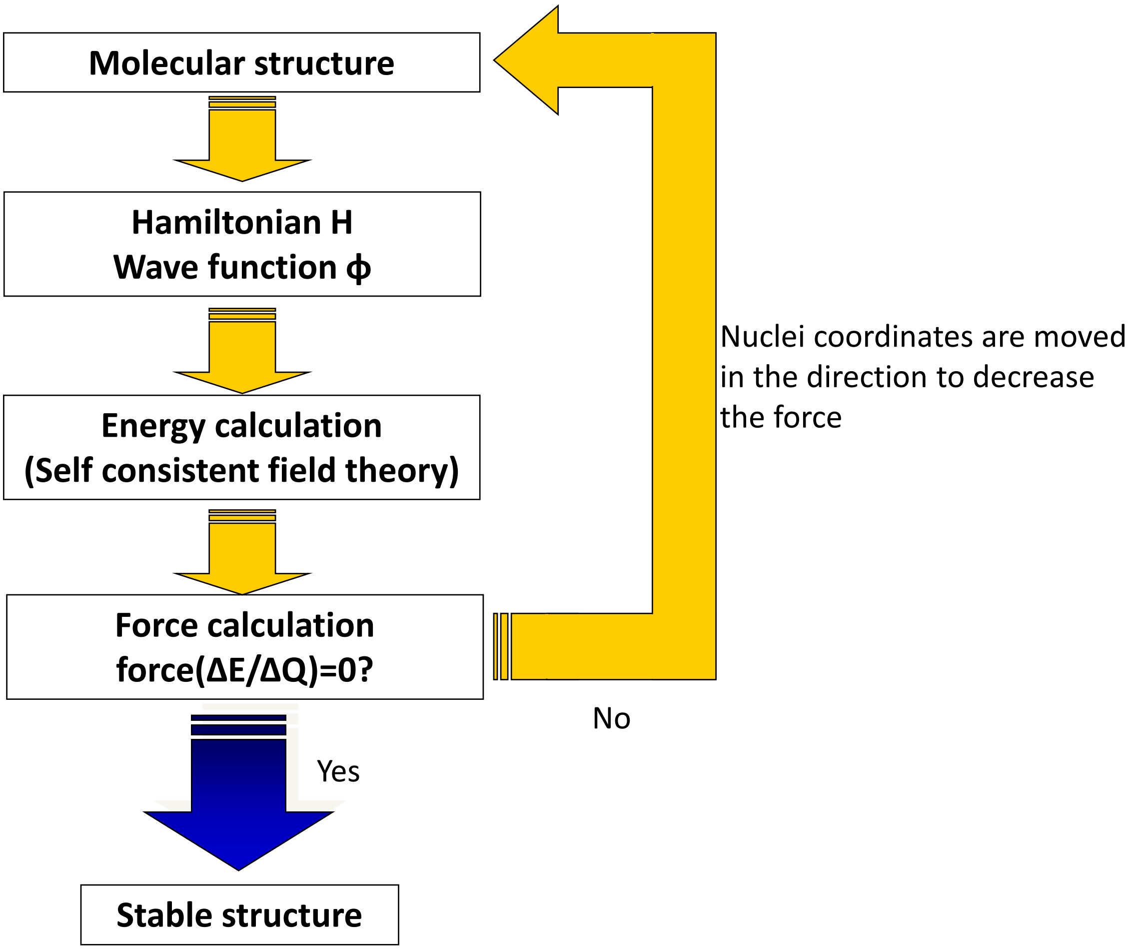

Fig. 2.3. Brief flow chart to obtain the stable molecular structure using quantum chemical calculation.

On the other hand, the electronic absorption spectra are calculated about the excited states of molecule. To obtain the properties of the excited states, the structure of the ground state serves as a starting point. First, the ground state stable structure is obtained as described above. Then, calculation method about excited states, such as configuration interaction method and time-dependent density functional method, are performed about a structure of ground state. In the configuration interaction method, the excited states are described by the replacement of occupied spin orbitals with unoccupied spin orbitals in slater determinant in ground state. In the time-dependent density functional method,11) the influence by external field is described using the energy functional in ground state. The change of the external potential are also assumed as linear response in this method. Using these methods, the properties about electric transition such as the excited energy, oscillator strength, and orbitals influenced to the transitions are obtained. As a result, the absorption spectra is simulated using the excited energy and the oscillator strength.

2.1.4 Accuracy and cost of quantum chemical calculation

In general, accuracy of quantum chemical calculations increase with increasing calculation cost. Both calculation accuracy and calculation cost increase in order of empirical methods, semi-empirical methods, and *ab initio* methods. Nowadays, empirical methods are not practically used because the cost of semi-empirical methods are considerably low due to recent computer advancement. The number of basis functions similarly influences. Figure 2.4 shows the correlation between accuracy and cost in quantum chemical calculation. The combination of high-cost and low-cost method enable to obtain high accuracy results effectively. The procedure to obtain high accuracy molecular structure is mentioned here as a typical example. At first, the structure optimizing by low accurate calculation method such as semi-empirical method is performed. This process leads to obtain roughly correct structure in a short time. Then, high accurate calculation about the roughly optimized structure is implemented. As a result, the structure with a high degree of accuracy is effectively obtained because the difference between roughly obtained structure and highly accurate structure is comparatively small. That is, the time to obtain the accurate structure is shortened. These multi-step process consisting of the combination of high and low accurate calculation method enable to reduce calculation cost.

2.2 Method of Calculation

Quantum chemical calculation is performed using some kinds of approximation due to a difficulty in obtaining a full quantum mechanical solution of a system involving a number of electrons around a number of atomic nuclei. A typical example of an approximation is the Born-Oppenheimer approximation, which is used in all calculation in this thesis. The Born-Oppenheimer approximation is the assumption that the electronic motion and the nuclear motion in molecules can be separated because a nuclear mass is much larger than electron's mass. Hartree-Fock method and density functional theory are typical calculation method in quantum chemistry.

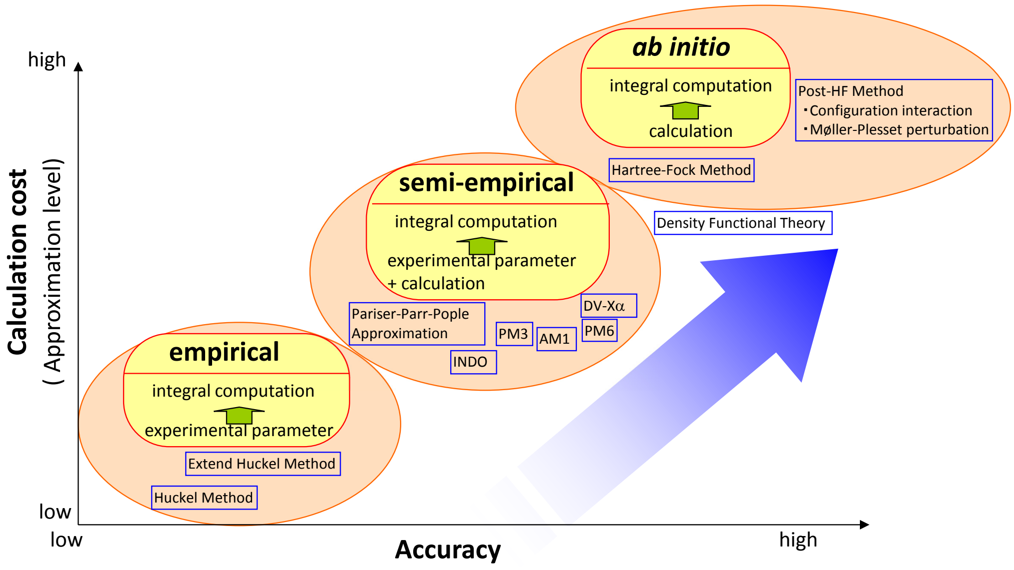

Fig. 2.4. Correlation between accuracy and cost in quantum chemical calculation.

2.2.1 Hartree-Fock Method

In Hartree-Fock approximation, the many-body wave function is written by a single Slater determinant of one-electron wave functions. The Hartree-Fock equation to assign an one-electron wave function ϕ to obtain energy extremum is given as

$$f(\mathbf{r})\,\phi_i(\mathbf{r}) = \varepsilon_i \phi_i(\mathbf{r}) \ ,$$

where $f(\mathbf{r})$ and ε_i are Fock operater and energy eigenvalue of wave function $\phi_i(\mathbf{r})$, respectively. The Fock operator is given by

$$\mathrm{f}(\mathbf{r}) = -\frac{\hbar^2}{2\mathrm{m}}\nabla^2 + \mathrm{v}(\mathbf{r}) + \sum_{\mathrm{j}}\left[J_j(\mathbf{r}) - K_j(\mathbf{r})\right].$$

The first and second term of the right side are one-electron operators and give the kinetic energy contribution and the electron-ion potential, respectively. The $J_j(\mathbf{r})$ in the third term is the coulomb operator, defining the repulsive force between two electrons. The $K_j(\mathbf{r})$ in the fourth term is the exchange operator, defining the quantum effect produced by exchanging two electrons. For actual calculation, one-electron wave functions are given by a linear combination of atomic orbitals. Then, the Hartree-Fock equation is represented by the Roothaan equations, which have a matrix-form. The Roothaan equations are solved using SCF method. The solution of the Roothaan equations describe the total electric energy E_0 as

$$E_0 = \sum_i \int \phi_i^*(\mathbf{r})\left(-\frac{\hbar^2}{2\mathrm{m}}\nabla^2 + \mathrm{v}(\mathbf{r})\right)\phi_\mathrm{i}(\mathbf{r})\mathrm{dr} + \sum_{i,j}\left(2\mathrm{J}_{\mathrm{ij}} - \mathrm{K}_{\mathrm{ij}}\right).$$

The first term of the right side is the one-electron (kinetic plus potential) energy. The second term of the right side is sum of the coulomb repulsion energy of the electrons and the exchange energy resulting from the quantum nature of electrons. The total energy E is represented as $E = E_0 + V$, where V is the nuclear repulsion energy.

The calculation methods to solve Hartree-Fock equation range from highly accurate to very approximate. *Ab initio* methods are based entirely on quantum mechanics and basic physical constants. Therefore, all integral calculations are performed without any substitution for empirical parameters. On the other hand, empirical and semi-empirical methods employ integral calculations by replacement of all and some integral calculations by empirical parameters, respectively. On semi-empirical method, the high-cost integral calculations such as two-electron integral are frequently substituted.

2.2.2 Density functional theory

Density functional theory is based on Hohenberg-Kohn theorem.8) From Hohenberg-Kohn theorem, the external potential is uniquely determined by the corresponding ground-state electronic density. Then, the wave function is uniquely corresponding to the electronic density through the external potential. Therefore, physical properties based on wave function are able to obtain from a given electronic density of ground state. Also, the energy of a system is given as a functional of the electronic density of the ground state. The electronic density that minimizes the total energy is the ground-state electronic density. This is the variational principle in case that a trial wave function is replaced by the electronic density. An actual calculation is based on Kohn-Sham equation

$$\left(-\frac{\hbar^2}{2\mathrm{m}}\nabla^2 + \mathrm{V}_{\mathrm{eff}}\right)\phi_{\mathrm{i}}(\mathrm{r}) = \varepsilon_{\mathrm{i}}\phi_{\mathrm{i}}(\mathrm{r}),$$

where $-\frac{\hbar^2}{2\mathrm{m}}\nabla^2$ and $\mathrm{V}_{\mathrm{eff}}$ are the kinetic energy operator and an external effective potential, respectively.[12)] Kohn-Sham equation is a representation of Shrödinger equation in a hypothetical system of non-interacting electrons in ground state. The external effective potential $\mathrm{V}_{\mathrm{eff}}$ is introduced to describe an actual electronic density as exactly as possible. To perform a quantum chemical calculation based on density functional theory, molecular orbitals $\phi_{\mathrm{i}}(\mathbf{r})$ are given as

$$\rho(\mathbf{r}) = \sum_{\mathrm{i}} |\phi_{\mathrm{i}}(\mathbf{r})|^2,$$

where $\rho(\mathbf{r})$ is the electronic density. Also, $\mathrm{V}_{\mathrm{eff}}$ is given as

$$\mathrm{V}_{\mathrm{eff}}(\mathbf{r}) = \mathrm{v}(\mathbf{r}) + \int \frac{\rho(\mathbf{r}')}{|\mathbf{r}-\mathbf{r}'|}\mathrm{d}\mathbf{r}' + \mathrm{V}_{\mathrm{xc}}(\mathbf{r}),$$

where $\mathrm{V}_{\mathrm{xc}}(\mathbf{r}) = \frac{\delta \mathrm{E}_{\mathrm{xc}}[\rho]}{\delta\rho}$ is the exchange-correlation potential. That is, $\mathrm{V}_{\mathrm{eff}}$ is described by a functional of an electronic density. The electron interactions are included in $\mathrm{V}_{\mathrm{xc}}(\mathbf{r})$. The total electric energy E_0 are obtained from Kohn-Sham equation as

$$E_0 = \sum_i \int \phi_i^*(\mathbf{r})\left(-\frac{\hbar^2}{2\mathrm{m}}\nabla^2\right)\phi_{\mathrm{i}}(\mathbf{r})\mathrm{dr} + \int \mathrm{v}(\mathbf{r})\rho(\mathbf{r})\mathrm{d}\mathbf{r} + J[\boldsymbol{\rho}] + E_{xc}[\boldsymbol{\rho}].$$

The first and second terms of the right side are the kinetic and potential energy, respectively. Also, the third and fourth terms of the right side are the coulomb interaction energy of the electrons and the exchange energy, respectively. Unfortunately, although the exact exchange energy leads to the exact electronic density, the exact exchange energy is unknown. Therefore, various approximated exchange energy is used.

2.3 Calculation level dependence of the accuracy and cost in phthalocyanine molecules

The information of calculation levels dependence of the accuracy and the cost is helpful to select the adequate calculation method on an objective system. Therefore, various calculations based on semi-empirical method, Hartree-Fock method, and density functional theory were performed to lead to the correlated information between calculation accuracy and cost in phthalocyanine molecules.

Figure 2.5 shows the molecular structure of copper phthalocyanine (CuPc), zinc porphyrin (ZnP), zinc phthalocyanine (ZnPc), zinc naphthalocyanine (ZnNPc), and the molecule substituted naphthalene part of ZnNPc with anthracene (ZnAPc), which are used for the calculation. For CuPc, the numbering of the atoms used to represent the positions of the bonds and the bond angles are included. We calculated the optimized structures of these molecules. For CuPc calculation, semi-empirical method PM6,13) Hartree-Fock (HF) method, and density functional method Becke three parameter exchange functional and Lee-Yang-Parr correlation functional (B3LYP) were used.14,15) From a minimal basis set sto-3G to high level basis set 6-311+G(2d,p) and basis sets including effective core potential (LanL2MB and LanL2DZ) were used. For the calculations on ZnP, ZnPc, ZnNPc, and ZnAPc, B3LYP was used with LanL2DZ basis set. All calculations were performed using the Gaussian 09 program package.16)

Table 2.1 Calculated bond lengths (in Å) and bond angles (in degree) of CuPc.

	HF					B3LYP				
	Bond length			Bond angle		Bond length			Bond angle	
Basis set	Cu-N$_1$	C$_1$-N$_1$	C$_\beta$- C$_\beta$'	C$_1$-N$_1$-C$_1$	C$_\alpha$-C$_\beta$-C$_\beta$'	Cu-N$_1$	C$_1$-N$_1$	C$_\beta$- C$_\beta$'	C$_1$-N$_1$-C$_1$	C$_\alpha$-C$_\beta$-C$_\beta$'
sto-3G	1.869	1.433	1.415	104.1	121.2	1.815	1.461	1.429	101.2	121.3
3-21G	1.961	1.364	1.400	109.0	121.1	1.925	1.394	1.410	106.6	121.1
6-31G(d)	2.007	1.340	1.391	110.9	121.1	1.954	1.375	1.409	108.2	121.2
6-31G(d,p)	2.007	1.340	1.390	110.9	121.1	1.954	1.375	1.408	108.2	121.2
6-31+G(d,p)	2.023	1.339	1.391	111.4	121.1	1.967	1.374	1.410	108.7	121.2
6-311+G(d,p)	2.023	1.338	1.390	111.5	121.1	1.968	1.372	1.406	108.9	121.2
6-311+G(2d,p)	1.969	1.348	1.402	109.8	121.2	1.966	1.370	1.404	108.9	121.2
LanL2MB	2.033	1.410	1.385	108.3	121.0	1.987	1.422	1.421	107.8	121.2
LanL2DZ	1.987	1.370	1.411	109.4	121.1	1.985	1.393	1.420	108.4	121.1

Table 2.1 *(Continued.)*

PM6					Exp.[15)]				
Bond length			Bond angle		Bond length			Bond angle	
Cu-N_1	C_1-N_1	C_β- C_β'	C_1-N_1-C_1	C_α-C_β-C_β'	Cu-N_1	C_1-N_1	C_β- C_β'	C_1-N_1-C_1	C_α-C_β-C_β'
1.988	1.404	1.392	108.2	121.2	1.935	1.366	1.413	107.3	121.0

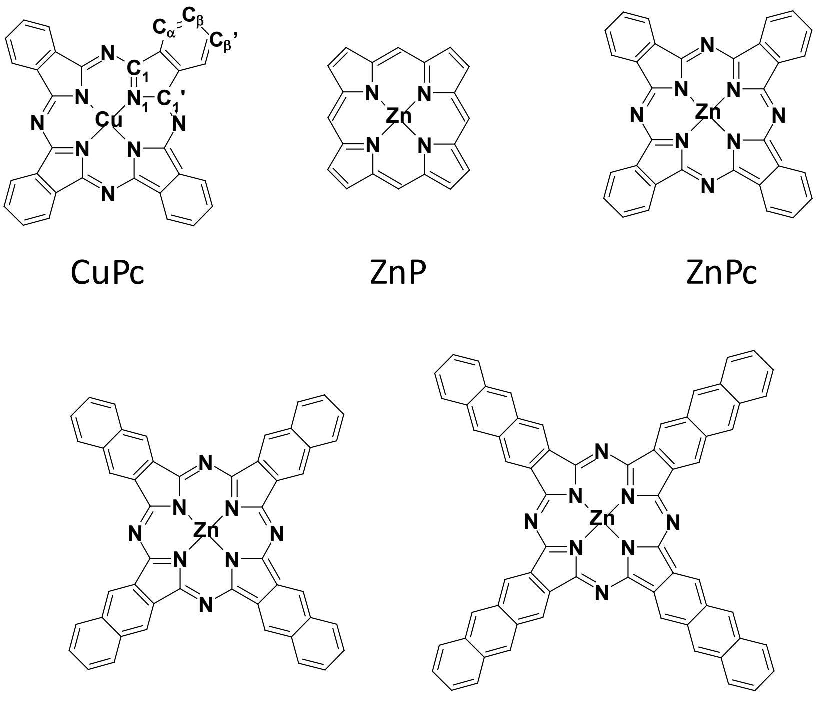

CuPc ZnP ZnPc

ZnNPc ZnAPc

Fig. 2.5. The molecular structures of CuPc, ZnP, ZnPc, ZnNPc, and ZnAPc.

Table 2.2 Calculation time represented as a ratio compared with HF/sto-3G.

Basis set	Basis functions	Calculation time		
		PM6	HF	B3LYP
	185	0.3		
sto-3G	234		1.0	3.5
3-21G	421		1.6	2.2
6-31G(d)	668		18.8	6.2
6-31G(d,p)	716		9.7	7.2
6-31+G(d,p)	889		54.7	51.1
6-311+G(d,p)	1034		68.9	43.0
6-311+G(2d,p)	1241		71.1	64.3
LanL2MB	229		1.6	1.2
LanL2DZ	414		3.6	3.6

Table 2.1 shows the calculated some bond lengths and some bond angles of CuPc. The calculation time ratio compared with HF/sto-3G in each calculation are also presented in Table 2.2 and Fig. 2.6. At PM6 level, the obtained bond length and bond angles are modestly correspondent to the experimental data with much small calculation cost. Therefore, this result suggests that semi-empirical method is very useful to obtain roughly optimized structure. In contrast, HF and B3LYP with sto-3G basis set give less consistency between calculation and experimental results than PM6 despite larger calculation cost. On the other hand, for both HF and B3LYP with from 3-21G to 6-311+G(2d,p) basis set and LanL2MB and LanL2DZ basis set, while accuracy of the calculated structural properties increased with increasing basis set level, the calculation cost also increased exponentially with increasing basis set level. On the other hand, comparison of HF with B3LYP suggests that B3LYP calculation give more correspondence structural properties with experiment in lower basis set than HF. As indicated in the Fig 2.6, the difference of calculation time between HF and B3LYP is not large and the calculation time drastically increases with increasing the number of basis functions. We also calculated about a CuPc molecule using Møller-Plesset perturbation method in second order

(MP2).[18)] However, even basis set is sto-3G, the calculation time ratio compared with HF/sto-3G is larger than 80. This result indicates that the calculation based on perturbation theory is much high-cost. To perform quantum chemical calculation about CuPc series, these results are helpful to select the appropriate calculation method.

Figure 2.7 shows molecular size dependency of calculation time per one SCF cycle in zinc phthalocyanine derivatives. The calculation time are represented as a ratio compared with ZnP. As a result, the calculation times approximately double per 4 benzene rings, or per about 160 basis functions. This result is useful to predict the calculation cost in larger phthalocyanine series system.

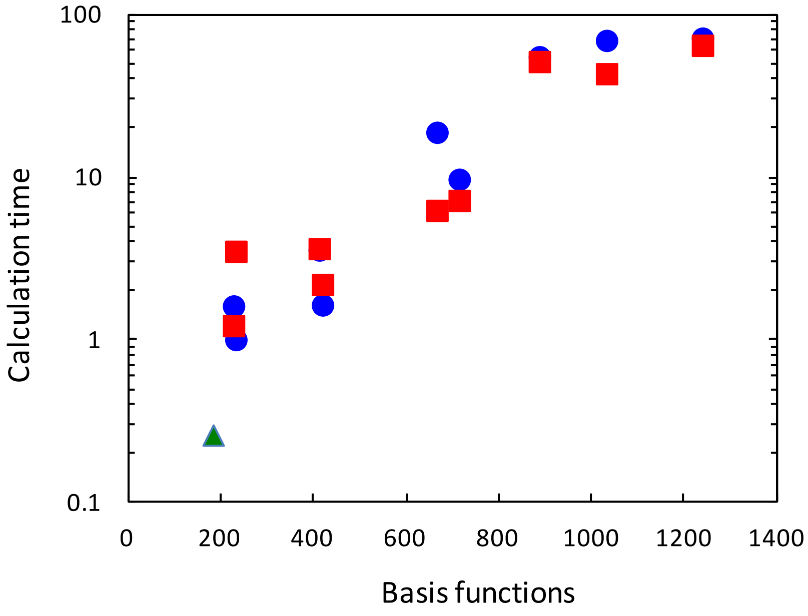

Fig. 2.6. Correlation between basis function and calculation time in CuPc calculation. Calculation times are evaluated by a ratio compared with HF/sto-3G. Red square, blue circle, and green triangle correspond to the calculation time by HF, B3LYP, and PM6 method, respectively.

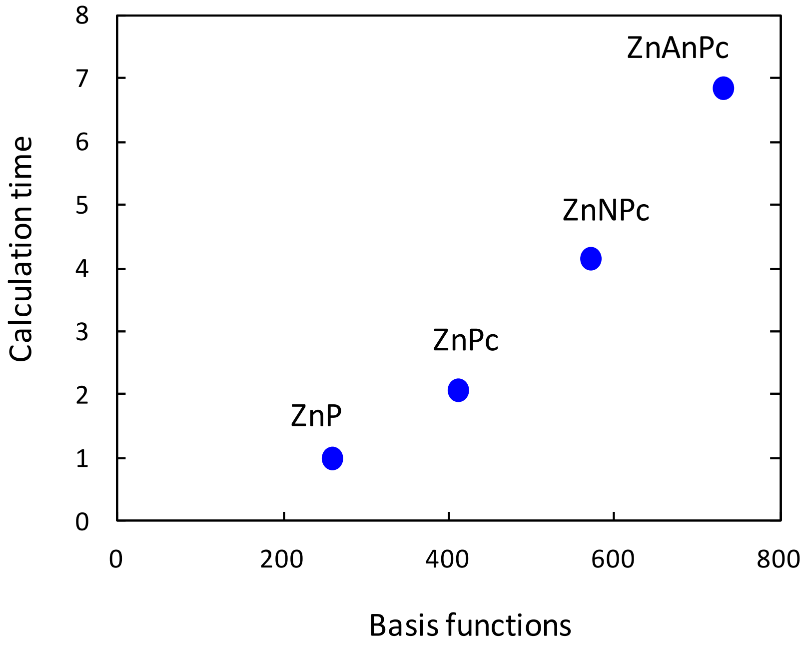

Fig. 2.7. Molecular size dependency of calculation time per one SCF cycle in zinc phthalocyanine derivatives. The SCF calculation was performed about each optimized structure and used B3LYP method with LanL2DZ. The calculation times are represented as a ratio compared with ZnP.

2.4 References

1) W. Heitler and F. London: Z. Phys. **44** (1927) 455.
2) J. C. Slater: Phys. Rev. **37** (1931) 481.
3) L. Pauling: Chem. Revs. **5** (1928) 173.
4) R. S. Mulliken: Phys. Rev. **32** (1928) 186.
5) R. S. Mulliken: Phys. Rev. **32** (1928) 761.
6) R. S. Mulliken: Phys. Rev. **33** (1929) 730.
7) E. Hückel: Z. Phys. **60** (1930) 423.
8) P. Hohenberg and W. Kohn: Phys. Rev. **136** (1964) B864.
9) K. Fukui, T. Yonezawa, and H. Shingu: J. Chem. Phys. **20** (1952) 722.
10) R. B. Woodward and R. Hoffmann: J. Am. Chem. Soc. **87** (1965) 395.
11) E. Runge and E. K. U. Gross: Phys. Rev. Lett. **52** (1984) 997.
12) W. Kohn and L. J. Sham: Phys. Rev. **140** (1965) A1133.
13) J. J. P. Stewart: J. Mol. Model. **13** (2007) 1173.
14) A. D. Becke: J. Chem. Phys. **98** (1993) 5648.
15) C. Lee, W. Yang, and R. G. Parr: Phys. Rev. B **37** (1988) 785.
16) M. J. Frisch *et al.*: Gaussian 09, Revision B.01 (Gaussian, Inc., Wallingford CT, 2010).
17) C. J. Brown: J. Chem. Soc. A (1968) 2488.
18) M. H-. Gordon, J. A. Pople, and M. J. Frisch: Chem. Phys. Lett. **153** (1988) 503.

Chapter 3

Partially Fluorinated Copper Phthalocyanine toward Band Engineering for High-Efficiency Organic Photovoltaics

3.1 Introduction

Organic photovoltaics (OPVs) have been drawing intense research interest because of their unique features such as being flexible, lightweight, and large-area devices.1-5) The energy band engineering for organic semiconductors plays an important role in realizing highly efficient OPVs.6) The systematic coordination of HOMO and LUMO energy levels leads to the improvement of the conversion efficiency of OPVs. Therefore, the adjustment of HOMO and LUMO levels in organic semiconductors by changing the molecular substituents and/or the molecular structures has been widely studied.7-10)

Phthalocyanine series are promising materials for OPVs because of their high chemical and thermal stability.11-15) Copper phthalocyanine (CuPc) is a typical phthalocyanine, and acts as a p-type semiconductor. The energy level of phthalocyanines generally depends on the metal at the center,16) the degree of polymerization,17,18) and the substituents at the benzene ring.19-22) In particular, halogenation at the benzene ring leads to a decrease in the energy level.19,22-25) Halogenated phthalocyanines, such as F_{16}CuPc and Cl_{16}CuPc, act as n-type semiconductors. 13,26-28) In halogenation, fluorination strongly affects the energy level because of the strong electron-withdrawing ability of fluorine atoms. Murdey *et al.* have measured the HOMO and LUMO energy levels of CuPc, an isomer of F_8CuPc, and F_{16}CuPc from the results of ultraviolet photoemission and inverse photoemission spectroscopy.29) Peisert *et al.* have reported the electronic structures of CuPc, an isomer of F_4CuPc, and F_{16}CuPc.25,30,31) However, there have been no reports on a systematic analysis on the number and position of substituting fluorine atoms.

In this chapter, we report the electronic structures, vibrational structures, and energy levels of F_xCuPc (x = 0, 4, 8, 12, and 16) determined by quantum chemical calculation. In particular, we focus on the effects of the number and position of fluorine atoms on the HOMO and LUMO energy levels. To evaluate the validity of the calculation, we show the UV-visible absorption and photoelectron yield spectra of CuPc, F_8CuPc, and $F_{16}CuPc$ thin films prepared by thermal evaporation. The chemical structures of CuPc, F_8CuPc, and $F_{16}CuPc$ are shown in Fig. 3.1. The relationship between the calculated and experimental results is discussed.

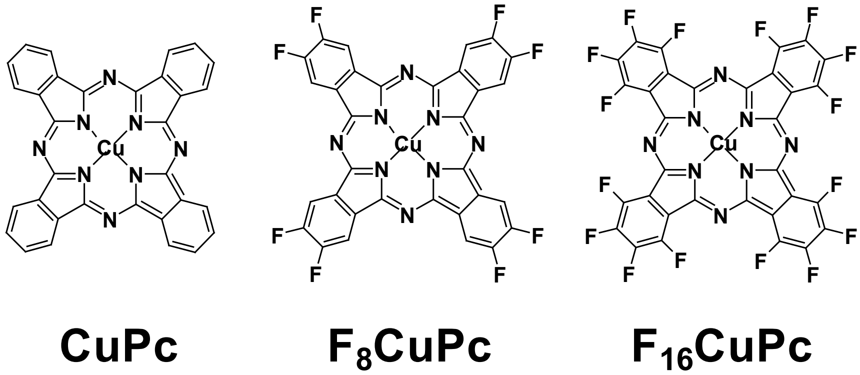

Fig. 3.1. Molecular structures of CuPc, F_8CuPc, and $F_{16}CuPc$.

3.2 Experimental

3.2.1 Computational details

Figure 3.2 shows the molecular structure of F_xCuPc used for the calculation including the numbering of the atoms used to represent the positions of the bonds, the bond angles, and the substituting fluorine atoms. We calculated the electronic and vibrational structures of the following molecules: CuPc, two isomers of F_4CuPc, three isomers of F_8CuPc, two isomers of $F_{12}CuPc$, and $F_{16}CuPc$. The molecules have four-fold rotational symmetry. The structure of F_xCuPc (x = 4, 8, and 12) is identified by the position of the fluorine atoms. The position is represented in the parentheses appended to the name of the molecule. The characters α_1, α_2, β_1, and β_2 in the parentheses denote fluorine atoms at $R_{\alpha1}$, $R_{\alpha2}$, $R_{\beta1}$, and $R_{\beta2}$, respectively. The substitutions at $R_{\alpha1}$ and $R_{\alpha2}$ ($R_{\beta1}$ and $R_{\beta2}$) are collectively referred to as α-substitution (β-substitution).

The geometry of F_xCuPc was optimized to calculate the electronic structure. The vibrational analysis in the optimized structure was performed. The vibration in the results shown in this paper showed no imaginary frequency, which indicates the stability of the optimized structure. The geometry optimization and vibrational analysis were performed by a hybrid density functional theory method combining the Becke three-parameter exchange functional and Lee-Yang-Parr correlation functional (B3LYP) using the LanL2DZ basis set.[32,33] The calculated frequencies were scaled by the factor 0.9614[34]. The Gaussian 09 program package was used for the calculation.[35]

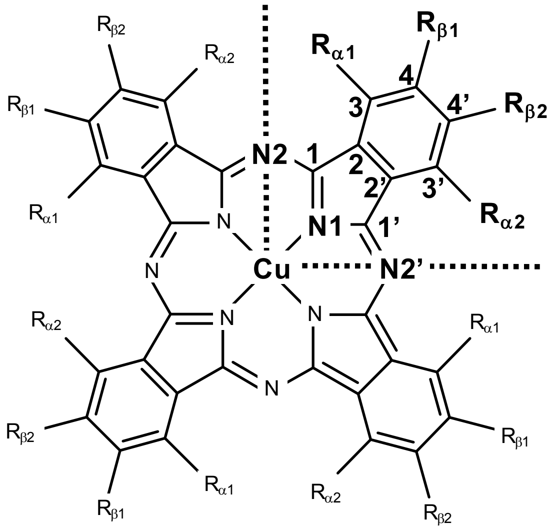

Fig. 3.2. Molecular structure of F_xCuPc used for calculation. $R_{\alpha 1}$, $R_{\alpha 2}$, $R_{\beta 1}$, and $R_{\beta 2}$ represent hydrogen or fluorine atoms. The structure has four-fold rotational symmetry.

3.2.2 Thin-film preparation and characterization

Thin films of CuPc, F_8CuPc (β_1, β_2), and $F_{16}CuPc$ were prepared by thermal evaporation as follows. The compounds were purchased from Tokyo Chemical Industry Co., Ltd. The F_8CuPc and $F_{16}CuPc$ (sublimation grade) were used as received without further purification. CuPc purified by train sublimation was used. Glass substrates were treated by O_2 plasma. Then, an organic thin film of CuPc, F_8CuPc, or $F_{16}CuPc$ was deposited on the substrate by thermal evaporation. The deposition rate ranged from 0.02 to 0.06 nm/s. The thicknesses of the films were 120 nm for CuPc and $F_{16}CuPc$ and 70 nm for F_8CuPc.

Absorption spectra of the film on the glass substrate were measured between 1.4 and 4.1 eV with a Hitachi U-3900 spectrophotometer. Photoelectron yield spectroscopy of the surface of the film deposited on the substrate was carried out at excitation photon energies in the range of 4.5 to 7.0 eV using a Riken Keiki AC-3 photoelectron spectrometer.[36]

3.3. Results

3.3.1 Optimized molecular structures

All calculated structures of F_xCuPc (x = 0, 4, 8, 12, and 16) are planar structures having D_{4h} or C_{4h} symmetry. The symmetry of CuPc, F_8CuPc (α_1, α_2), F_8CuPc (β_1, β_2), and F_{16}CuPc is D_{4h}; that of F_4CuPc, F_8CuPc (α_1, β_2), and F_{12}CuPc is C_{4h}. The symmetry of D_{4h} for the optimized structure of CuPc is the same as those shown in previous reports.[37,38)]

Table 3.1. Calculated bond lengths of F_xCuPc expressed in Å.

	CuPc	F_4CuPc		F_8CuPc			F_{12}CuPc		F_{16}CuPc
		(α_1)	(β_1)	(α_1,α_2)	(α_1,β_2)	(β_1, β_2)	(α_1, α_2, β_1)	(α_1, β_1, β_2)	
Cu−N1	1.985	1.986	1.984	1.990	1.986	1.984	1.989	1.986	1.989
N1−C1 (N1−C1')	1.393	1.395 (1.390)	1.393 (1.393)	1.392	1.395 (1.389)	1.393	1.391 (1.392)	1.394 (1.389)	1.391
C1−N2 (C1'−N2')	1.337	1.335 (1.336)	1.336 (1.337)	1.334	1.335 (1.335)	1.336	1.333 (1.334)	1.334 (1.335)	1.333
C1−C2 (C1'−C2')	1.465	1.464 (1.464)	1.465 (1.463)	1.464	1.463 (1.465)	1.464	1.465 (1.463)	1.464 (1.464)	1.464
C2−C2'	1.418	1.421	1.418	1.423	1.421	1.418	1.423	1.420	1.422
C2−C3 (C2'−C3')	1.404	1.400 (1.402)	1.403 (1.405)	1.400	1.401 (1.402)	1.404	1.399 (1.401)	1.399 (1.402)	1.399
C3−C4 (C3'−C4')	1.407	1.399 (1.407)	1.397 (1.405)	1.400	1.397 (1.397)	1.395	1.403 (1.398)	1.401 (1.395)	1.401
C4−C4'	1.420	1.416	1.411	1.411	1.408	1.415	1.403	1.412	1.408
C3−$R_{\alpha1}$ (C3'−$R_{\alpha2}$)	1.086	1.394 (1.085)	1.084 (1.085)	1.388	1.389 (1.084)	1.084	1.379 (1.384)	1.380 (1.084)	1.376
C4−$R_{\beta1}$ (C4'−$R_{\beta2}$)	1.087	1.086 (1.086)	1.401 (1.085)	1.085	1.084 (1.396)	1.390	1.387 (1.084)	1.381 (1.386)	1.379

The bond length and bond angle of the optimized structure are shown in Tables 3.1 and 3.2, respectively. The structure of CuPc is almost the same as those experimentally and computationally obtained in earlier works.[38,39)] A slight difference is that the bond length in this work is slightly larger than those in the earlier works. The calculation results for partially fluorinated CuPc show that a fluorine atom deforms the benzene ring having the fluorine atom. The angle at a carbon atom bonding to a fluorine atom is larger than that at the carbon atom of CuPc. The angles of C2–C3–C4 are 117.6° for CuPc and 120.6° for F_8CuPc (α_1, α_2); the angles of C3–C4–C4’ are 121.1° for CuPc and 121.9° for F_8CuPc (β_1, β_2).

Table 3.2. Calculated bond angles of F_xCuPc expressed in degree.

	CuPc	F_4CuPc		F_8CuPc			F_{12}CuPc		F_{16}CuPc
		(α_1)	(β_1)	(α_1,α_2)	(α_1,β_2)	(β_1, β_2)	(α_1, α_2, β_1)	(α_1, β_1, β_2)	
C1–N1–C1'	108.4	108.6	108.5	108.9	108.7	108.5	108.9	108.7	108.9
N2–C1–N1 (N2'–C1'–N1)	127.2	126.7 (127.8)	127.4 (127.2)	127.3	126.7 (127.9)	127.3	127.4 (127.3)	126.9 (127.9)	127.4
N1–C1–C2 (N1–C1'–C2')	109.1	108.8 (109.2)	109.0 (109.1)	108.9	108.8 (109.1)	109.0	108.9 (108.9)	108.8 (109.1)	108.8
C1–C2–C2' (C1'–C2'–C2)	106.7	106.9 (106.5)	106.7 (106.7)	106.7	106.9 (106.5)	106.7	106.6 (106.7)	106.9 (106.5)	106.7
C2'–C2–C3 (C2–C2'–C3')	121.3	118.3 (122.5)	121.6 (121.3)	119.6	118.5 (122.9)	121.6	120.6 (119.6)	119.3 (122.8)	120.5
C2–C3–C4 (C2'–C3'–C4')	117.6	120.7 (117.6)	115.6 (118.0)	120.6	120.8 (115.6)	116.5	118.1 (120.6)	118.9 (116.3)	118.7
C3–C4–C4' (C3'–C4'–C4)	121.1	119.8 (121.1)	124.3 (119.2)	119.9	118.1 (124.1)	121.9	122.4 (118.7)	120.4 (122.2)	120.8

3.3.2 Charge distributions

The atomic charge distribution of F_xCuPc (x = 0, 4, 8, 12, and 16) are shown in Table 3.3. The fluorine atoms have negative charges due to the large electronegativity of fluorine atom. Also, a carbon atom bonding to a fluorine atom has more positive charges than a carbon atom bonding to a hydrogen atom. The charges of a carbon atom bound to a hydrogen atom in CuPc are –0.402 e (–0.209 e) at carbon C3 (C4), and the charges of a carbon atom bonding to a fluorine atom in F_{16}CuP are 0.025 e (0.104 e) at carbon C3 (C4). The fluorination effects on charge distributions extend to copper atom and nitrogen N1, which are at central part in

F_xCuPc molecule. The positive charges of copper atom and nitrogen N1 increase with an increase in the number of fluorine atoms. The average charges in Cu/N1 in F_xCuPc (x = 0, 4, 8, 12, and 16) are 0.865/–0.404 (CuPc), 0.876/–0.404 (F_4CuPc), 0.885/–0.402 (F_8CuPc), 0.896/-0.401 (F_{12}CuPc), and 0.905/–0.398 (F_{16}CuPc), respectively.

Table 3.3. Calculated atomic charges of F_xCuPc expressed in *e*.

	CuPc	F_4CuPc		F_8CuPc			F_{12}CuPc		F_{16}CuPc
		(α_1)	(β_1)	(α_1,α_2)	(α_1,β_2)	(β_1, β_2)	(α_1, α_2, β_1)	(α_1, β_1, β_2)	
Cu	0.865	0.877	0.874	0.887	0.886	0.883	0.896	0.895	0.905
N1	–0.404	–0.403	–0.404	0.401	–0.402	–0.403	–0.400	–0.401	–0.398
N2	0.096	0.124	0.097	0.154	0.125	0.099	0.152	0.125	0.151
C1 (C1')	–0.079	–0.051 (–0.081)	–0.072 (–0.072)	–0.058	–0.044 (–0.074)	–0.068	–0.055 (–0.050)	–0.042 (–0.072)	–0.052
C2 (C2')	0.252	0.101 (0.299)	0.284 (0.271)	0.155	0.110 (0.338)	0.318	0.208 (0.176)	0.160 (0.386)	0.264
C3 (C3')	–0.402	0.186 (–0.424)	–0.550 (–0.371)	0.165	0.232 (–0.587)	–0.525	–0.006 (0.213)	0.085 (–0.573)	0.025
C4 (C4')	–0.209	–0.352 (–0.163)	0.369 (–0.350)	–0.310	–0.508 (0.432)	0.226	0.281 (–0.476)	0.049 (0.302)	0.104
$R_{\alpha1}$ ($R_{\alpha2}$)	0.260	–0.216 (0.278)	0.287 (0.268)	–0.198	–0.206 (0.303)	0.293	–0.170 (–0.189)	–0.181 (0.309)	–0.163
$R_{\beta1}$ ($R_{\beta2}$)	0.224	0.251 (0.233)	–0.233 (0.258)	0.259	0.283 (–0.223)	–0.202	–0.197 (0.289)	–0.176 (–0.194)	–0.169

3.3.3 Vibrational structures

F_xCuPc molecule is composed of 8 nitrogen atoms, 32 carbon atoms, 16 – x hydrogen atoms, x fluorine atoms, and one copper atom. Therefore every F_xCuPc molecule consists of 57 atoms and has 3 × 57 – 6 = 165 normal vibrational modes. All F_xCuPc molecules with D_{4h} symmetry have the same vibrational modes as below:

$$\Gamma_{vib(D4h)} = 14A_{1g} + 13A_{2g} + 14B_{1g} + 14B_{2g} + 13E_g \\ + 6A_{1u} + 8A_{2\mathrm{u}} + 7B_{1\mathrm{u}} + 7B_{2\mathrm{u}} + 28E_{\mathrm{u}} ,$$

and all F_xCuPc molecules with C_{4h} symmetry have the same vibrational modes as below:

$$\Gamma_{vib(C4h)} = 27A_g + 28B_g + 13E_g + 14A_u + 14B_\mathrm{u} + 28E_\mathrm{u} .$$

These vibrations can be divides into in-plane vibration modes (A_{1g}, A_{2g}, B_{1g}, B_{2g}, and E_u in D_{4h} symmetry and A_g, B_g, and E_u in C_{4h} symmetry) and out-of-plane vibration modes (A_{1u}, A_{2u}, B_{1u}, B_{2u}, and E_g in D_{4h} symmetry and Au, B_u, and E_g in C_{4h} symmetry). A_{2u} and E_u (A_u and E_u) modes in D_{4h} (C_{4h}) symmetry are infrared active.

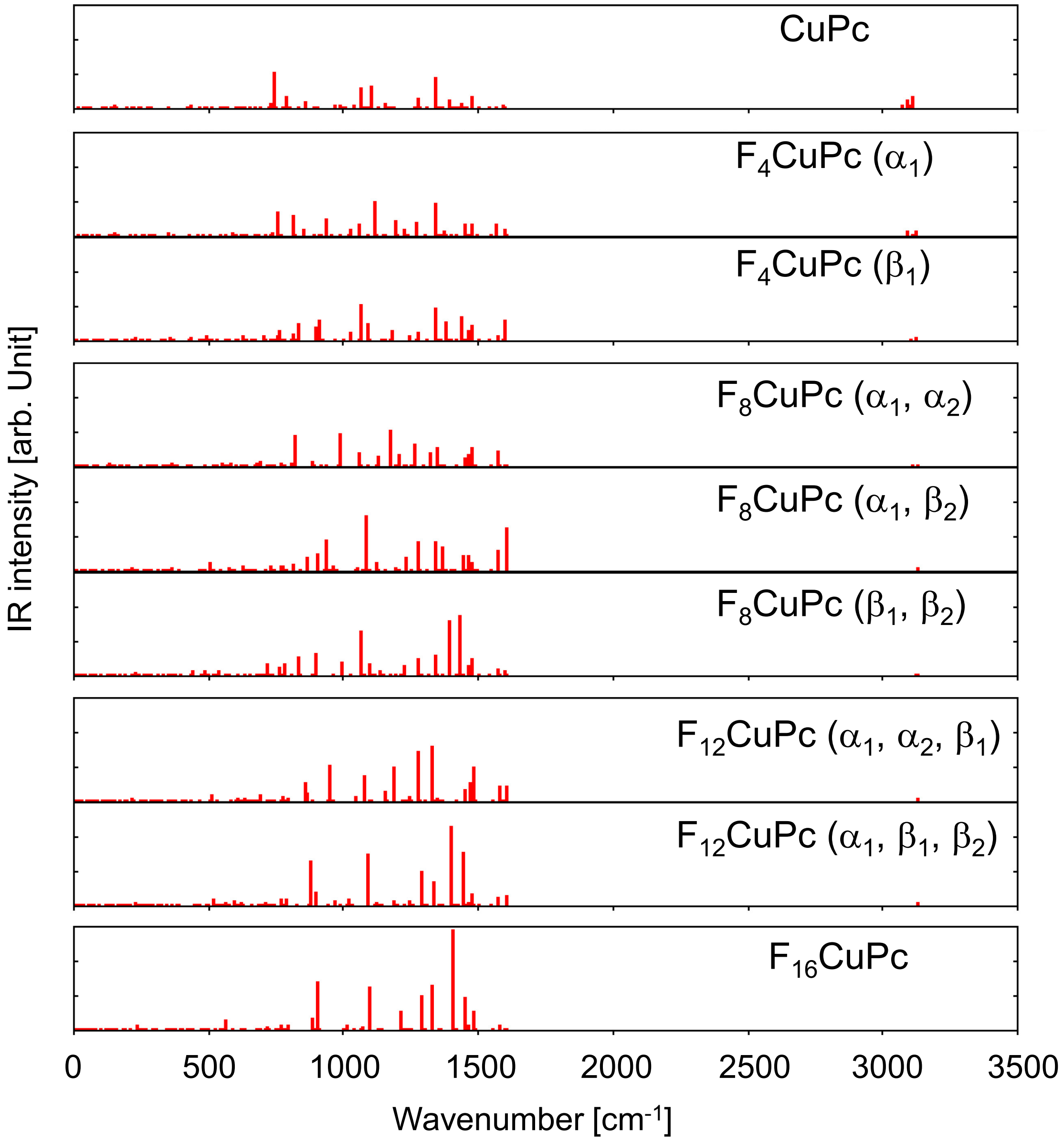

Fig. 3.3. Calculated IR spectra of F_xCuPc.

Table 3.4. Calculated infrared active vibrational modes of F_xCuPc (x = 0, 8, and 16).

CuPc			F_8CuPc									$F_{16}CuPc$		
			(α_1,α_2)			(α_1,β_2)			(β_1, β_2)					
Sym.	Fre.	Int.	Sym.	Fre.	Int.	Sym.	Fre.	Int.	Sym.	Fre.	Int.	Sym.	Fre.	Int.
1 A_{2u}	39	2.0	1 A_{2u}	37	1.4	1 A_u	30	0.0	1 A_{2u}	26	0.9	1 A_{2u}	27	0.9
1 E_u	115	3.7	1 E_u	86	3.6	2 A_u	62	0.2	1 E_u	73	0.0	1 E_u	66	0.3
2 A_{2u}	153	11.0	2 A_{2u}	133	15.6	1 E_u	79	1.2	2 A_{2u}	128	0.2	2 A_{2u}	104	0.4
2 E_u	279	5.2	3 A_{2u}	155	4.2	3 A_u	136	0.2	3 A_{2u}	232	21.2	3 A_{2u}	151	0.5
3 A_{2u}	285	0.6	2 E_u	204	0.0	2 E_u	217	0.9	2 E_u	237	0.5	2 E_u	194	0.1
3 E_u	291	0.7	3 E_u	251	4.7	4 A_u	218	16.1	3 E_u	265	0.7	4 A_{2u}	241	24.6
4 A_{2u}	356	1.0	4 A_{2u}	294	0.2	5 A_u	238	3.9	4 E_u	276	0.0	3 E_u	249	4.6
5 A_{2u}	439	20.6	4 E_u	335	2.6	3 E_u	261	3.1	4 A_{2u}	354	1.7	4 E_u	261	1.1
4 E_u	492	5.4	5 A_{2u}	353	0.3	4 E_u	317	6.5	5 E_u	369	7.1	5 E_u	269	0.4
5 E_u	562	6.8	5 E_u	369	18.3	6 A_u	333	2.3	5 A_{2u}	397	0.0	6 E_u	308	3.2
6 E_u	628	3.4	6 E_u	434	0.3	7 A_u	360	0.0	6 A_{2u}	441	27.8	5 A_{2u}	347	1.6
7 E_u	733	25.6	7 E_u	550	9.4	5 E_u	366	7.7	6 E_u	489	30.8	7 E_u	366	2.5
6 A_{2u}	745	306.0	6 A_{2u}	585	18.7	8 A_u	476	0.1	7 E_u	540	26.6	6 A_{2u}	377	0.0
8 E_u	779	3.8	8 E_u	586	7.3	6 E_u	488	5.6	8 E_u	581	0.6	8 E_u	440	0.0
7 A_{2u}	793	86.5	9 E_u	682	17.8	7 E_u	508	65.2	9 E_u	703	3.4	9 E_u	474	5.5
9 E_u	864	39.7	10 E_u	695	33.3	8 E_u	582	9.2	10 E_u	721	83.0	10 E_u	569	79.2
8 A_{2u}	973	8.6	7 A_{2u}	771	8.6	9 A_u	590	6.0	7 A_{2u}	768	59.0	11 E_u	631	1.8
10 E_u	989	18.4	11 E_u	809	7.8	10 A_u	628	29.1	11 E_u	786	87.0	7 A_{2u}	637	0.9
11 E_u	1043	10.5	8 A_{2u}	824	260.8	9 E_u	638	2.4	12 E_u	838	155.2	12 E_u	720	13.1
12 E_u	1065	160.0	12 E_u	885	33.8	10 E_u	736	26.4	8 A_{2u}	903	182.7	8 A_{2u}	773	31.2
13 E_u	1107	179.2	13 E_u	989	269.3	11 A_u	769	25.2	13 E_u	997	102.9	13 E_u	801	34.5
14 E_u	1159	29.7	14 E_u	1060	108.0	12 A_u	775	30.8	14 E_u	1069	376.0	14 E_u	887	88.6
15 E_u	1173	2.5	15 E_u	1131	73.2	11 E_u	817	39.1	15 E_u	1102	86.3	15 E_u	907	400.3
16 E_u	1275	4.4	16 E_u	1179	305.7	13 A_u	865	109.1	16 E_u	1140	25.4	16 E_u	1015	28.7
17 E_u	1280	76.4	17 E_u	1208	46.3	14 A_u	905	136.9	17 E_u	1196	1.5	17 E_u	1075	14.1
18 E_u	1344	255.1	18 E_u	1211	92.6	12 E_u	939	251.6	18 E_u	1230	75.8	18 E_u	1102	367.5
19 E_u	1396	66.9	19 E_u	1270	178.6	13 E_u	962	30.7	19 E_u	1283	139.3	19 E_u	1213	156.5
20 E_u	1444	33.7	20 E_u	1323	110.4	14 E_u	1056	11.8	20 E_u	1341	160.4	20 E_u	1251	0.1
21 E_u	1463	0.3	21 E_u	1352	145.5	15 E_u	1084	458.5	21 E_u	1398	468.8	21 E_u	1291	286.9
22 E_u	1481	90.1	22 E_u	1456	63.6	16 E_u	1123	64.2	22 E_u	1434	503.5	22 E_u	1331	377.6
23 E_u	1571	1.6	23 E_u	1468	95.7	17 E_u	1196	21.4	23 E_u	1470	72.6	23 E_u	1407	850.5
24 E_u	1597	10.3	24 E_u	1480	153.8	18 E_u	1238	111.9	24 E_u	1483	128.3	24 E_u	1454	276.3
25 E_u	3075	9.2	25 E_u	1579	112.9	19 E_u	1282	236.8	25 E_u	1577	46.0	25 E_u	1469	36.0
26 E_u	3092	52.6	26 E_u	1605	0.6	20 E_u	1348	238.0	26 E_u	1605	35.8	26 E_u	1483	144.8
27 E_u	3109	13.7	27 E_u	3113	3.2	21 E_u	1371	194.8	27 E_u	3128	5.4	27 E_u	1583	27.8
28 E_u	3115	83.3	28 E_u	3130	3.0	22 E_u	1448	118.4	28 E_u	3130	3.6	28 E_u	1605	4.2
						23 E_u	1469	112.8						
						24 E_u	1481	54.0						
						25 E_u	1577	167.0						
						26 E_u	1608	367.0						
						27 E_u	3134	9.9						
						28 E_u	3135	2.4						

Sym., symmetry modes; Fre., frequency (cm^{-1}); Int., Intensity.

Table 3.5. Calculated infrared active vibrational modes of F_xCuPc (x = 4 and 12).

F_4CuPc						$F_{12}CuPc$					
(α_1)			(β_1)			(α_1, α_2, β_1)			(α_1, β_1, β_2)		
Sym.	Fre.	Int.	Sym.	Fre.	Int.	Sym.	Fre.	Int.	Sym.	Fre.	Int.
1 A_u	37	1.2	1 A_u	30	0.0	1 A_u	30	0.0	1 A_u	26	0.9
2 A_u	72	5.2	1 E_u	87	0.7	2 A_u	49	0.5	2 A_u	59	1.4
1 E_u	97	4.7	2 A_u	98	2.8	1 E_u	74	1.3	1 E_u	69	0.6
3 A_u	151	11.2	3 A_u	143	3.2	3 A_u	108	1.8	3 A_u	119	0.1
2 E_u	230	2.3	4 A_u	229	13.4	4 A_u	151	0.1	4 A_u	149	0.1
4 A_u	233	0.5	2 E_u	252	0.9	2 E_u	199	0.1	2 E_u	213	1.5
3 E_u	284	2.1	3 E_u	280	0.3	5 A_u	218	21.9	5 A_u	230	21.1
5 A_u	299	0.0	5 A_u	329	0.7	3 E_u	250	5.1	3 E_u	259	1.7
6 A_u	355	0.2	6 A_u	359	0.7	4 E_u	270	1.1	4 E_u	263	0.5
4 E_u	356	10.2	4 E_u	360	17.2	6 A_u	311	0.1	6 A_u	283	0.3
7 A_u	428	0.0	7 A_u	441	21.9	5 E_u	325	5.3	5 E_u	293	2.3
5 E_u	482	5.2	8 A_u	483	6.8	7 A_u	353	0.5	7 A_u	350	1.5
6 E_u	544	5.6	5 E_u	496	33.3	6 E_u	366	6.6	6 E_u	367	3.3
8 A_u	546	0.1	6 E_u	511	6.6	8 A_u	379	0.1	8 A_u	386	0.2
7 E_u	592	16.3	7 E_u	610	2.4	7 E_u	436	0.1	7 E_u	464	2.5
9 A_u	622	5.9	9 A_u	634	25.1	9 A_u	472	1.7	9 A_u	493	1.2
8 E_u	689	6.7	8 E_u	706	28.4	8 E_u	512	50.0	8 E_u	519	39.6
9 E_u	742	18.4	9 E_u	758	35.4	10 A_u	606	6.3	10 A_u	569	12.4
10 A_u	758	193.3	10 A_u	767	72.5	9 E_u	611	7.6	9 E_u	596	35.8
11 A_u	772	4.5	11 A_u	775	0.0	10 E_u	639	12.8	10 E_u	627	19.2
12 A_u	818	158.7	10 E_u	814	40.7	11 A_u	664	3.7	11 A_u	691	0.2
10 E_u	853	40.3	12 A_u	839	141.6	11 E_u	692	47.2	11 E_u	717	12.0
13 A_u	915	0.0	13 A_u	899	104.9	12 A_u	770	7.1	12 A_u	769	47.8
11 E_u	936	127.6	11 E_u	916	160.9	13 A_u	778	24.7	13 A_u	776	1.3
14 A_u	991	6.4	14 A_u	973	0.4	12 E_u	797	11.1	12 E_u	791	39.5
12 E_u	1027	39.5	12 E_u	1032	57.9	14 A_u	862	151.7	13 E_u	879	375.9
13 E_u	1059	84.0	13 E_u	1069	307.0	13 E_u	866	57.4	14 A_u	901	100.1
14 E_u	1119	281.8	14 E_u	1096	132.0	14 E_u	953	297.2	14 E_u	969	35.2
15 E_u	1154	2.5	15 E_u	1144	4.3	15 E_u	1049	35.1	15 E_u	1020	39.9
16 E_u	1197	115.2	16 E_u	1185	77.1	16 E_u	1079	216.5	16 E_u	1095	430.0
17 E_u	1231	38.0	17 E_u	1246	25.2	17 E_u	1160	75.0	17 E_u	1128	15.2
18 E_u	1276	98.4	18 E_u	1277	63.0	18 E_u	1192	277.6	18 E_u	1191	34.8
19 E_u	1345	273.6	19 E_u	1344	277.1	19 E_u	1250	32.7	19 E_u	1248	36.5
20 E_u	1379	25.7	20 E_u	1383	151.3	20 E_u	1283	413.5	20 E_u	1291	281.8
21 E_u	1451	90.5	21 E_u	1440	191.0	21 E_u	1330	464.3	21 E_u	1339	188.4
22 E_u	1465	7.4	22 E_u	1468	76.7	22 E_u	1351	13.7	22 E_u	1403	674.8
23 E_u	1480	85.6	23 E_u	1482	113.5	23 E_u	1456	83.4	23 E_u	1446	443.6
24 E_u	1570	82.9	24 E_u	1575	34.0	24 E_u	1476	146.8	24 E_u	1470	10.9
25 E_u	1605	46.9	25 E_u	1600	164.5	25 E_u	1484	278.9	25 E_u	1483	92.7
26 E_u	3093	23.2	26 E_u	3108	0.6	26 E_u	1584	116.8	26 E_u	1577	53.4
27 E_u	3114	4.4	27 E_u	3125	8.7	27 E_u	1605	126.4	27 E_u	1608	75.6
28 E_u	3124	30.0	28 E_u	3130	7.1	28 E_u	3136	11.1	28 E_u	3134	8.6

Tables 3.4 and 3.5 show the calculated IR-active vibrational modes and Fig. 3.3 shows simulated IR spectra of F_xCuPc (x = 0, 4, 8, 12, and 16). The simulated IR spectra of CuPc is almost the same as those experimentally and computationally obtained in earlier works.40) All the modes between 3075 and 3136 cm^{-1} in F_xCuPc are typical C–H stretching mode. In C–H stretching modes, the wavenumber increases with an increase in the number of fluorine atoms, and the intensity decreases with an increase in the number of fluorine atoms. Within the IR-active modes, the particularly large IR intensity vibrational modes are in-plane C3–$F_{\beta1}$ stretching mode. These modes are observed at 1398 (F_8CuPc (β_1, β_2)), 1403 ($F_{12}CuPc$ (α_1, β_1, β_2)), and 1407 ($F_{16}CuPc$) cm^{-1}. These IR intensities conform to the order of $F_{16}CuPc$ > $F_{12}CuPc$ (α_1, β_1, β_2) > F_8CuPc (β_1, β_2). The vibrational modes of 1407 cm^{-1} in $F_{16}CuPc$, which are the largest IR intensity modes in F_xCuPc (x = 0, 4, 8, 12, and 16), are shown in Fig. 3.4.

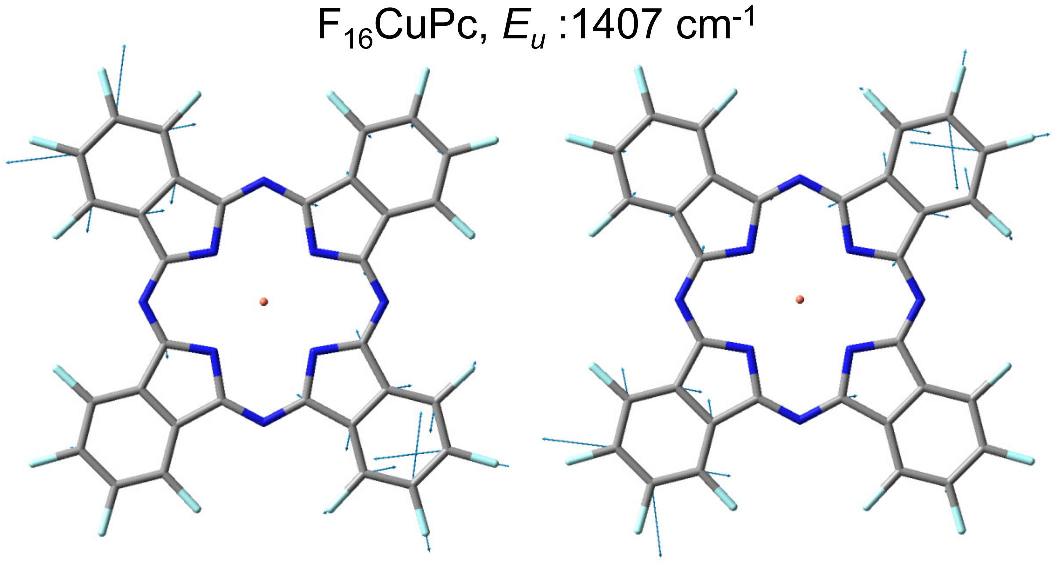

Fig. 3.4. Calculated vibrational modes with the largest IR intensity in F_xCuPc.

3.3.4 Frontier orbitals and their energy levels

Figure 3.5 shows wave functions of the HOMO and LUMO calculated for F_xCuPc (x = 0, 4, 8, 12, and 16). The LUMO is doubly degenerate for all molecules. The symbols a_{1u}, a_u, and

e_g denote representations in group theory. The wave functions of HOMO for all molecules have the same symmetry as represented by a_{1u} or a_u. Also, the wave functions of the LUMO are represented similarly to e_g. It is unclear from Fig. 3.5 that the wave function of the LUMO has the same symmetry for all molecules. This is because the LUMO is doubly degenerate.

The HOMO and LUMO energies calculated for F_xCuPc are summarized in Fig. 3.6 and Table 3.6. The horizontal axis in Fig. 3.6 indicates the position of fluorine atoms. The HOMO and LUMO energies decrease with an increase in the number of fluorine atoms. The HOMO and LUMO energies range from −5.33 to −6.82 eV and from −3.12 to −4.65 eV, respectively. In particular, β-substitution rather than α-substitution leads to large decreases in the HOMO and LUMO energies. The difference in the decrease between α-substitution and β-substitution is probably related to the molecular structure and orbital phase. In addition, the HOMO energy is more sensitive to the number of fluorine atoms than the LUMO energy. The difference in the decrease between the HOMO and LUMO energies affects the HOMO–LUMO gap energy. α-substitution reduces the gap energy, whereas β-substitution increases it. The HOMO–LUMO gap energy ranges from 2.14 to 2.24 eV.

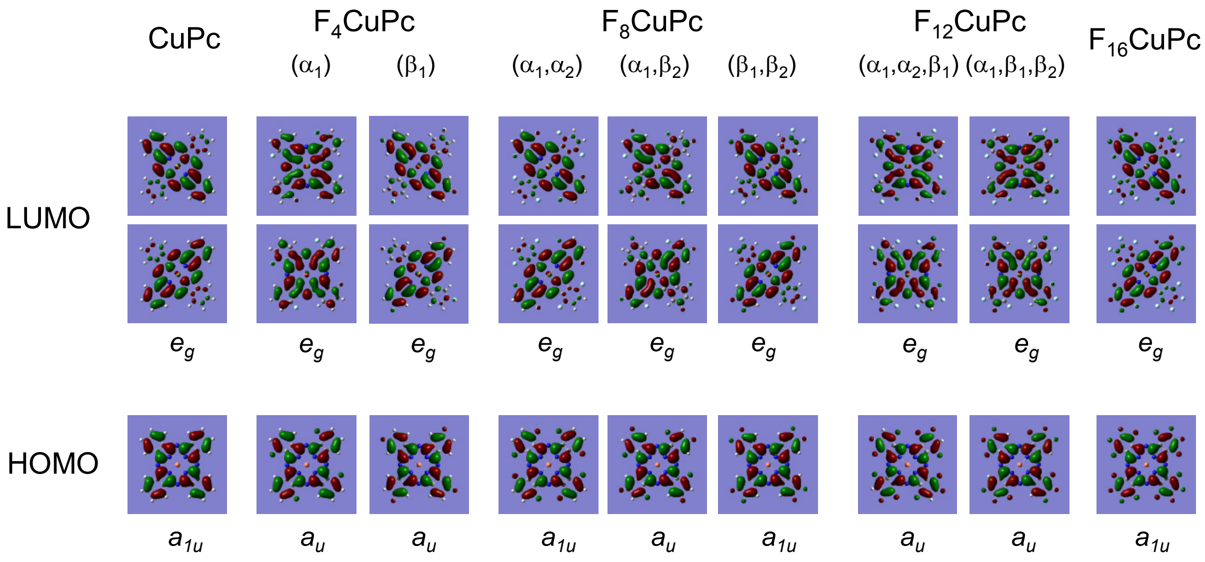

Fig. 3.5. Wave functions of HOMO and LUMO calculated for F_xCuPc.

Table 3.6. Calculated HOMO, LUMO, and HOMO-LUMO gap energies of F_xCuPc.

	HOMO (eV)	LUMO (eV)	HOMO–LUMO gap energy (eV)
CuPc	−5.33	−3.12	2.20
F_4CuPc (α_1)	−5.65	−3.48	2.17
F_4CuPc (β_1)	−5.84	−3.63	2.22
F_8CuPc (α_1, α_2)	−5.93	−3.79	2.14
F_8CuPc (α_1, β_2)	−6.15	−3.96	2.19
F_8CuPc (β_1, β_2)	−6.32	−4.08	2.24
$F_{12}CuPc$ (α_1, α_2, β_1)	−6.38	−4.24	2.15
$F_{12}CuPc$ (α_1, β_1, β_2)	−6.59	−4.38	2.20
$F_{16}CuPc$	−6.82	−4.65	2.17

3.3.5 Spectroscopic analysis

Figure 3.7 shows absorption spectra of CuPc, F_8CuPc (β_1, β_2), and $F_{16}CuPc$ thin films deposited on glass substrates. The spectra of CuPc and $F_{16}CuPc$ in Fig. 3.7 are similar to those in previous reports.[41,42] The spectrum of F_8CuPc has a similar sharp peak to that of CuPc. The spectra of CuPc, F_8CuPc, and $F_{16}CuPc$ have two peaks in the range of 1.4 to 2.4 eV. The absorption spectra in this range are known as the Q-band, which corresponds to $\pi \rightarrow \pi^*$ transitions from a_{1u} to e_g orbitals.[43] The splitting of the absorption spectra into two peaks in the Q-band is caused by the interaction between molecules in a film. The energies at the two peaks are 1.79 and 2.02 eV for CuPc, 1.85 and 2.07 eV for F_8CuPc, and 1.58 and 1.97 eV for $F_{16}CuPc$. The energies for $F_{16}CuPc$ are lower than those for CuPc. On the other hand, the energies for F_8CuPc are higher than those for CuPc. This tendency is consistent with that of the calculated HOMO–LUMO energy gaps of 2.20 eV for CuPc, 2.24 eV for F_8CuPc, and 2.17 eV for $F_{16}CuPc$.

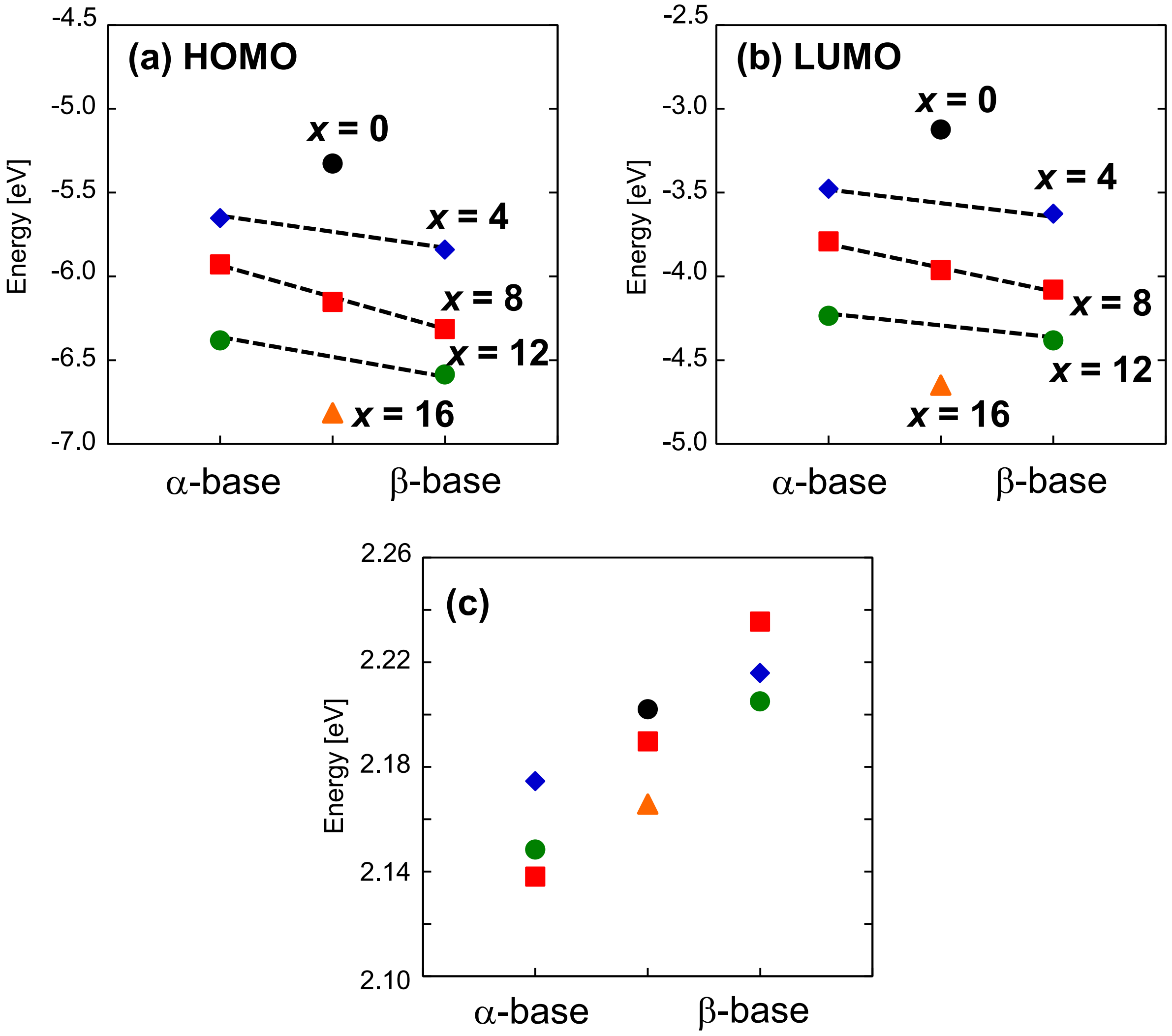

Fig. 3.6. (a) HOMO, (b) LUMO, and (c) HOMO-LUMO gap energies calculated for F_xCuPc (x = 0, 4, 8, 12, and 16). The horizontal axis indicates the position of fluorine atoms. The plots on the left-hand side labeled α-base correspond to F_4CuPc (α_1), F_8CuPc (α_1, α_2), and $F_{12}CuPc$ (α_1, α_2, β_1). The plots at the center correspond to CuPc, F_8CuPc (α_1, β_2), and $F_{16}CuPc$. The plots on the right-hand side labeled β-base correspond to F_4CuPc (β_1), F_8CuPc (β_1, β_2), and $F_{12}CuPc$ (α_1, β_1, β_2). Black circle: CuPc; blue diamonds: F_4CuPc; red squares: F_8CuPc; green circles: $F_{12}CuPc$; orange triangle: $F_{16}CuPc$.

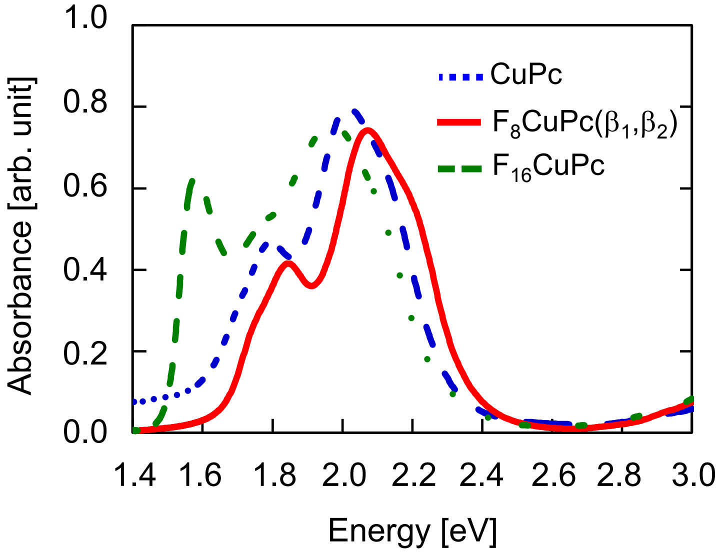

Fig. 3.7. Absorption spectra of CuPc, F_8CuPc (β_1, β_2), and F_{16}CuPc thin films on glass substrates.

Figure 3.8 shows the photoelectron yield spectra observed from the surfaces of CuPc, F_8CuPc (β_1, β_2), and F_{16}CuPc films. The threshold energy and shape in a photoelectron spectrum are generally related to the HOMO energy and density of states, respectively. The experimental HOMO energy is defined by fitting a line to a measured spectrum. The HOMO energies obtained from the spectra are −5.10 eV for CuPc, −6.15 eV for F_8CuPc, and −6.68 eV for F_{16}CuPc. On the other hand, the calculated HOMO energies are −5.33 eV for CuPc, −6.32 eV for F_8CuPc, and −6.82 eV for F_{16}CuPc. The experimental HOMO energies are higher than the calculated values. The differences are 0.23 eV for CuPc, 0.17 eV for F_8CuPc, and 0.14 eV for F_{16}CuPc. Since the experimental HOMO energy is affected by the interaction between molecules, the difference is probably due to the interaction. Calculations considering the interaction will improve the consistency.

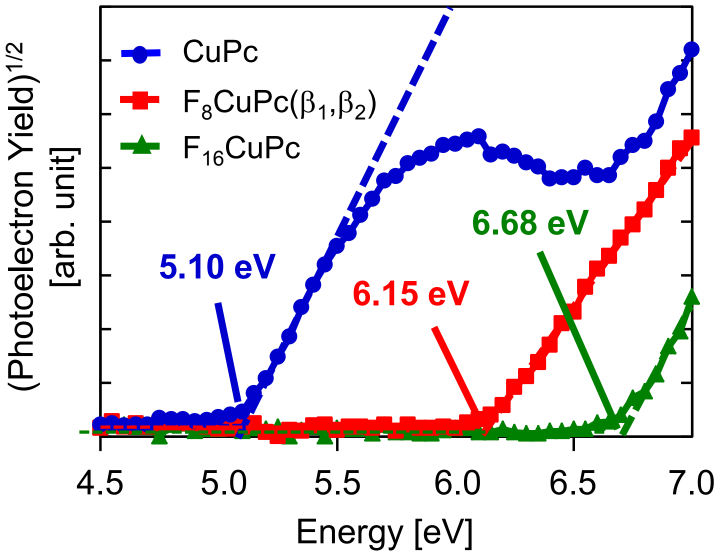

Fig. 3.8. Photoelectron yield spectra of CuPc, F_8CuPc (β_1, β_2), and F_{16}CuPc thin films on glass substrates. The values in the figure show the negative values of the experimental HOMO energy.

3.4 Conclusions

We investigated the electronic structures and vibrational structures of of F_xCuPc (x = 0, 4, 8, 12, and 16) by quantum chemical calculation. In particular, we focused on orbital energies. The calculated HOMO and LUMO levels depend on the number of fluorine atoms and their position on the benzene ring. For CuPc, F_8CuPc, and $F_{16}CuPc$, the calculated band gap energy and HOMO levels are consistent with the results of UV-visible absorption spectra and photoelectron ionization energies, respectively. The calculated HOMO energies range from −5.33 to −6.82 eV; the LUMO energies range from −3.12 to −4.65 eV. The variations in HOMO and LUMO levels are useful in the design of high-efficiency organic photovoltaics containing CuPc series.

3.5 References

1) Y. Galagen, I. G. Vries, A. P. Langen, R. Andriessen, W. J. H. Verhees, S. C. Veenstra, and J. M. Kroon: Chem. Eng. Process. **50** (2011) 454.
2) M. Granström, K. Petritsch, A. C. Arias, A. Lux, M. R. Andersson, and R. H. Friend: Nature **395** (1998) 257.
3) J. Y. Kim, K. Lee, N. E. Coates, D. Moses, T.-Q. Nguyen, M. Dante, and A. J. Heeger: Science **317** (2007) 222.
4) J. Jung, D. Kim, J. Lim, C. Lee, and S. C. Yoon: Jpn. J. Appl. Phys. **49** (2010) 05EB03.
5) F. C. Krebs, S. A. Gevorgyan, B. Gholamkhass, S. Holdcroft, C. Schlenker, M. E. Thompson, B. C. Thompson, D. Olson, D. S. Ginley, S. E. Shaheen, H. N. Alshareef, J. W. Murphy, W. J. Youngblood, N. C. Heston, J. R. Reynolds, S. Jia, D. Laird, S. M. Tuladhar, J. G. A. Dane, P. Atienzar, J. Nelson, J. M. Kroon, M. M. Wienk, R. A. J. Janssen, K. Tvingstedt, F. Zhang, M. Andersson, O. Inganäs, M. L.-Cantu, R. Bettignies, S. Guillerez, T. Aernouts, D. Cheyns, L. Lutsen, B. Zimmermann, U. Würfel, M. Niggemann, H.-F. Schleiermacher, P. Liska, M. Grätzel, P. Lianos, E. A. Katz, W. Lohwasser, and B. Jannon: Sol. Energy Mater. Sol. Cells **93** (2009) 1968.
6) B. C. Thompson and J. M. J. Fréchet: Angew. Chem., Int. Ed. **47** (2008) 58.
7) P. Morvillo and E. Bobeico: Sol. Energy Mater. Sol. Cells **92** (2008) 1192.
8) D. Patra, D. Sahu, H. Padhy, D. Kekuda, C.-W. Chu, K.-H. Wei, and H.-C. Lin: Macromol. Chem. Phys. **212** (2011) 1960.
9) T. Yamamoto, T. Ikai, M. Kuzuba, T. Kuwabara, K. Maeda, K. Takahashi, and S. Kanoh: Macromolecules **44** (2011) 6659.
10) J. C. Bijleveld, V. S. Gevaerts, D. D. Nuzzo, M. Turbiez, S. G. J. Mathijssen, D. M. Leeuw, M. M. Wienk, and R. A. J. Janssen: Adv. Mater. **22** (2010) E242.
11) E. A. Lawton: J. Phys. Chem. **62** (1958) 384.
12) F. Ghani, J. Kristen, and H. Riegler: J. Chem. Eng. Data **57** (2012) 439.
13) R. Ye, M. Baba, and K. Mori: Jpn. J. Appl. Phys. **44** (2005) L581.
14) D. Song, F. Zhu, B. Yu, L. Huang, Y. Geng, and D. Yan: Appl. Phys. Lett. **92** (2008) 143303.
15) F. Pan, H. Tian, X. Qian, L. Huang, Y. Geng, and D. Yan: Org. Electron. **12** (2011) 1358.
16) M.-S. Liao and S. Scheiner: J. Chem. Phys. **114** (2001) 9780.
17) M. Hanack and P. Stihler: Eur. J. Org. Chem. (2000) 303.

18) N. Kobayashi, H. Lam, W. A. Nevin, P. Janda, C. C. Leznoff, T. Koyama, A. Monden, and H. Shirai: J. Am. Chem. Soc. **116** (1994) 879.

19) X. Cai, Y. Zhang, X. Zhang, and J. Jiang: J. Mol. Struct.: THEOCHEM **801** (2006) 71.

20) L. Zhang, D. Qi, L. Zhao, Y. Bian, and W. Li: J. Mol. Graphics Model. **35** (2012) 57.

21) A. Ogunsipe, J.-Y. Chen, and T. Nyckong: New J. Chem. **28** (2004) 822.

22) U. Weiler, T. Mayer, W. Jaegermann, C. Kelting, D. Schlettwein, S. Makarov, and D. Wöhrle: J. Phys. Chem. B **108** (2004)19398.

23) W. Chen, H. Huang, S. Chen, Y. L. Huang, X. Y. Gao, and A. T. S. Wee: Chem. Mater. **20** (2008) 7017.

24) C. Shen and A. Kahn: J. Appl. Phys. **90** (2001) 4549.

25) H. Peisert, M. Knupfer, and J. Fink: Appl. Phys. Lett. **81** (2002) 2400.

26) Z. Bao, A. J. Lovinger, and J. Brown: J. Am. Chem. Soc. **120** (1998) 207.

27) M.-M. Ling, Z. Bao, and P. Erk: Appl. Phys. Lett. **89** (2006) 163516.

28) R. Koshy and C. S. Menon: E-J. Chem. **9** (2012) 2439.

29) R. Murdey, N. Sato, and M. Bouret: Mol. Cryst. Liq. Cryst. **455** (2006) 211.

30) H. Peisert, M. Knupfer, T. Schwieger, G. G. Fuentes, D. Olligs, J. Fink, and Th. Schmidt: J. Appl. Phys. **93** (2003) 9683.

31) H. Peisert, M. Knupfer, and J. Fink: Surf. Sci. **515** (2002) 491.

32) A. D. Becke: J. Chem. Phys. **98** (1993) 5648.

33) C. Lee, W. Yang, and R. G. Parr: Phys. Rev. B **37** (1988) 785.

34) Z. Liu, Z.-X. Chen, B. Jin, and X. Zhang: Vib. Spectrosc. **56** (2011) 210.

35) M. J. Frisch *et al.*: Gaussian 09, Revision B.01 (Gaussian, Inc., Wallingford CT, 2010).

36) K. Kanai, M. Honda, H. Ishii, Y. Ouchi, and K. Seki: Org. Electron. **13** (2012) 309.

37) P. N. Day, Z. Wang, and R. Pachter: J. Mol. Struct.: THEOCHEM **455** (1998) 33.

38) Z. Liu, X. Zhang, Y. Zhang, and J. Jiang: Spectrochim. Acta A **67** (2007) 1232.

39) C. J. Brown: J. Chem. Soc. A (1968) 2488.

40) D. Li, Z. Peng, L. Deng, Y. Shen, and Y. Zhou: Vib. Spectrosc. **39** (2005) 191.

41) T. Basova, E. Kol'tsov, A. Hassan, A. Tsargorodskaya, A. Ray, and I. Igumenov: Phys. Status Solidi B **242** (2005) 822.

42) A. A. M. Farag: Opt. Laser Technol. **39** (2007) 728.

43) P. C. Minor, M. Gouterman, and A. B. P. Lever: Inorg. Chem. **24** (1985) 1894.

Chapter 4

Electronic Structure and Spectra of Fluorinated Copper Phthalocyanine Dimer: Quantum Chemical Study

4.1 Introduction

Metal phthalocyanines have attracted a great deal of attention for a wide variety of application, such as solar cells,[1-3] organic light emitting diodes as hole transport layer or buffer layer,[4,5] field effect transistors,[6-10] and gas sensors.[11] Also, substituted phthalocyanines have received attention because modification of phthalocyanines is effective technique to change their properties.[12] In paticular, since a substitution of the peripheral hydrogen of phthalocyanines by halogen atoms leads to a decrease in the energy level,[13-17] halogenated phthalocyanines are promising materials in terms of a control technique of energy levels of organic materials. Copper phthalocyanine (CuPc) is one of the most typical phthalocyanine. Halogenated phthalocyanines, such as hexadecafluoro copper phthalocyanine (F_{16}CuPc) and hexadecachloro copper phthalocyanine (Cl_{16}CuPc), are known as n-type semiconductiors.[18-21] In halogenation, fluorination is the most effective to decrease the energy level in halogenation because fluorine atom has strong electron-withdrawing ability.

The importance of theoretical investigation for prediction of properties of organic materials is well-known. The electronic structure of a CuPc and a fluorinated CuPc molecule has been studied theoretically.[22,23] However, an organic film consists of a lot of molecules. An organic film structure readily changes depending on the conditions in a film formation process. The properties of an organic film such as absorption spectra in ultraviolet-visible wavelength region, which is one of the important properties of organic semiconductors, are significantly related to the film structure due to intermolecular interaction. Therefore, the theoretical investigation including intermolecular interaction is desirable. The examination about dimer simply clarifies the electronic properties including intermolecular interaction because dimer is a minimum unit of a multimolecular structure.

In this chapter, we theoretically studied about the F_xCuPc (x=0, 8, and 16) monomer and dimer based on quantum chemical calculation. The electronic structures of them were investigated. In particular, we focus on the influence of the dimerization on the absorption spectra in ultraviolet-visible wavelength region in F_xCuPc (x = 0 and 8).

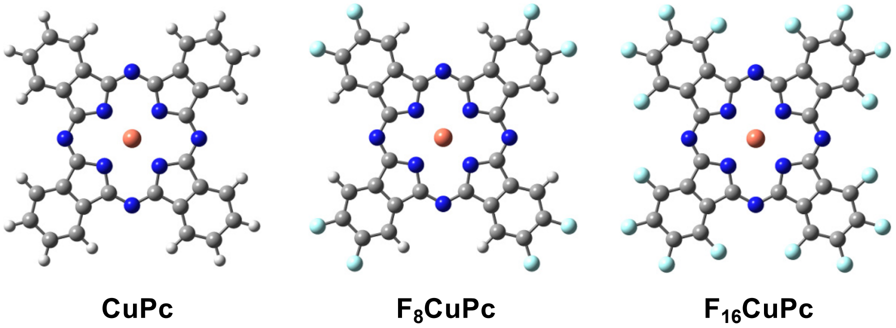

Fig. 4.1. Molecular structure of F_xCuPc (x=0, 8, and 16).

4.2 Computational details

The structures of F_xCuPc (x = 0, 8, and 16), which are calculated monomer molecule, are shown in Fig. 4.1. All fluorine atoms of F_8CuPc are at the far position (β-position) of benzene ring from molecular center. The structural optimization of F_xCuPc monomer were carried out by a hybrid density functional theory method combining the Becke three-parameter exchange functional and Lee-Yang-Parr correlation functional (B3LYP) using the LanL2DZ basis set.[24,25] To describe the potential energy surface (PES) of F_xCuPc dimer, single point calculation using optimized monomer structure was performed by semi-empirical method PM6. Figure 4.2 shows a model structure of CuPc dimer for single point calculation. In Fig. 4.2, the atomic structure of CuPc dimer is depicted by side view (upper part) and top view (under part) as example. The two π-conjugate planes of dimer molecule were placed parallel to each other. The Cu atom of one molecule was set as origin and a line from copper to outer nitrogen of the one molecule was set as x-axis. Also, the position of one molecule was fixed. The π-conjugated planes were consistently parallel to xy plane. Then, the position of the other molecule was changed keeping the π-conjugated planes parallel to each other. The center (Cu atom) position of the other molecule was changed from 0.0 to 5.0 Å per 0.2 Å, from 0.0 to 5.0 Å per 0.2 Å, and from 3.0 to 4.0 Å per 0.2 Å, for x, y, and z-direction, respectively. We performed the single point calculation with PM6 level about all the dimer structure to obtain the total energy at each structure. From obtained energies, the PESs were described. The optimization of F_xCuPc (x = 0, 8, and 16) dimer was also performed at the some low-energy position in PES with fixed monomer structure.

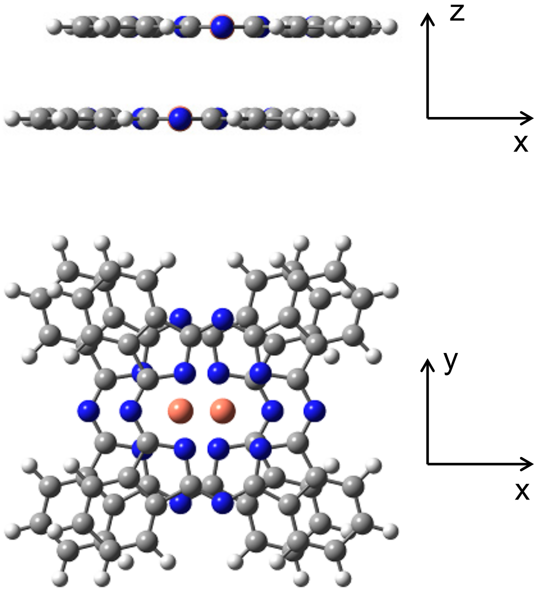

Fig. 4.2. Model structure of CuPc dimer. The atomic structure of CuPc dimer is depicted by side view (upper part) and top view (under part).

For CuPc and F_8CuPc dimer, the excitation energy calculation by time-dependent-CAM-B3LYP method with LanL2DZ basis set was performed on the basis of the experimental structures. The experimental structure of F_8CuPc film was unknown. Therefore, both CuPc and F_8CuPc dimer structures for calculation were used the experimentally known α- and β-CuPc structures as reference.[26)] That is, for α-F_xCuPc (x = 0 and 8) dimer structures for calculation, the two Cu atoms were positioned at the position of Cu atoms of experimental α-CuPc, and the orientation of ligand part were coordinated with experimental α-CuPc ligand. The optimized structures of CuPc and F_8CuPc monomer were used for α-CuPc and α-F_8CuPc dimer for calculation, respectively. For β-F_xCuPc (x = 0 and 8) dimer structures for calculation are same. As reference, the excitation energy calculation about CuPc and F_8CuPc monomer was also performed. The Gaussian 09 program package was used for the all calculation.[27)]

4.3 Results

4.3.1 F_xCuPc (x= 0, 8, and 16) monomer

All optimized structure of F_xCuPc (x = 0, 8, and 16) have D_{4h} symmetry with planar π-conjugate plane. The D_{4h} symmetry of CuPc optimized structures are reported in literature.[28,29)] The bond length and bond angle of the optimized structures are shown in Fig. 4.3. The bond length in this work is slightly larger than experimental value. The calculation results indicate that the fluorination causes the slight structural defomation. The maximum difference in bond length and in bond angle are 0.012 Å at C_α-C_β (between CuPc and F_8CuPc) and 3.0° at H_α (F_α)-C_α-C_β (between CuPc and $F_{16}CuPc$), respectively. C_α (C_β) represents the carbon bound to H or F at α- (β-)position. H_α or F_α represents the hydrogen or fluorine at α-position.

Figure 4.4 shows molecular orbitals of F_xCuPc (x = 0, 8, and 16) monomer. Each LUMO and HOMO have e_g and a_{1u} symmetry, respectively. The HOMO and LUMO energies decrease with an increase in the number of fluorine atoms. The HOMO and LUMO energies range from -5.33 to -6.82 eV and from -3.12 to -4.65 eV, respectively.

4.3.2 Potential energy surfaces of F_xCuPc (x = 0, 8, and 16) dimer

Figures 4.5–4.7 show the PES of CuPc, F_8CuPc, and $F_{16}CuPc$, respectivety. The PES at z = 3.0 Å are not shown due to the considerably higher energy throughout the PES than the PES at other z value. The optimized low energy dimer positions are indicated in Table 4.1. Figs. 4.5–4.7 show that the low energy positions exist in F_xCuPc (x =0, 8, and 16) PES along the lines of the y (or x) = 0 and y = x. Although the energy at around (x, y) = (4.0, 0.0) is comparable (only from 13 to 43 meV larger) to the minimum energy in the $F_{16}CuPc$ PES, the PES of CuPc and F_8CuPc do not have the low energy point at around (x, y) = (4.0, 0.0). This is indicated that the influence of fluorine atom has not appeared by octa-fluorination but appeared by hexadeca-fluorination of CuPc. The experimental positions of α-CuPc, β-CuPc, and $F_{16}CuPc$ dimer correspond to (1.6, 0.0, 3.4), (3.4, 0.0, 3.4), and (3.8, 0.0, 3.1), respectively.[26)] As the experimental position of CuPc and $F_{16}CuPc$ dimer are along the lines of y = 0, the calculation results are quantitatively consistent with experimental results. The quantitative difference between experiment and calculation result is presumably due to the influence of non-nearest neighbor molecules or the calculation level.

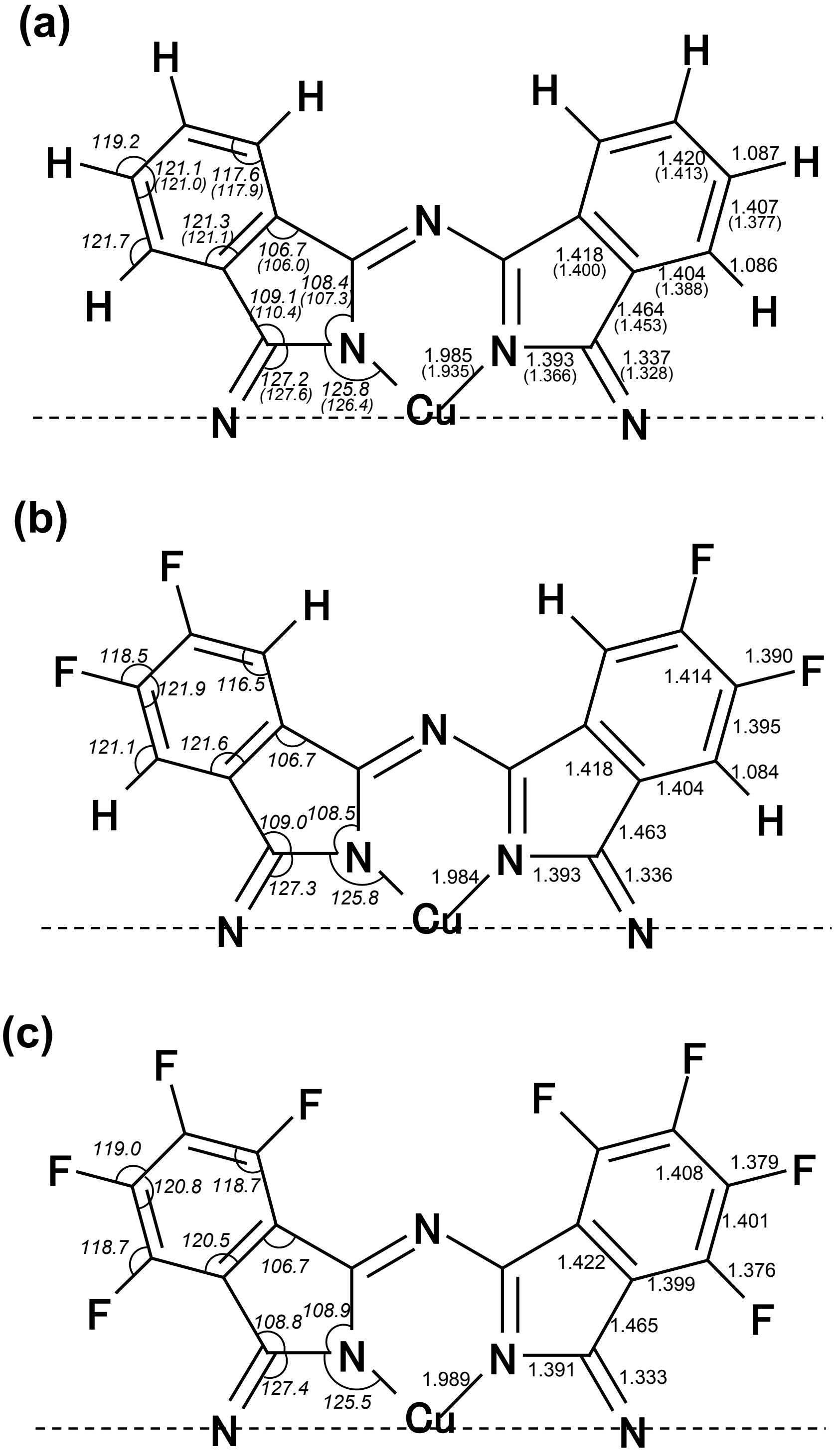

Fig. 4.3. Bond length (in Å) and bond angle (in degree) of the optimized structures of (a) CuPc, (b) F_8CuPc, and (c) $F_{16}CuPc$.

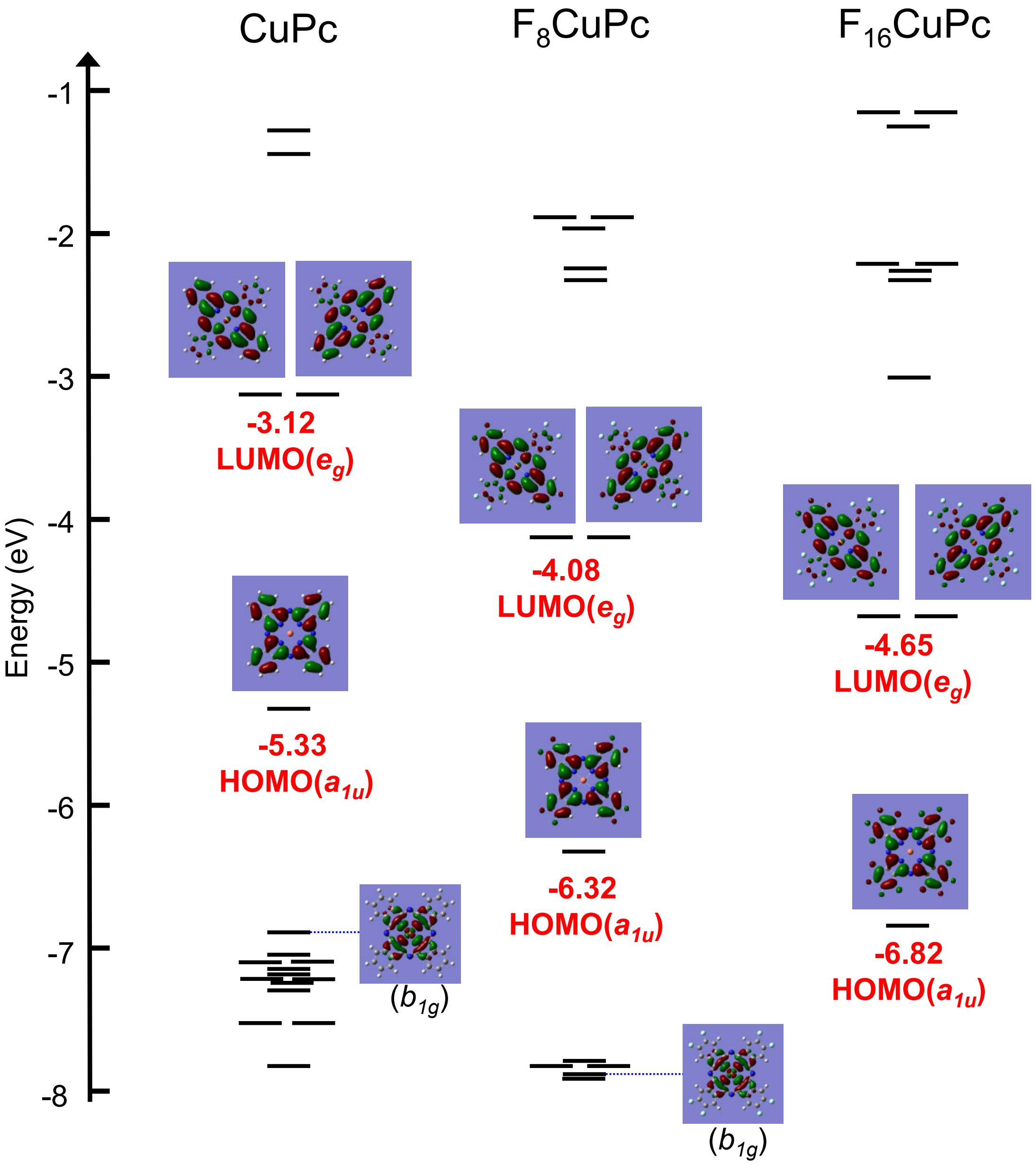

Fig. 4.4. Molecular orbitals of F_xCuPc (x = 0, 8, and 16) monomer.

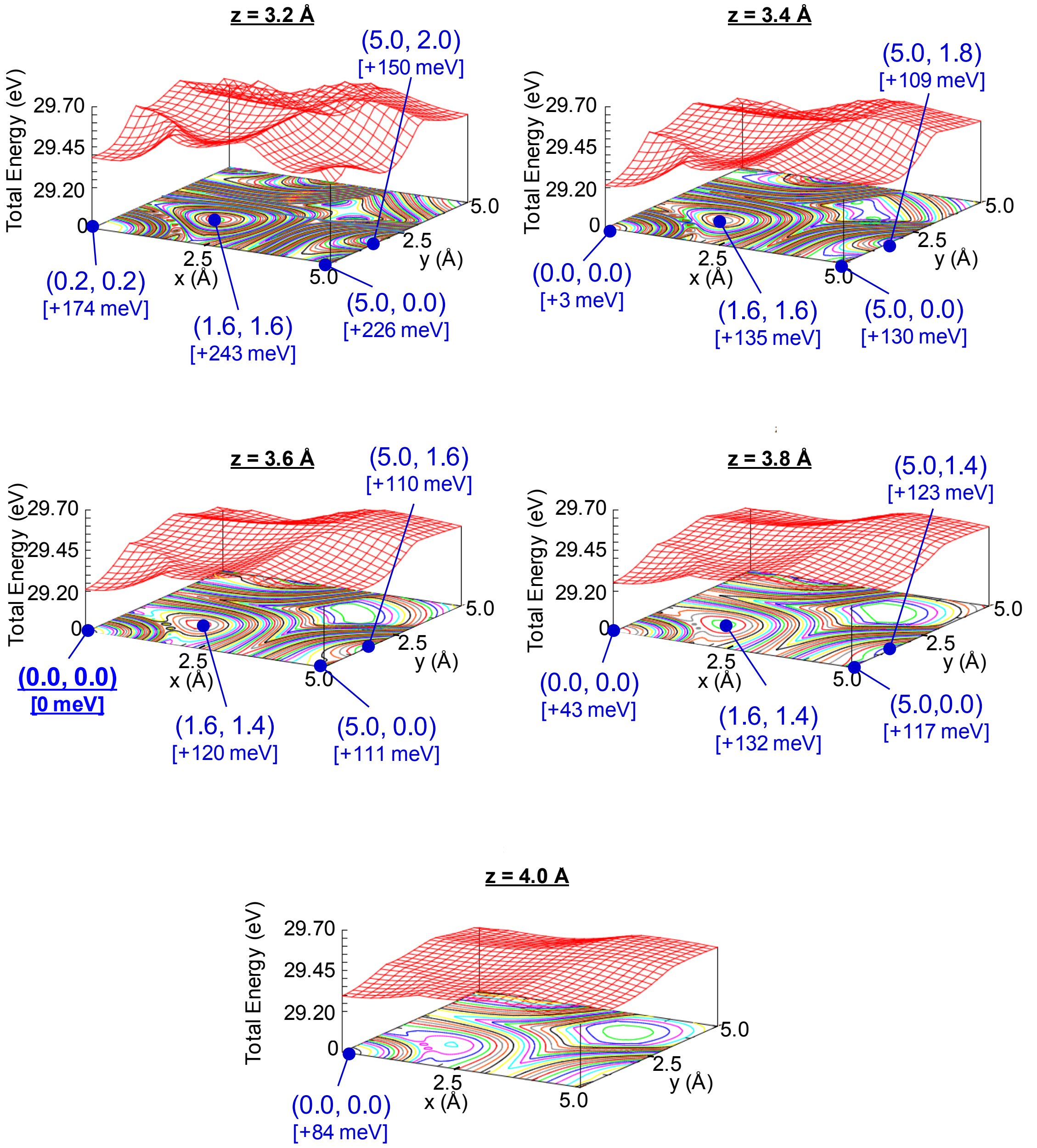

Fig. 4.5. Potential energy surfaces of CuPc dimer. Contour is described at intervals of 5 meV.

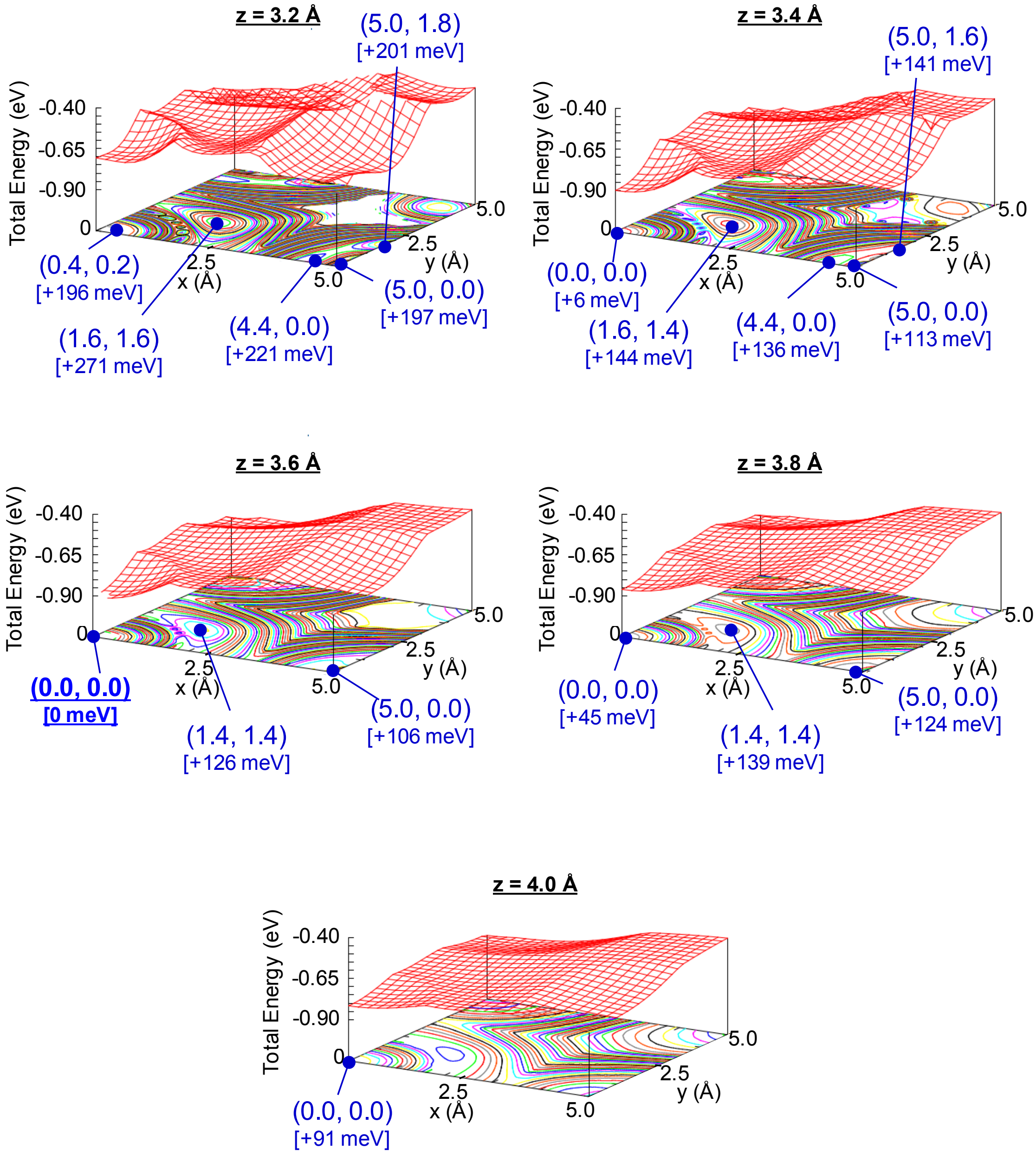

Fig. 4.6. Potential energy surfaces of F_8CuPc dimer. Contour is described at intervals of 5 meV.

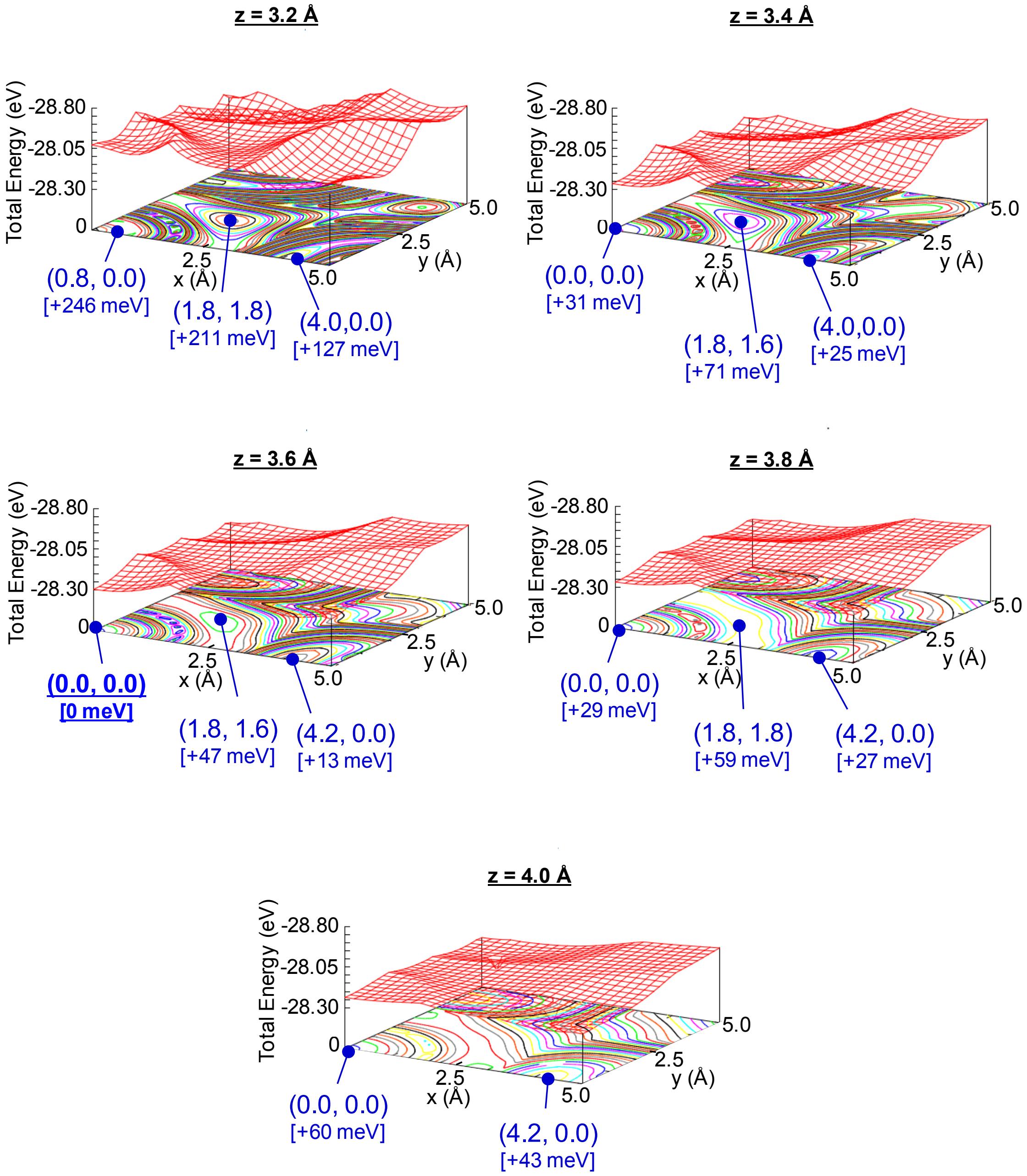

Fig. 4.7. Potential energy surfaces of $F_{16}CuPc$ dimer. Contour is described at intervals of 5 meV.

Table 4.1. Optimized positions of F_xCuPc (x=0, 8, and 16) dimer.

	CuPc		F_8CuPc		$F_{16}CuPc$	
	Position (x , y, z) (Å)	ΔE_{tot} (meV)	Position (x , y, z) (Å)	ΔE_{tot} (meV)	Position (x , y, z) (Å)	ΔE_{tot} (meV)
1 (most stable)	(0.00, 0.00, 3.55)	0.0	(6.27, 0.00, 3.31)	0.0	(4.12, 0.00, 3.53)	0.0
2	(7.63, 1.73, 3.35)	94.4	(1.08, 1.09, 3.59)	63.1	(0.00, 0.00, 3.56)	56.1
3	(1.56, 1.52, 3.56)	197.4	(0.00, 0.00, 3.50)	83.1	(1.69, 1.69, 3.59)	104.6

4.3.3 Influence of dimerization on absorption spectra

Figures 4.8 and 4.9 show the calculated molecular orbital diagrams of CuPc and F_8CuPc dimer, respectively. For all calculated F_xCuPc (x = 0 and 8) dimer, the LUMO is copper derived orbital, and from the LUMO+1 to LUMO+4 are ligand derived orbital. For occupied orbitals of calculated dimer, although the HOMO of β-phase are metal derived orbital, the HOMO-1 and HOMO-2 of β-phase and the HOMO-2 of α-phase are ligand derived orbital. The HOMO-1 of both α-CuPc and α-F_8CuPc are ligand derived orbital but slightly mixed with metal state. The HOMO of α-CuPc is mixed orbital of metal and ligand state, and the HOMO of α-F_8CuPc is basically metal derived orbital. For from the LUMO+1 to LUMO+4 of CuPc and F_8CuPc dimer, the degree of orbital energy splitting of β-phase is larger than α-phase. The splitting energy of α-CuPc, β-CuPc, α-F_8CuPc, and β-F_8CuPc are 68, 145, 84, and 113 meV, respectively.

Excitation energies and oscillator strengths of CuPc and F_8CuPc dimer are represented in Tables 4.2 and 4.3, respectively. The transition with large oscillator strength (> 0.1) in CuPc and F_8CuPc dimer are based on the π-π* (ligand-to-ligand) transition. The absorption spectra in presented region are known as the Q-band.[30)] CuPc monomer with D_{4h} symmetry has the π-π* transition with E_u symmetry at 2.06 eV with oscillator strength of 0.44. On the other hand, the π-π* transitions of CuPc dimer are divided into two groups. One is the transitions in lower energy region from 2.03 to 2.10 eV derived from $1A_u$ and $1B_u$ transitions, the other is the transitions in higher energy region from 2.20 to 2.29 eV derived from $3A_u$ and $3B_u$ transitions. E_u symmetry in D_{4h} of CuPc monomer correspond the A_u and B_u symmetry in C_{2h} of CuPc dimer. The transition splitting into lower or higher energy regions in CuPc dimer is due to splitting of unoccupied ligand derived orbitals (from LUMO+1 to LUMO+4) and of occupied ligand derived orbitals (HOMO-1 and HOMO-2), and the transition energies depend on the degree of orbital energy splitting. In lower energy region, the transition energies and the oscillator strength of β-CuPc are smaller and larger than α-CuPc, respectively. In higher energy region, the transition energies and the oscillator strength of β-CuPc are larger and smaller than α-CuPc, respectively. The previous experimental study has shown the absorption spectra of CuPc film have the same tendency with calculation results in this study.31) For F_8CuPc, monomer with D_{4h} symmetry has the π-π* transition with E_u symmetry at 2.14 eV with oscillator strength of 0.43. The π-π* transitions of F_8CuPc dimer are also divided into two groups. $2A_u$ and $1B_u$ transitions of α-phase or $1A_u$ and $2B_u$ transitions of β-phase are in lower energy region from 2.08 to 2.12 eV, and $3A_u$ transitions are in higher energy region from 2.21 to 2.29 eV. The dependence of changing of the transition energies and the oscillator strength is similar to CuPc case. The research of optical property about F_8CuPc film has not been sufficiently investigated. However, if phase transformation similar to CuPc in F_8CuPc film arises, this result indicates that the similar change of absorption spectra of F_8CuPc film with CuPc is observed.

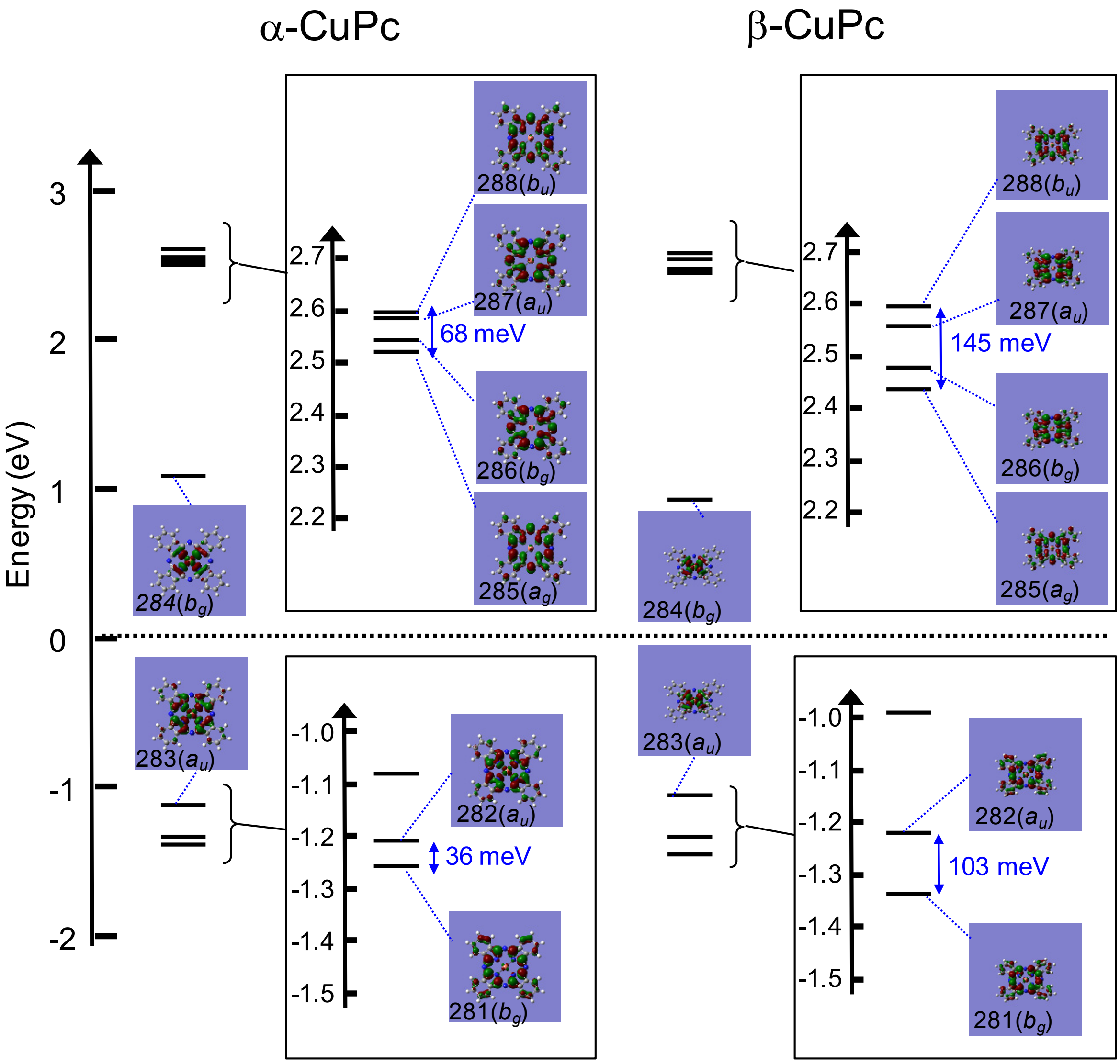

Fig. 4.8. Calculated molecular orbital diagrams of CuPc dimer. The number described in the orbital figure show the orbital number. The intermediate value between HOMO and LUMO is set as zero.

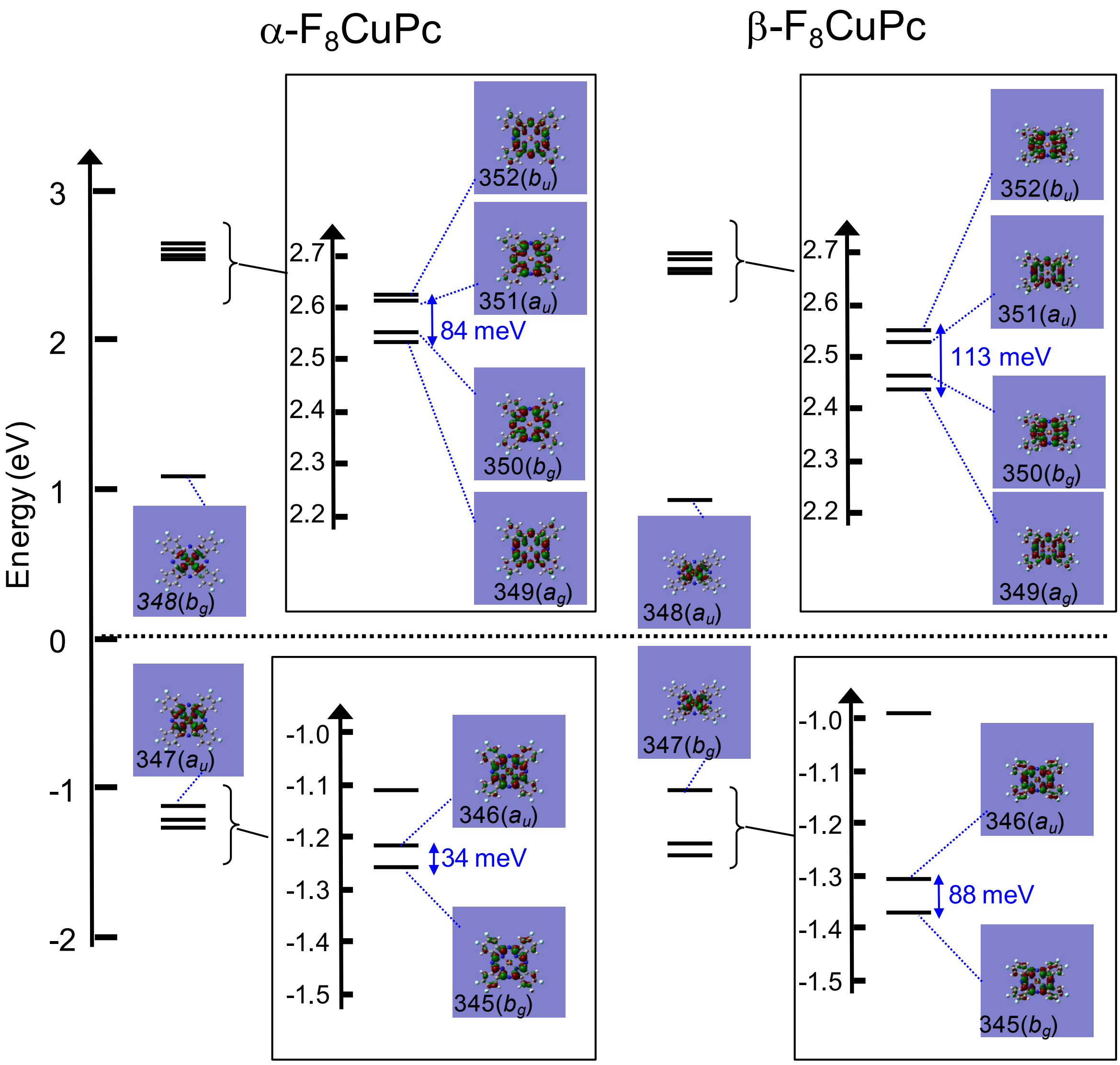

Fig. 4.9. Calculated molecular orbital diagrams of F_8CuPc dimer. The number described in the orbital figure show the orbital number. The intermediate value between HOMO and LUMO is set as zero.

Table 4.2. Excitation energies and oscillator strengths of CuPc dimer

	Transition	Energy (eV)	*f*
α-CuPc			
$1A_u$	282(a_u)→285(a_g) (46%) 283(a_u,HOMO) → 285(a_g) (37%)	2.034	0.203
$1B_u$	282(a_u)→286(b_g) (47%) 283(a_u,HOMO)→286(b_g) (40%)	2.098	0.513
$2A_u$	276(b_u)→284(b_g,LUMO) (48%) 282(a_u)→285(a_g) (31%)	2.113	0.063
$2B_u$	281(b_u) →287(a_u) (63%)	2.120	0.050
$3A_u$	281(b_g) →288(b_u) (68%)	2.195	0.291
β-CuPc			
$1B_u$	282(a_u) →286(a_g) (60%)	2.026	0.482
$1A_u$	282(a_u) →285(a_g) (58%)	2.046	0.330
$2A_u$	277(b_u)→284(b_g,LUMO) (41%) 279(b_u)→284(b_g,LUMO) (39%)	2.109	0.086
$2B_u$	276(a_u)→284(b_g,LUMO) (54%)	2.112	0.037
$3B_u$	281(b_g) →287(a_u) (64%)	2.276	0.112
$3A_u$	281(b_g) →288(b_u) (67%)	2.290	0.149

Table 4.3. Excitation energies and oscillator strengths of F$_8$CuPc dimer.

	Transition	Energy (eV)	*f*
α-F$_8$CuPc			
$1A_u$	339(b_u)→348(a_g,LUMO) (53%)	2.026	0.065
$2A_u$	346(a_u)→349(a_g) (55%) 339(a_u)→348(a_g, LUMO) (31%)	2.095	0.218
$1B_u$	346(a_u)→350(b_g) (49%) 345(b_g)→351(a_u) (31%)	2.118	0.497
$2B_u$	337(a_u)→348(b_g,LUMO) (49%)	2.172	0.037
$3B_u$	345(b_g) →351(a_u) (61%) 346(a_u) →350(b_g) (32%)	2.179	0.034
$3A_u$	345(b_g) →352(b_u) (68%)	2.214	0.259
β-F$_8$CuPc			
$1B_u$	340(b_g) →348(a_u,LUMO) (61%)	2.002	0.032
$2B_u$	346(a_u) →350(b_g) (58%)	2.077	0.499
$1A_u$	346(a_u) →349(a_g) (49%)	2.083	0.261
$2A_u$,	346(a_u)→349(a_g) (42%) 338(a_g)→348(a_u,LUMO) (41%)	2.135	0.156
$3A_u$	345(b_g)→352(b_u) (65%)	2.290	0.119
$3B_u$	345(b_g) →351(a_u) (62%) 346(a_u) →350(b_g) (31%)	2.302	0.079

4.4 Conclusions

We investigated the electronic structure of F_xCuPc (x = 0, 8, and 16) monomer and dimer by quantum chemical calculation. The HOMO and LUMO energy levels of monomer are dependent on a number of fluorine atoms. For dimer aligned the π-conjugated plane of one molecule parallel to the other, the potential energy surfaces are obtained. The calculated potential energy surfaces show that the parallel displacement of one molecule along the line from copper to inner nitrogen of the other molecule or the line from copper to outer nitrogen of it leads to low energy position. The excited state calculation about CuPc dimer explains the absorption spectra difference between α- and β-CuPc films by intermolecular interaction. The difference of excitation energy and oscillator strength by phase transformation of F_8CuPc film is predicted. The results and methodology in this study are helpful for estimation of properties of organic semiconductor layer or for application of CuPc based organic semiconductor layer for organic devices.

4.5 References

1) C. W. Tang: Appl. Phys. Lett. **48** (1986) 183.
2) P. Peumans, V. Bulovi, and S. R. Forrest: Appl. Phys. Lett.: **76** (2000) 2650.
3) F. Yang, M. Shtein, and S. R. Forrest: Nature Materials **4** (2005) 37.
4) J. Blochwitz, M. Pfeiffer, T. Fritz, and K. Leo: Appl. Phys. Lett. **73** (1998)729.
5) P. –C. Kao, S. –Y. Chu. Z. –X. You, S. J. Liou, and C. –A. Chuang: Thin Solid Films **498** (2006) 249.
6) R. B. Chaabane, A. Ltaief, C. Dridi, H. Rahmouni, A. Bouazizi, and H. B. Ouada: Thin Solid Films **427** (2003) 371.
7) J. Zhang, H. Wang, X. Yan, J. Wang, J. Shi, and D. Yan: Adv. Mater. **17** (2005) 1191.
8) J. Wang, H. Wang, X. Yan, H. Huang, and D. Yan: Appl. Phys. Lett. **87** (2005) 093507.
9) Q. Tang, H. Li, M. He, W. Hu, C. Liu, K. Chen, C. Wang, Y. Liu, and D. Zhu: Adv. Mater. **18** (2006) 65.
10) R. W. I. Boer, A. F. Stassen, M. F. Craciun, C. L. Mulder, A. Molinari, S. Rogge, ans A. F. Morpurgo: Appl. Phys. Lett. **86** (2005) 262109.
11) M. Bouvet: Anal. Bioanal. Chem. **384** (2006) 366.
12) E. A. Cueller and T. J. Marks: Inorg. Chem. **20** (1981) 3766.
13) X. Cai, Y. Zhang, X. Zhang, and J. Jiang: J. Mol. Struct.: THEOCHEM **801** (2006) 71.
14) U. Weiler, T. Mayer, W. Jaegermann, C. Kelting, D. Schlettwein, S. Makarov, and D. Wöhrle: J. Phys. Chem. B **108** (2004)19398.
15) W. Chen, H. Huang, S. Chen, Y. L. Huang, X. Y. Gao, and A. T. S. Wee: Chem. Mater. **20** (2008) 7017.
16) C. Shen and A. Kahn: J. Appl. Phys. **90** (2001) 4549.
17) H. Peisert, M. Knupfer, and J. Fink: Appl. Phys. Lett. **81** (2002) 2400.
18) R. Ye, M. Baba, and K. Mori: Jpn. J. Appl. Phys. **44** (2005) L581.
19) Z. Bao, A. J. Lovinger, and J. Brown: J. Am. Chem. Soc. **120** (1998) 207.
20) M.-M. Ling, Z. Bao, and P. Erk: Appl. Phys. Lett. **89** (2006) 163516.
21) R. Koshy and C. S. Menon: E-J. Chem. **9** (2012) 2439.
22) Y. Kuzumoto, H. Matsuyama, and M. Kitamura: to be published in Jpn. J. Appl. Phys.
23) M.-S. Liao and S. Scheiner: J. Chem. Phys. **114** (2001) 9780.
24) A. D. Becke: J. Chem. Phys. **98** (1993) 5648.

25) C. Lee, W. Yang, and R. G. Parr: Phys. Rev. B **37** (1988) 785.

26) A. C. Cruickshank, C. J. Dotzler, S. Din, S. Heutz, M. F. Toney, and M. P. Ryan: J. Am. Chem. Soc. **134** (2012) 14302.

27) M. J. Frisch *et al.*: Gaussian 09, Revision B.01 (Gaussian, Inc., Wallingford CT, 2010).

28) P. N. Day, Z. Wang, and R. Pachter: J. Mol. Struct.: THEOCHEM **455** (1998) 33.

29) Z. Liu, X. Zhang, Y. Zhang, and J. Jiang: Spectrochim. Acta A **67** (2007) 1232.

30) P. C. Minor, M. Gouterman, and A. B. P. Lever: Inorg. Chem. **24** (1985) 1894.

31) W. Y. Tong, A. B. Djurišić, M. H. Xie, A. C. M. Ng, K. Y. Cheung, W. K. Chan, Y. H. Leung, H. W. Lin, and S. Gwo: J. Phys. Chem. B **110** (2006) 17406.

Chapter 5

Structural and Electrical Properties of Fluorinated Copper Phthalocyanine toward Organic Photovoltaics: Post-Annealing Effect under Pressure

5.1 Introduction

There has been growing interest in organic photovoltaics (OPVs) because of their innovative device features such as light weight, large area, and flexible.[1-5] The phthalocyanine series is a promising group of materials for OPVs because of its high chemical and thermal stability.[6-10] Copper phthalocyanine (CuPc) is a well-known p-type semiconductor material among phthalocyanines.[11,12] The fluorination of phthalocyanines leads to a decrease in energy level depending on the number of fluorine atoms.[13-19] It has been reported that organic transistors having hexadecafluoro CuPc (F_{16}CuPc) as a channel material operate as n-channel transistors. [8,20] This indicates that F_{16}CuPc works as an n-type semiconductor. Octafluoro CuPc (F_8CuPc) is also expected to be n-type semiconductor due to its lower energy levels than CuPc.

The use of CuPc and F_{16}CuPc or F_8CuPc is associated with the simple fabrication of pn junction diodes and their application in photovoltaic cells. In fact, devices with a CuPc/F_{16}CuPc hetero junction have been investigated.[21,22] However, the CuPc/F_{16}CuPc devices reported in Refs. 21 and 22 showed reverse rectifying characteristics, that is, the current at a negative voltage applied to the CuPc layer is larger than that at a positive voltage. The reason for these characteristics remains unclear. From the fabrication conditions and results described, it seems that the structure of F_{16}CuPc is related to the characteristics of CuPc/F_{16}CuPc devices.

Substrate temperature and post-annealing for the deposition of organic layers affect the properties of organic films. The effect of temperature on the mobility or morphology of typical organic semiconductors such as pentacene or poly(3-hexylthiophene) (P3HT) films has been extensively investigated.23-27) For CuPc thin films, several studies have also shown that deposition or annealing at higher temperatures transforms the crystalline phase from the α-phase to the β-phase and changes the electronic or optical properties.28-34) However, there have been only a few reports about the properties of F_{16}CuPc films deposited on a heated substrate and annealed.21)

In this chapter, we have investigated the effects of substrate temperature and post-annealing on the properties of CuPc, F_{16}CuPc, and CuPc/F_{16}CuPc films to examine the potential of F_{16}CuPc to OPVs. The influence of substrate temperature on properties of F_8CuPc film was also investigated.

5.2 Experimental

The molecular structures of compounds used in this study are shown in Fig. 1. Copper phthalocyanine purified by train sublimation was used and sublimation-grade F_{16}CuPc was purchased and used as received without further purification.

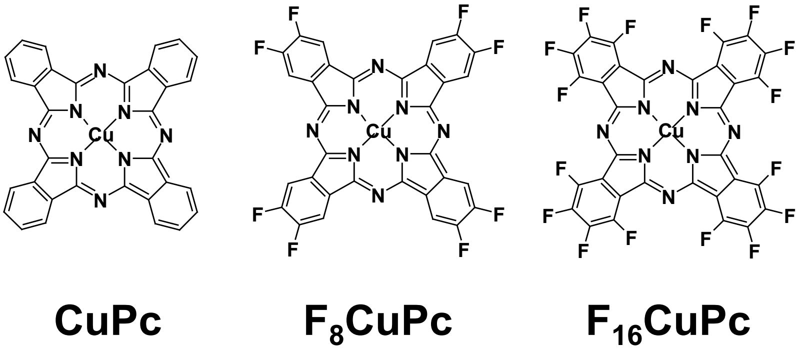

Fig. 5.1. Molecular structures of CuPc, F_8CuPc, and F_{16}CuPc.

A glass substrate coated with a 150-nm-thick indium-tin-oxide (ITO) layer was used for all the samples. The substrate was treated with O_2 plasma to increase its work function. Then, organic films of CuPc, F_8CuPc, F_{16}CuPc, and CuPc/F_{16}CuPc were deposited on the substrate by thermal evaporation at a rate of 0.02 nm/s. The thickness of the CuPc, F_8CuPc, and F_{16}CuPc layers was 120 nm. Thus, the total thickness of the CuPc/F_{16}CuPc bilayer was 240 nm. The substrate temperature T_s during the deposition of organic layers was room temperature (RT) or 120 ˚C for some of the samples; T_s was gradually elevated from RT to 120 ˚C after the start of deposition for the other samples. Some substrates with CuPc, F_{16}CuPc, and CuPc/F_{16}CuPc layers deposited at T_s = 120 ˚C were annealed at a temperature of T_a = 300 ˚C for 2 h on a hot plate in a nitrogen-filled glove box before the deposition of a silver electrode. Other substrates with CuPc, F_{16}CuPc, and CuPc/F_{16}CuPc layers deposited at T_s = RT were annealed at T_a = 300 ˚C for 1 h under a pressure of 4.1 MPa using an EVG520HE hot embossing system of the EV Group. The schematic diagram for the preparation of the pressure-applied films is shown in Fig. 5.2. A stainless steel plate with a PTFE sheet was used to apply pressure to the surface of an organic layer on a substrate. For samples electrically characterized, a silver metal layer was deposited through a metal mask having 0.25-mm^2-area holes as an upper electrode.

The morphology of the organic layer deposited on the substrate was characterized by scanning electron microscopy (SEM) and atomic force microscopy (AFM). The crystallinity of the organic layer was investigated using the X-ray diffraction (XRD) patterns obtained in the $\theta - 2\theta$ mode with CuKα radiation. The current-voltage characteristics were measured in the dark or under illumination in a glove box using a semiconductor device parameter analyzer.

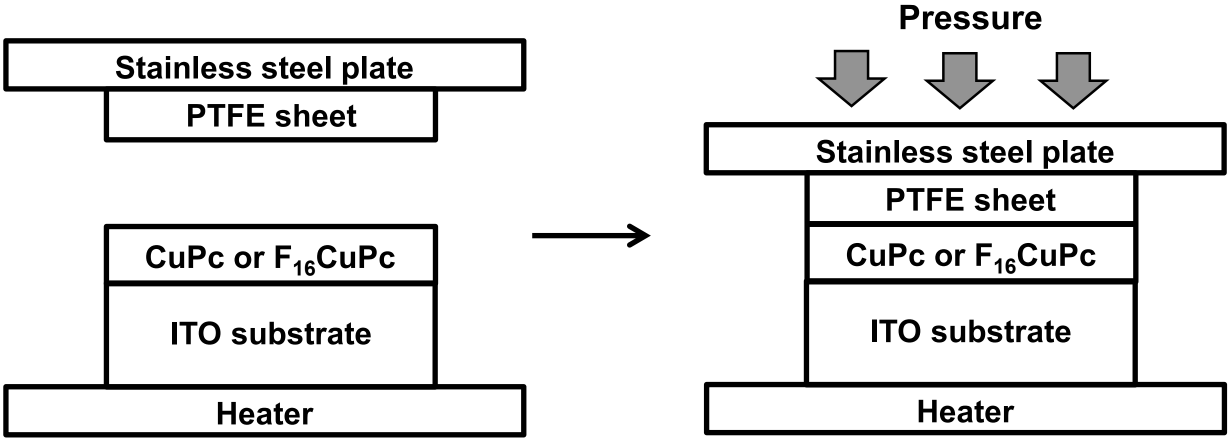

Fig. 5.2. Schematic diagram of substrate heating under applied pressure.

5.3 Results

5.3.1 Structural properties of CuPc and F_{16}CuPc

Figure 5.3 shows SEM images of the CuPc and $F_{16}CuPc$ films deposited on substrates prepared under different conditions. Although the surface morphology of the CuPc and $F_{16}CuPc$ films was also examined by AFM, the rough surface of $F_{16}CuPc$ films prepared under certain conditions obstructed the AFM observation of the surface. Thus, SEM images are shown in this manuscript, and AFM images obtained for some samples that are shown in Fig. 5.4 were used for the estimation of root mean square roughness (RMS). The CuPc films deposited at T_s = RT and 120 ˚C have a smooth surface as compared with the other samples. The RMS values of these films are 4.9 and 4.1 nm, respectively. On the other hand, the CuPc films post-annealed at 300 ˚C with or without additional pressure have crystal-like domains, and their RMS values are 3.8 and 6.0 nm, respectively. The $F_{16}CuPc$ films have a very rough surface as compared with the CuPc films. Needle-like structures are present in the films under all the examined conditions. In particular, substrate heating and post-annealing without additional pressure enhance surface roughness. The rough surfaces of the $F_{16}CuPc$ films in Figs. 5.3(e)-5.3(g) prevented the AFM observation. On the other hand, additional pressure during post-annealing planarized the $F_{16}CuPc$ films, as shown in Fig. 5.3(h). The RMS of the $F_{16}CuPc$ film is 9.1 nm, which is slightly larger than those of the CuPc films. Also, substrate heating at T_s elevated from RT suppresses surface roughness, as shown in Fig. 5.3(i). Schematic illustrations of the $F_{16}CuPc$ films in Figs. 5.3(e)-5.3(g) and 5.3(h) are shown in Figs. 5.5(a) and 5.5(b), respectively.

The XRD patterns of the CuPc and $F_{16}CuPc$ films are shown in Fig. 5.6. The diffraction peaks at $2\theta = 6.7^\circ$ of CuPc and $2\theta = 6.0^\circ$ of $F_{16}CuPc$ correspond to interplane spacings of d = 13.2 and 14.7 Å, respectively. The spacings are close to those reported in earlier studies.20,33) Peak intensity increases with substrate temperature. This result indicates that substrate heating improves the crystallinity of CuPc and $F_{16}CuPc$ thin films. Since substrate heating up to 120 ˚C does not change the surface morphology of a CuPc film, as shown in Figs. 5.6(a) and 5.6(b), the result of the XRD analysis implies that we can improve the crystallinity of the CuPc film without changing the surface morphology.

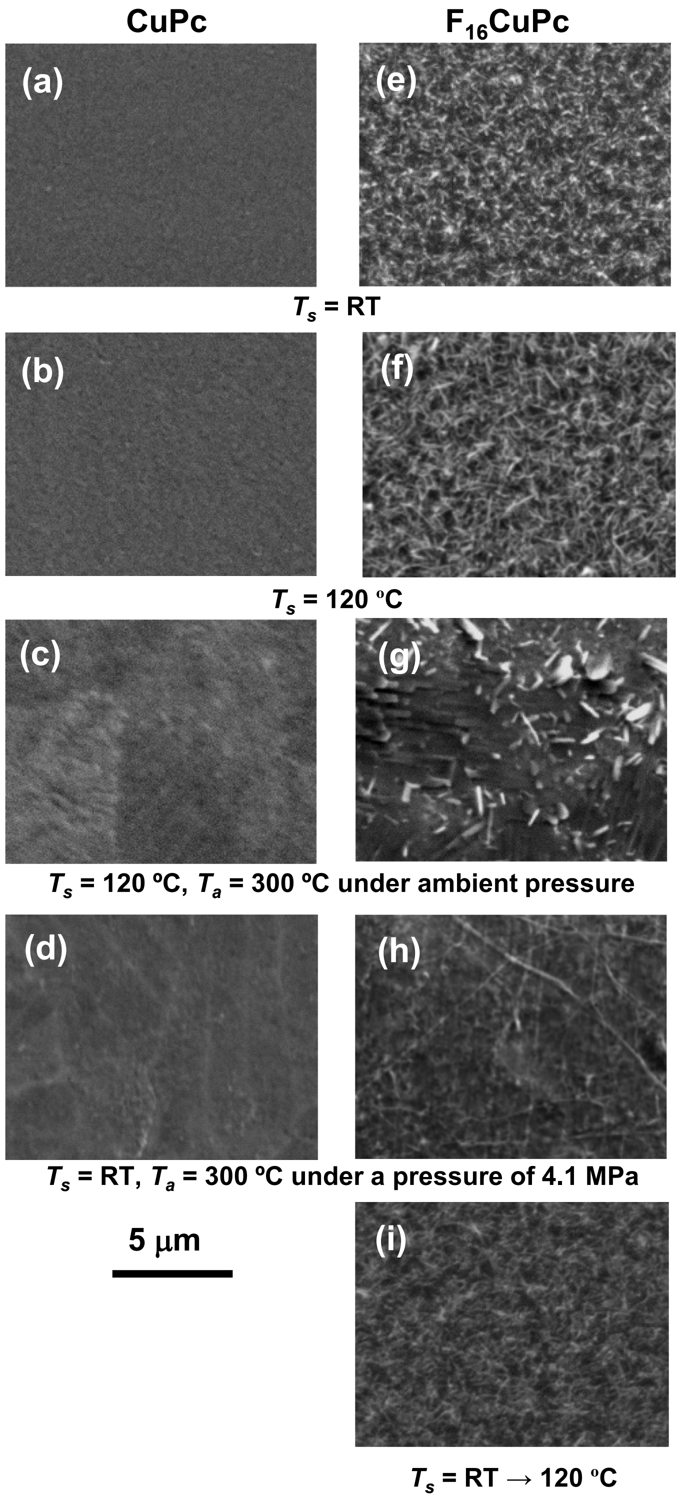

Fig. 5.3. SEM images of (a)-(d) CuPc and (e)-(i) $F_{16}CuPc$ films. The films were deposited at (a, d, e, h) room temperature and (b, c, f, g) 120 ˚C. For (i), substrate temperature was gradually increased from RT to 120 ˚C. The samples for (c) and (g) were annealed at 300 ˚C after deposition without additional pressure. The samples for (d) and (h) were annealed at 300 ˚C under a pressure of 4.1 MPa.

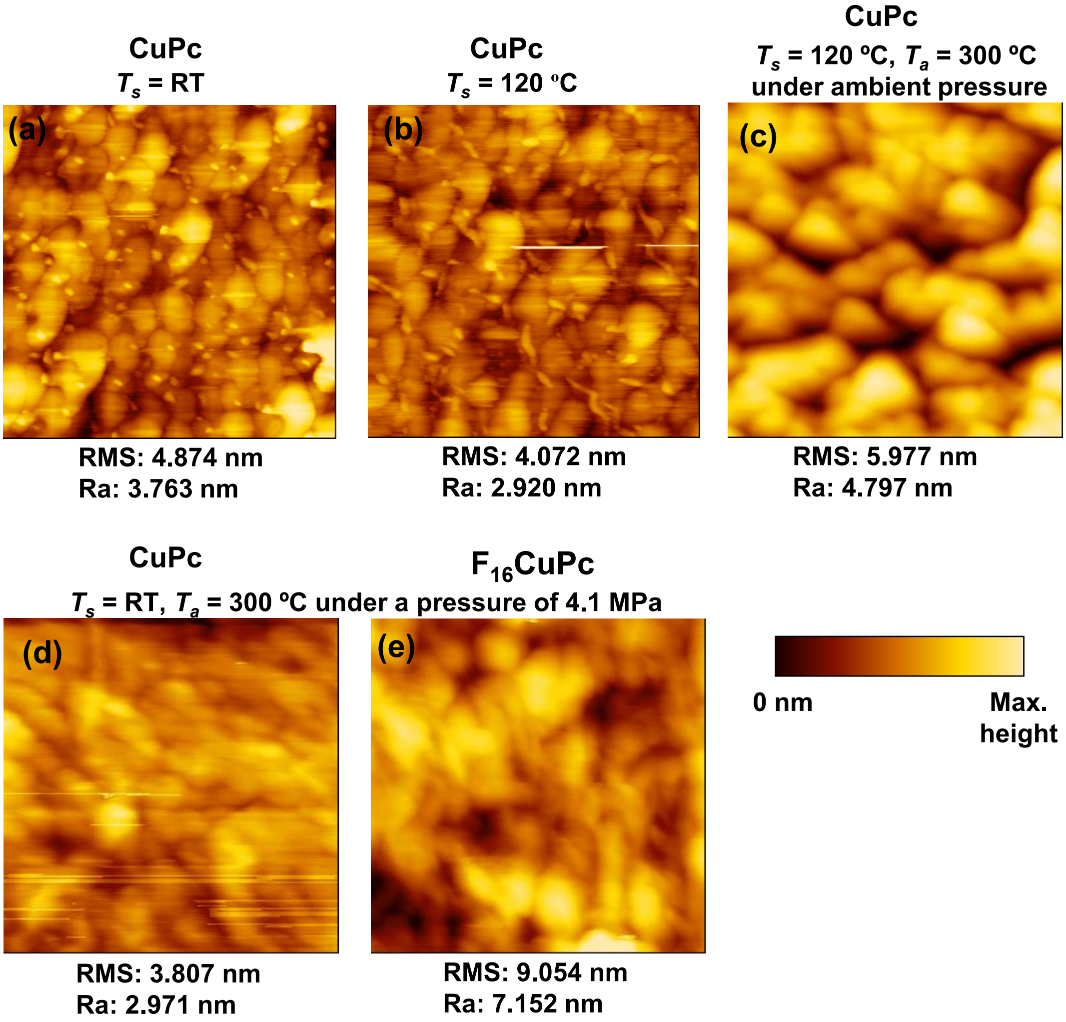

Fig. 5.4. AFM images of (a)-(d) CuPc and (e) F_{16}CuPc films. The films were deposited at (a, d, e) room temperature and (b, c) 120 ˚C. The sample for (c) was annealed at 300 ˚C after deposition without additional pressure. The samples for (d) and (e) were annealed at 300 ˚C under a pressure of 4.1 MPa. The total image size is 1 × 1 μm^2. The maximum height represented in AFM images are (a)-(d) 30 nm and (e) 50 nm.

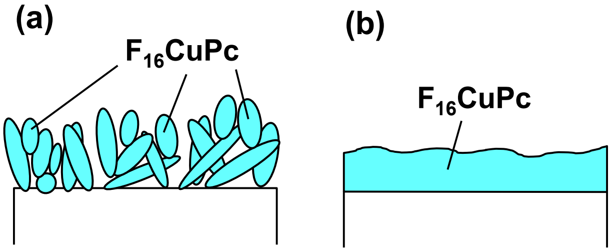

Fig. 5.5. Schematic illustration of $F_{16}CuPc$ films with (a) needle-like structure and (b) smooth surface.

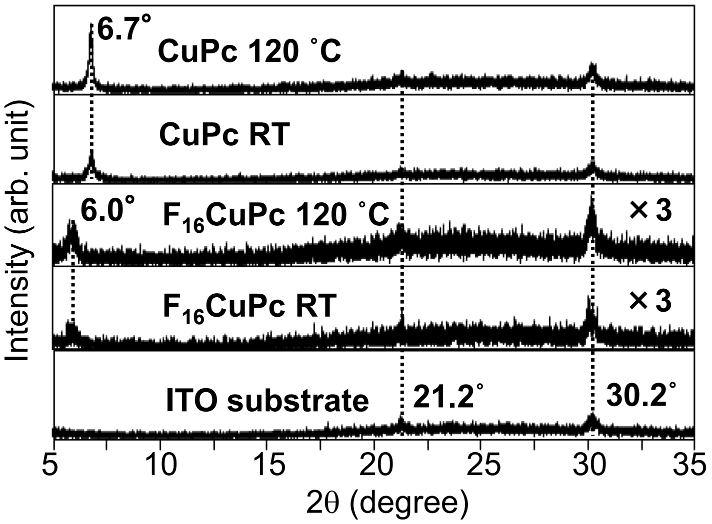

Fig. 5.6. XRD patterns of CuPc and $F_{16}CuPc$ films deposited on ITO substrates at RT and 120 ˚C. An XRD pattern for an ITO substrate is also shown as reference.

5.3.2 Electrical properties of CuPc and $F_{16}CuPc$

The structure of the CuPc and $F_{16}CuPc$ single-layer devices for electrical measurement is shown in Fig. 5.7 (a). The current-voltage characteristics of the CuPc devices are shown in Fig. 5.7(b). For the CuPc device of T_s = 120 ˚C, the current at the positive voltage applied to the ITO electrode is larger than that at the negative voltage, and the rectification property is confirmed in the CuPc device. On the other hand, the CuPc device of T_s = RT has a low current as compared with the device of T_s = 120 ˚C. In addition, the current increase at the negative voltage leads to breakdown. As a result, substrate heating contributes to clear rectifying characteristics. The difference in the current characteristics is probably attributed to the crystallinity of the CuPc films depending on substrate temperature.

Figure 5.7(c) shows the current-voltage characteristics of the F_{16}CuPc devices without post-annealing. Many of the devices with F_{16}CuPc layers deposited at T_s = RT and 120 ˚C broke down at voltages of over ±0.5 V. This is probably due to thin areas in the F_{16}CuPc layer with a three-dimensional structure, as shown in Figs. 5.3(e) and 5.3(f). On the other hand, the devices with F_{16}CuPc layers at T_s gradually elevated from RT to 120 ˚C operated at voltages of up to ±1.0 V, as shown in Fig. 5.7(c). This implies that gradual heating reduces surface roughness and suppresses electrically weak areas in the F_{16}CuPc layer. The explanation is consistent with the flat surface of F_{16}CuPc shown in Fig. 5.3(i) as compared with those shown in Figs. 5.3(e) and 5.3(f). The current-voltage characteristics exhibit rectification property. However, the current at the negative voltage applied to the ITO electrode is larger than that at the positive voltage. Since a F_{16}CuPc layer generally works as an n-type semiconductor, the rectification property in Fig. 5.7(c) indicates that electrons in the F_{16}CuPc layer are transported from the ITO electrode rather than from the Ag electrode. This suggests that the Ag electrode has a high work function as compared with the ITO electrode. The reason for this high work function is discussed in the last paragraphs of this section.

Figure 5.7(d) shows the current-voltage characteristics of a single-layer device with F_{16}CuPc post-annealed at 300 ˚C under pressure. The current-voltage characteristics exhibit clear rectification property. The rectification ratio in Fig. 5.7(d) improves as compared with that in Fig. 5.7(c). This is because the current at the positive voltage in Fig. 5.7(d) was suppressed. The suppression is probably attributed to a reduction of the thin areas in the F_{16}CuPc layer, causing current leakage. Another difference between the current-voltage characteristics in Figs. 5.7(c) and 5.7(d) is in the absolute value of current. The absolute value of current at −1 V in Fig. 5.7(d) is about 80 $\mu A/cm^2$, which is about 1/10000 of that in Fig. 5.7(c).

The F_{16}CuPc devices prepared at T_s gradually elevated from RT to 120 ˚C exhibit a current value of about −1 A/cm^2 at −1 V, as shown in Fig. 5.7(c). The result indicates that the substantial thickness of the F_{16}CuPc layer is less than the designed thickness of 120 nm. A device with a 25-nm-thick CuPc layer has shown a similar current value.35) Although the current characteristics of an organic single-layer device generally depend on the carrier mobility of the organic layer, the thickness of 25 nm for the CuPc layer in Ref. 35 provides an indication of the substantial thickness of the F_{16}CuPc layer. The reason for the small substantial thickness is the three-dimensional structure shown in Fig. 5.5(a). Another reason is the diffusion of Ag atoms into the F_{16}CuPc layer. It has been suggested that Au atoms diffuse into a F_{16}CuPc layer within about 6 nm from the interface of Au and F_{16}CuPc.36) Since Ag atoms have similar properties with Au atoms, it is possible that Ag atoms diffuse into a F_{16}CuPc layer.

In Figs. 5.7(c) and 5.7(d), the current at the negative voltage is larger than that at the positive voltage. This is due to the high work function of Ag on a F_{16}CuPc layer. 37-40) To confirm this explanation, we measured the work function of a Ag film covered with a 2-nm-thick F_{16}CuPc layer by photoelectron spectroscopy. The work function obtained was 5.08 eV, which is high as compared with the normal work function of Ag. The change in the work function implies the presence of a dipole moment at the interface of the F_{16}CuPc and Ag layers. We calculated the atomic charges of a Ag-F_{16}CuPc model structure by quantum chemical calculation using PM6 method to predict the charge distribution between a F_{16}CuPc molecule and a Ag atom. In this model, a Ag atom was positioned directly above the Cu atom of a F_{16}CuPc molecule and the distance between the Ag atom and the Cu atom was set at 2.5 Å. The calculation showed that the atomic charges at the Ag atom and F_{16}CuPc molecule are +0.591 and −0.591 in atomic unit, respectively. This result supports the presence of a dipole moment at the interface of the F_{16}CuPc and Ag layers.

5.3.3 Structural and electrical properties of F_8CuPc

The XRD patterns of the F_8CuPc film deposited at $T_s = 120$ ˚C are shown in Fig. 5.8(a). The diffraction peaks at $2\theta = 6.4^\circ$ of F_8CuPc correspond to interplane spacings of $d = 13.8$ Å. The spacings are between spacings of $d = 13.2$ Å ($2\theta = 6.7^\circ$) of CuPc and $d = 14.7$ ($2\theta = 6.0^\circ$) of F_{16}CuPc (Fig. 5.6). The peak intensity at $2\theta = 6.4^\circ$ of F_8CuPc is smaller than that at $2\theta = 6.7^\circ$ of CuPc and $2\theta = 6.0^\circ$ of F_{16}CuPc in Fig. 5.6. This result indicates that F_8CuPc film has more amorphous-like structure than CuPc and F_{16}CuPc films.

All of the devices with F_8CuPc layers deposited at $T_s = 120$ ˚C exhibited no rectification property due to very large leak current and broke down at voltages of over plus or minus few hundred mV. This is probably due to thin areas in the F_8CuPc layer with a three-dimensional structure. On the other hand, the devices with F_8CuPc layers at T_s gradually elevated from RT to 120 ˚C operated at voltages of up to ±0.4 V and slightly exhibited rectification property, as shown in Fig. 5.8(b). This implies that gradual heating reduces surface roughness and suppresses electrically weak areas in the F_8CuPc layer, as is the case in F_{16}CuPc (Fig. 5.7(c)). However, the operating voltage in the devices with F_8CuPc layer is smaller than that in the devices with F_{16}CuPc layer. This implies that F_8CuPc layer probably has a more three-dimensional surface than F_{16}CuPc layer.

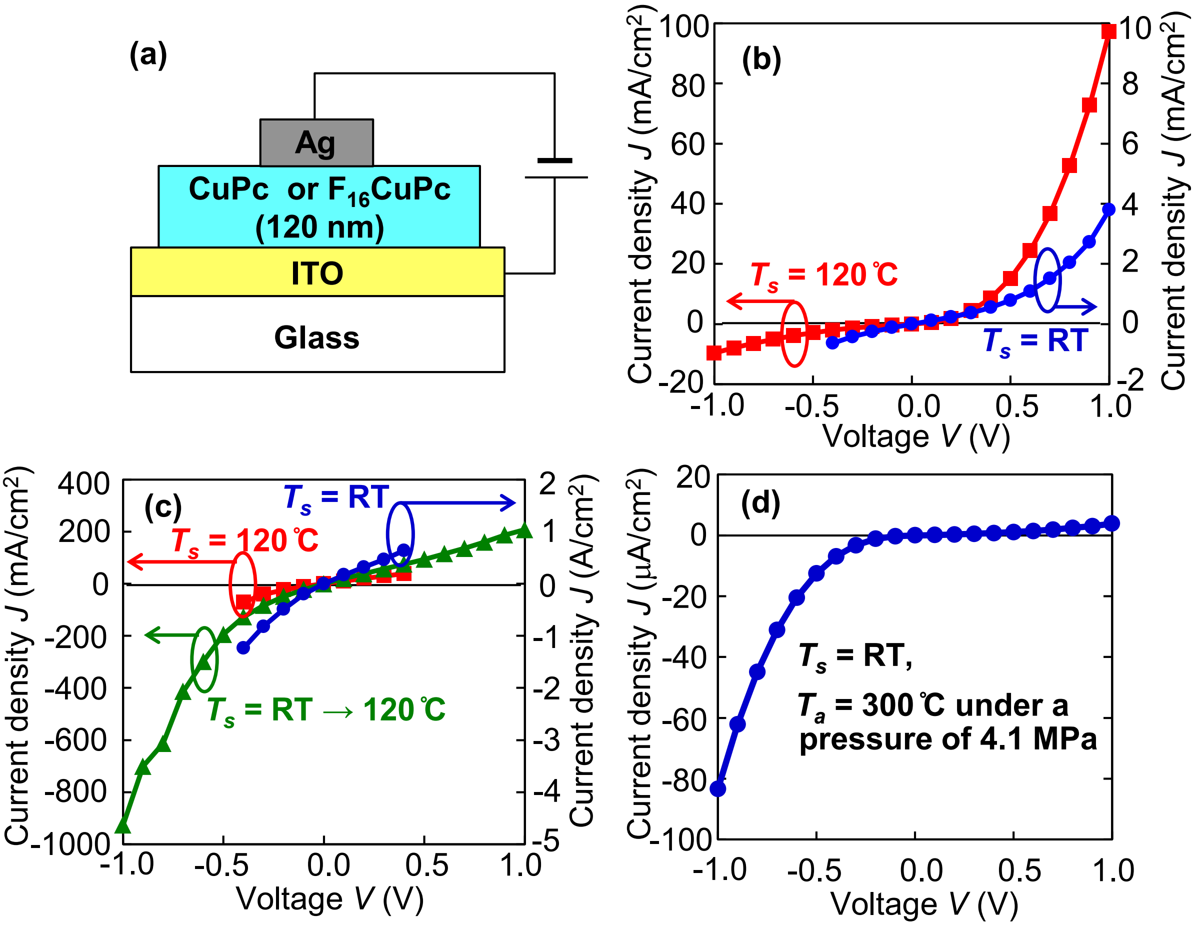

Fig. 5.7. Current-voltage characteristics of (a) CuPc and (b, c) F_{16}CuPc single-layer devices.

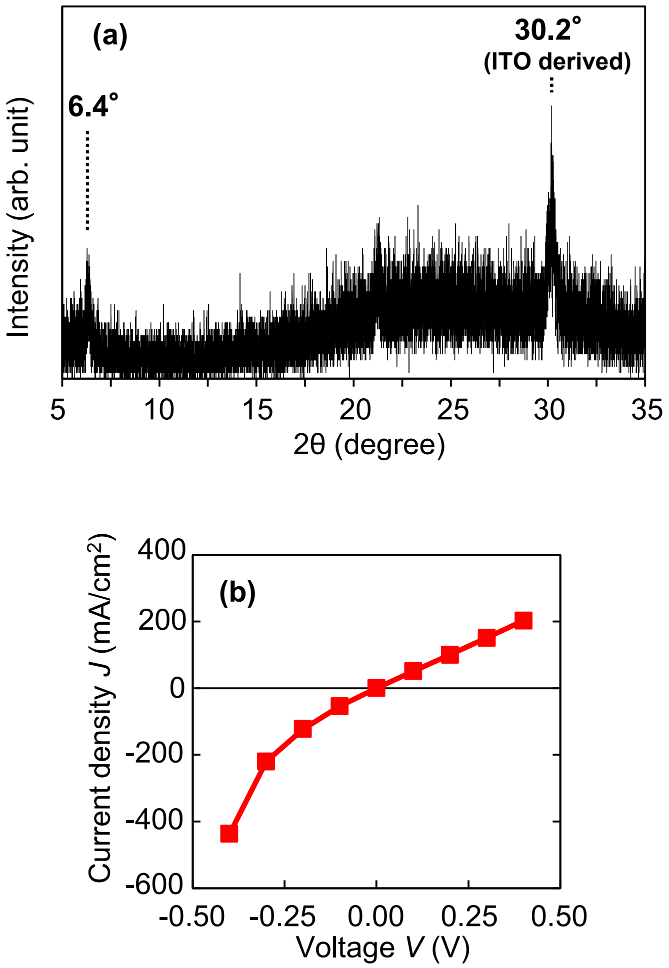

Fig. 5.8. (a) XRD patterns of F_8CuPc films deposited on ITO substrates and (b) current-voltage characteristics of F_8CuPc single-layer devices.

5.3.4 Electrical properties of CuPc/F_{16}CuPc

Figure 5.9 shows the current-voltage characteristics of the CuPc/F_{16}CuPc devices. The device structure is shown in the inset in Fig. 5.9(a). The device with CuPc/F_{16}CuPc layers deposited at T_s = 120 ˚C shows a reverse rectifying property, that is, the current at negative voltages applied to the electrode connected to a p-type semiconductor is larger than that at positive voltages. This result is in agreement with those of earlier studies.[21,22] In addition, the device showed no photovoltaic property under illumination. The reverse rectifying property is probably because the F_{16}CuPc layer leads to an increase in the work function of the Ag electrode as well as of the F_{16}CuPc single-layer device, and a thin F_{16}CuPc area works as a modifier of work function rather than as an n-type semiconductor. The band diagram for the device is schematically shown in Fig. 5.9(b). The superscripts $\delta-$ and $\delta+$ for F_{16}CuPc and Ag represent the charge distributions described in Sect. 5.3.2. The dipole moment caused by the charge distribution increases the work function of the Ag electrode. As a result, the device with the CuPc/F_{16}CuPc layers shows a reverse rectifying property.

On the other hand, the device with the CuPc/F_{16}CuPc layers, which were deposited at T_s = RT, and then annealed at 300 ˚C under pressure, exhibits the rectification and photovoltaic property shown in Fig. 5.9(c). A schematic band diagram for ITO/CuPc/F_{16}CuPc/Ag layers without consideration of band bending is shown in Fig. 5.9(d) as reference. The result indicates that the CuPc/F_{16}CuPc layers work as a pn junction diode. This suggests that post-annealing under pressure improves the flatness of the F_{16}CuPc layer, and reduces the thin F_{16}CuPc area. It is possible that the optimization of the device structure and fabrication conditions will lead to improvement in photovoltaic properties.

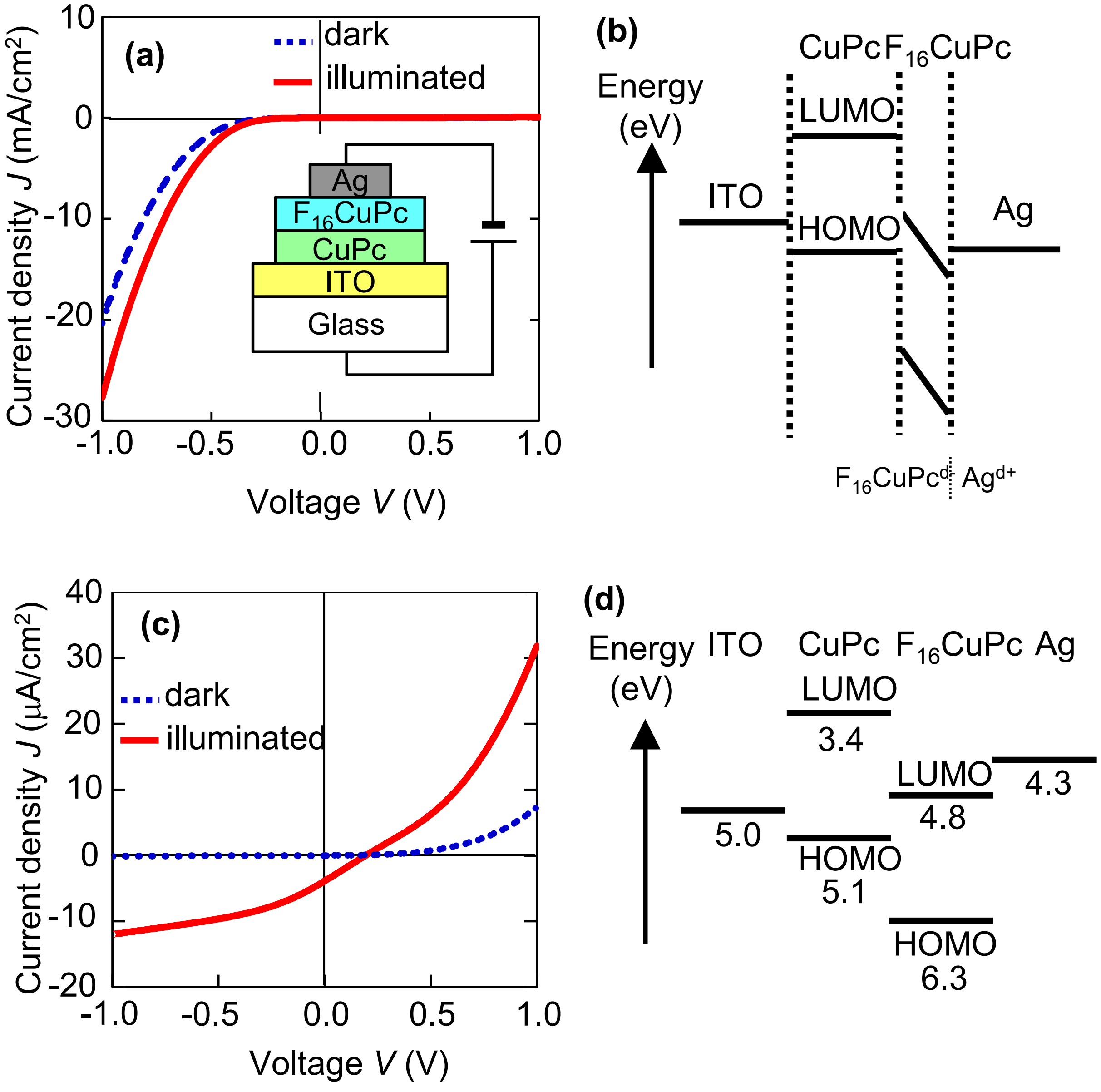

Fig. 5.9. Current-voltage characteristics of CuPc/F$_{16}$CuPc double-layer devices. The sample for (a) was deposited at 120 ˚C. The sample for (c) was deposited at room temperature, then annealed at 300 ˚C under a pressure of 4.1 MPa. The schematic band diagrams of samples (a) and (c) are shown in (b) and (d), respectively.

5.4 Conclusions

We investigated the effects of substrate temperature and post-annealing on the structural and electrical properties of CuPc, F_8CuPc, and F_{16}CuPc single-layer films and CuPc/F_{16}CuPc bilayer films. A single-layer device with a CuPc film deposited at 120 ˚C exhibited a superior rectifying property to that with a film deposited at RT. Substrate heating from RT during deposition reduced the surface roughness and improved the rectifying property of F_8CuPc and F_{16}CuPc devices. Post-annealing under additional pressure for the F_{16}CuPc and CuPc/F_{16}CuPc devices markedly improved the rectifying property. In particular, the CuPc/F_{16}CuPc devices worked as a pn junction diode and provided photocurrent under illumination. Post-annealing under pressure is useful for improving the electric characteristics of organic semiconductor films having a rough surface.

5.5 References

1) M. Granström, K. Petritsch, A. C. Arias, A. Lux, M. R. Andersson, and R. H. Friend: Nature 395 (1998) 257.

2) J. Y. Kim, K. Lee, N. E. Coates, D. Moses, T.-Q. Nguyen, M. Dante, and A. J. Heeger: Science 317 (2007) 222.

3) Y. Galagen, I. G. Vries, A. P. Langen, R. Andriessen, W. J. H. Verhees, S. C. Veenstra, and J. M. Kroon: Chemical Engineering and Processing 50 (2011) 454.

4) J. Jung, D. Kim, J. Lim, C. Lee, and S. C. Yoon: Jpn. J. Appl. Phys. 49 (2010) 05EB03.

5) F. C. Krebs, *et al.*: Sol. Energy Mater. Sol. Cells 93 (2009) 1968.

6) E. A. Lawton: J. Phys. Chem. 62 (1958) 384.

7) F. Ghani, J. Kristen, and H. Riegler: J. Chem. Eng. Data 57 (2012) 439.

8) R. Ye, M. Baba, and K. Mori: Jpn, J. Appl. Phys. 44 (2005) L581.

9) D. Song, F. Zhu, B. Yu, L. Huang, Y. Geng, and D. Yan: Appl. Phys. Lett. 92 (2008) 143303.

10) F. Pan, H. Tian, X. Qian, L. Huang, Y. Geng, and D. Yan: Organic Electronics 12 (2011) 1358.

11) C. W. Tang: Appl. Phys. Lett. 48 (1986) 183.

12) P. E. Fielding and F. Gutman: J. Chem. Phys. 26 (1957)411

13) Y. Kuzumoto, H. Matsuyama, and M. Kitamura: to be published in Jpn. J. Appl. Phys.

14) U. Weiler, T. Mayer, W. Jaegermann, C. Kelting, D. Schlettwein, S. Makarov, and D. Wöhrle: J. Phys. Chem. B 108 (2004)19398.

15) W. Chen, H. Huang, S. Chen, Y. L. Huang, X. Y. Gao, and A. T. S. Wee: Chem. Mater. 20 (2008) 7017.

16) H. Peisert, M. Knupfer, and J. Fink: Appl. Phys. Lett. 81 (2002) 2400.

17) R. Murdey, N. Sato, and M. Bouret: Mol. Cryst. Liquid Cryst. 455 (2006) 211.

18)H. Peisert, M. Knupfer, T. Schwieger, G. G. Fuentes, D. Olligs, J. Fink, and Th. Schmidt: J. Appl. Phys. 93 (2003) 9683.

19) H. Peisert, M. Knupfer, and J. Fink: Surface Science 515 (2002) 491.

20) Z. Bao, A. J. Lovinger, and J. Brown: J. Am. Chem. Soc. 120 (1998) 207.

21) A. Optiz, B. Ecker, J. Wagner, A. Hinderhofer, F. Schreiber, J. Manara, J. Pflaum, and W. Brütting: Org. Elec. 10 (2009)1259.

22) H. Wang, J. Wang, H. Huang, X. Yan, and D. Yan: Org. Elec. 7 (2006) 369.

23) R. Ye, M. Baba, K. Suzuki, Y. Ohishi, and K. Mori: Jpn. J. Appl. Phys. 42 (2003) 4473.

24) S. J. Kang, M. Noh, D. S. Park, H. J. Kim, C. N. Whang, and C. -H. Chang: J. Appl. Phys. 95 (2004) 2293.

25) Y. -J. Lin, H. -Y. Tsao, and D. -S. Liu: Appl. Phys. Lett. 101 (2012) 013302.

26) H. J. C. Marrero, C. M. Alonso, L. H. Difur, and H. Hu: Eur. Phys. J. Appl. Phys. 63 (2013) 10201.

27) G. Scavia, W. Porzio, S. Destri, L. Barba, G. Arrighetti, S. Milita, L. Fumagalli, D. Natali, and M. Sampietro: Surface Science 620 (2008) 3106.

28) L. Lozzi, S. Santucci, S. L. Rosa, B. Delley, and S. Picozzi: J. Chem. Phys. 121 (2004) 1883.

29) O. Berger, W. -J. Fischer, B. Adolphi, S. Tierbach, V. Melev, and J. Schreiber: J. Mater. Sci.: Mater. Electron. 11 (2000) 331.

30) M. D. Pirriera, J. Puigdollers, C. Voz, M. Stella, J. Bertomeu, and R. Alcubilla: J. Phys. D: Appl. Phys. 42 (2009) 145102.

31) L. Grządziel, J. Żak, and J. Szuber: Thin Solid Films 436 (2003) 70.

32)T. Nonaka, Y. Nakagawa, Y. Mori, M. Hirai, T. Matsunobe, M. Nakamura, T. Takahagi, A. Ishitani, H. Lin, and K. Koumoto: Thin Solid Films 256 (1995) 262.

33) Z. Bao, A. J. Lovinger, and A. Dodabalapur: Adv. Mater. 9 (1997) 42.

34) W. Y. Tong, A. B. Djurišić, M. H. Xie, A. C. M. Ng, K. Y. Cheung, W. K. Chan, Y. H. Leung, H. W. Lin, and S. Gwo: J. Phys. Chem. B 110 (2006) 17406.

35) H. Yamamoto, H. Kasajima, W. Yokoyama, H. Sasabe, and C. Adachi: Appl. Phys. Lett. 86 (2005) 083502.

36) C. Shen and A. Kahn: J. Appl. Phys. 90 (2001) 4549.

37) C. -a. Di, G. Yu, Y. Liu, X. Xu, Y. Song, and D. Zhu: Appl. Phys. Lett. 89 (2006) 033502.

38) J. H. Park, S. W. Cho, S. H. Park, J. G. Jeong, H. J. Kim, Y. Yi, and M. -H. Cho: Synth. Met. 160 (2010) 108.

39) A. S. Komolov, E. F. Lazneva, S. A. Komolov, P. S. Repin, and A. A. Gavrikov: Semiconductors 46 (2012) 988.

40) C. Shen, A. Kahn, and J. Schwartz: J. Appl. Phys. 90 (2001) 6236.

Chapter 6

Work Function of Gold, Silver, and Copper Surfaces Modified using Substituted Benzenethiols

6.1 Introduction

Organic electronic devices including transistors,1,2) light-emitting diodes (LEDs) 3,4) and photovoltaic cells5,6) have attracted great attention because of their potential application to mechanically flexible, large area, and lost cost devices. The interface between an organic semiconductor layer and an electrode plays an important role in the device performance. Metal electrodes modified with polar molecules have been used to improve carrier injection into organic layers for organic transistors7-10) and organic LEDs.11,12) This is because modification of electrodes forms a monolayer on the electrode, and the layer leads to the work function change of the electrode.

Various aromatic and aliphatic thiols have been used to form a polar monolayer on a metal electrode, and to turn the work function of the metal surface. In pioneering works, alkylthiols with different chain lengths,13) and fluorinated and amino alkylthiols14) have been used to change the surface potential of metals. Aromatic thiols have also been used for modification of electrodes15) and improvement of carrier injection into organic layers.16) In particular, metal electrodes modified with substituted benzenethiols (BTs) have improved the device performance of organic transistors17-21) and organic LEDs.22) Substituted BTs, 4-nitrobenzenethiol,17,19) pentafluorobenzenethiol (PFBT),18,20,21) 4-fluorobenzenethiol (FBT),20,22) 4-methylbenzenethiol (MBT),19) 4-aminobenzenethiol (ABT),19) 4-(dimethylamino)benzenethiol (DABT).19) have contributed to improvement of device performance.

Formation and structure of Au, Ag, and Cu surfaces modified with BT,23-29) FBT,29,30) and PFBT29,31-33) have been intensively studied by electron energy loss spectroscopy, X-ray photoelectron spectroscopy, scanning tunneling microscopy, UV photoelectron spectroscopy, and infrared reflection. One of the most useful information for application to organic electronic devices is a systematical investigation including the work function and thermal stability of metal surfaces modified with various substituted BTs. Schmidt and co-workers have investigated the thermal stability of Cu surfaces modified with BT, PFBT, FBT, and ABT by thermal desorption spectroscopy.29) Thermal stability of BT on a Ag surface has been examined by Han and co-workers using infrared spectroscopy.26) Thermal desorption behavior of a BT monolayer formed on a Au surface has been reported by two groups.25,34)

In this chapter, we report the work function of Au, Ag, and Cu surfaces modified with various substituted BTs: PFBT, FBT, MBT, ABT, and DABT. Among the three metals, we especially focus on Au. The relation between measured work function and calculated dipole moment of the molecules are examined. In addition, the thermal stability of the modified Au electrode is discussed on the basis of the work function of annealed samples and the thermal desorption spectra.

6.2 Methodology

6.2.1 Brief theory

Schematic illustration of a Au, Ag, and Cu film, which were prepared in this study, modified with a substituted BT is shown in Fig. 6.1(a). In general, a polar monolayer formed on a metal surface induces potential energy shift. The energy shift can be observed as work function change of the modified metal. Dipoles with the direction shown in Fig. 6.1(b) decrease work function and dipoles with opposite direction increase work function. Work function change induced by a polar monolayer ΔW is expressed as

$$\Delta W = \frac{qNd\cos\theta}{\varepsilon}, \tag{6.1}$$

where q is the elementary charge, N is the area density of the molecule, d is the dipole moment of the molecule, θ is the average angle of the dipole direction relative to the surface normal, and ε is the permittivity of the molecule layer.14,35,36) The dipole moment d includes influence of charge distribution at the interface between the metal and the monolayer.

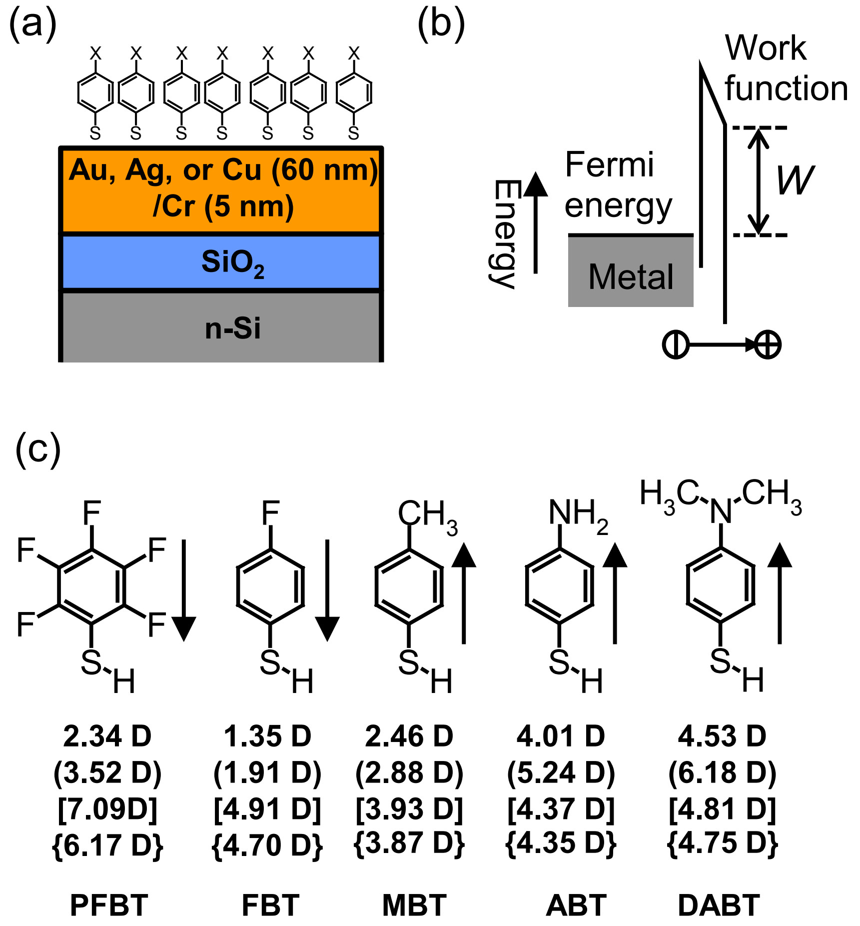

Fig. 6.1. (a) Schematic illustration of a Au, Ag, and Cu surface modified with a substituted benzenthiol evaluated in this study. (b) The energy level of a Au, Ag, and Cu modified with a polar monolayer. (c) Chemical structures and dipole moments $d_{\mathrm{S\text{-}H}}$ of molecules used for modification of a Au, Ag, and Cu surface. Numerical value in the parentheses, square brackets, and braces represents a dipole moment $d_{\mathrm{S\text{-}Au}}$, $d_{\mathrm{S\text{-}Ag}}$, and $d_{\mathrm{S\text{-}Cu}}$ calculated for a substituted benzene molecule with a S-Au, S-Ag, and S-Cu group instead of a S-H group, respectively.

6.2.2 Calculations

The chemical structure of molecules used for surface modification is shown in Fig. 6.1(c). We calculated the dipole moment of the molecule on density functional theory (DFT) using the Gaussian 09 program package with the B3LYP method and LanL2DZ basis set.[37)] Also, we calculated the dipole moment of a molecule with a S-Au, S-Ag, and S-Cu group instead of a

S-H group in a substituted BT to roughly involve the influence of S-Au, S-Ag, and S-Cu termination in a monolayer on the dipole moment, respectively. Calculated dipole moments $d_{\text{S-H}}$ are shown in Fig. 6.1(c) with the chemical structure. The direction of dipoles in PFBT, FBT, MBT, ABT, and DABT is inclined at an angle of 31, 60, 24, 14, and 12° with respect to the molecular axis, respectively. Numerical value in the parentheses, square brackets, and braces represents dipole moment $d_{\text{S-Au}}$, $d_{\text{S-Ag}}$, and $d_{\text{S-Cu}}$ calculated for a substituted benzene molecule with a S-Au, S-Ag, and S-Cu group, respectively. The dipole moment is represented in debye units and denoted by D.

6.2.3 Experiments

The 60-nm-thick Au, Ag, and Cu layer for this study was thermally evaporated on a SiO_2/Si substrate with a 5-nm-thick Cr adhesive layer at room temperature, respectively. The substrate with the deposited metal layer was stored in a dry-nitrogen filled glovebox until surface modification. The substrate was immersed in an ethanol solution with substituted BT for surface modification. The concentration C of the substituted BT ranged from 1 μ to 10 m mol/L and the immersion time t ranged from 1 to 100 min. The surface modification was performed in air at room temperature of about 300 K. Some substrates with Au layer were annealed on a hot plate placed in the glovebox at temperatures of 373 to 473 K to investigate the thermal stability. The work function of Au, Ag, and Cu surfaces was measured with an atmospheric photoelectron spectrometer (AC-2, Riken Keiki Co.). Also, thermal desorption spectra during linearly heating at a rate of 30 K/min were measured with a gas chromatograph mass spectrometer (GCMS-QP2010 Ultra, Shimazu Co.) to observe species desorbing from a modified Au surface.

6.3 Results

6.3.1 Au surfaces modified with substituted benzenethiols

Figure 6.2 shows the measured work function of Au surface modified with PFBT and MBT as a function of a product of immersion time and concentration tC. The work function for PFBT increases with tC and that for MBT decreases with tC. For both modifications, the work function almost saturates at tC greater than 10^{-3} min mol/L. The saturated work function W_{sat} is about 5.48 eV for PFBT, and 4.47 eV for MBT. On the other hand, unmodified Au surface as a reference had a work function of 4.83 eV, which is denoted as W_0. Since work function change is proportional to the area density of molecules on a metal surface as represented in (6.1), work function change ΔW is written as

$$\Delta W = \Delta W_{\text{sat}}\left(1 - \exp(-k_a tC)\right), \qquad (6.2)$$

where ΔW_{sat} is a reached value of ΔW, and equals $W_{\text{sat}} - W_0$ and k_a is the association constant for the adsorption of the molecules.[38)] Here, it is assumed that the adsorption conforms to the Langmuir adsorption model, and desorption can be neglected. Curves fitting to the measured work function using (6.2) are shown in Fig. 6.2. Association constant is estimated to be 106 s^{-1} mol^{-1} L for PFBT and 386 s^{-1} mol^{-1} L for MBT from the fitting curves.

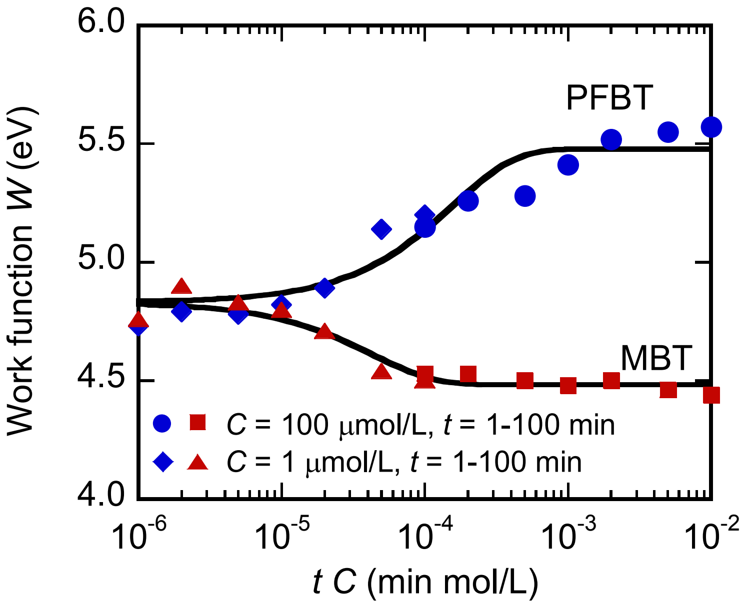

Fig. 6.2. Work function of PFBT- and MBT- modified Au surfaces treated with different tC, where t is the immersion time and C is the concentration of PFBT or MBT in the solution.

Figure 6.3 shows the saturated work function of Au surface modified with PFBT, FBT, MBT, ABT, and DABT. The horizontal axis represents the dipole moment $d_{\text{S-Au}}$ in the substituted benzene with a S-Au group obtained by DFT calculation. The saturated work function is average for five to ten samples prepared at $tC \geq 10^{-3}$ min mol/L. The length of the error bars is of twice the standard deviation for the samples. The experimental W_{sat} value decreases with the dipole moment except that for ABT. The tendency of the work function change is consistent with (6.1). However, the work function does not linearly change with the dipole moment even excluding that for ABT. The dependence of the work function indicates that the area density N and/or the average angle θ in (6.1) depend on the substituted BTs. We estimated the area density from W_{sat} and $d_{\mathrm{S\text{-}Au}}$ assuming $\theta = 0$ and $\varepsilon = 3.0$.[29,31] Since θ is generally greater than 0, the assumption provides underestimation of area density. The estimated area density is summarized with $d_{\mathrm{S\text{-}H}}$, $d_{\mathrm{S\text{-}Au}}$ and W_{sat} in Table 6.1. The area density ranges from 0.23 to 1.6 × 10^{14} cm^{-2}, and are not excessive values. The value of 2.3 × 10^{13} cm^{-2} for ABT is slightly less than those for other substituted BTs. Adsorption of ABT on a Au surface may be abnormal because of the reactivity of the amino group. Since amines act as nucleophiles, amino terminals sometimes lead to unintentional reaction. In actual, dense amine-terminated monolayers has been prepared by hidden amine route.[39]

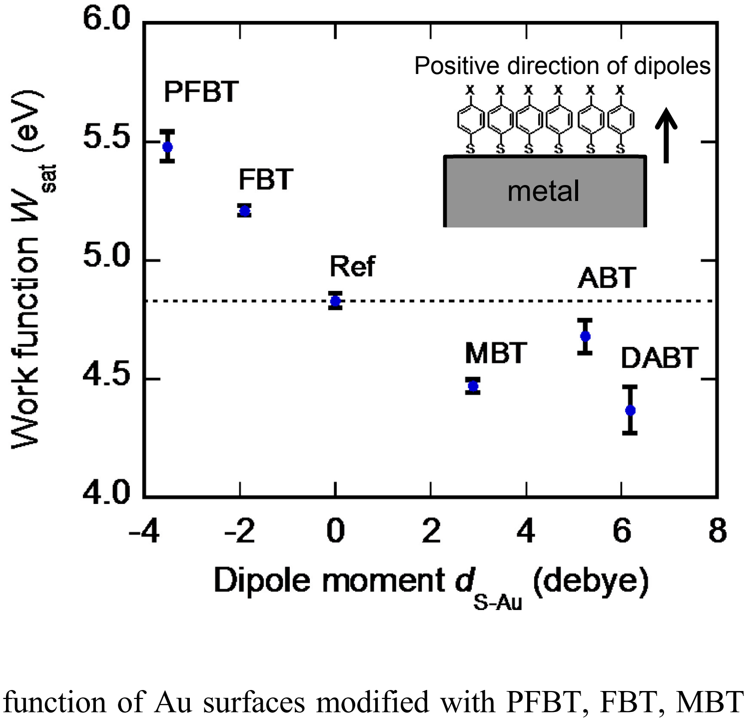

Fig. 6.3. Work function of Au surfaces modified with PFBT, FBT, MBT, ABT, and DABT prepared under saturation condition, and unmodified Au surface.

Table 6.1. Work function of Au surface modified various substituted benzenethiols W_{sat}, calculated dipole moments of substituted benzenethiols $d_{\mathrm{S\text{-}H}}$, and substituted benzene with a S-Au group $d_{\mathrm{S\text{-}Au}}$, and estimated area density of molecules formed on Au surface.

molecules	W_{sat} (eV)	$d_{\mathrm{S\text{-}H}}$ (debye)	$d_{\mathrm{S\text{-}Au}}$ (debye)	N (cm^{-2})
PFBT	5.48	−2.34	−3.52	1.5×10^{14}
FBT	5.21	−1.35	−1.91	1.6×10^{14}
MBT	4.47	2.46	2.88	1.0×10^{14}
ABT	4.68	4.01	5.24	2.3×10^{13}
DABT	4.37	4.53	6.18	5.9×10^{13}

6.3.2 Ag and Cu surfaces modified with substituted benzenethiols

The experimental W_{sat} value of Ag and Cu surface modified with PFBT, FBT, MBT, ABT, and DABT decreases with the dipole moment, and the tendency of the work function change is consistent with (6.1), except that for DABT on Ag surface and for ABT. Although the dipole moment of $d_{S\text{-}Ag}$ and $d_{S\text{-}Cu}$ in ABT are larger than in MBT, the differences of the work function of Ag and Cu surface between ABT-modified and unmodified substrate are both less than 0.15 eV. As mentioned for Au in Sect. 6.3.1, adsorption of ABT on Ag and Cu surface may also be abnormal as in the case of Au because of the reactivity of the amino group. Figure 6.4 shows the saturated work function of Ag and Cu surface modified with PFBT, FBT, MBT, and DABT, and the work function of unmodified Ag and Cu surface. We estimated the area density from W_{sat} and $d_{\mathrm{S\text{-}Ag}}$ or $d_{\mathrm{S\text{-}Cu}}$ according to (6.1) assuming $\theta = 0$ and $\varepsilon = 3.0$.[29,31)] The estimated area density is summarized in Table 6.2. The area density of PFBT, FBT, and MBT ranges from 0.97 to 1.2 × 10^{14} cm^{-2} for Ag and 0.26 to 0.64 × 10^{14} cm^{-2} for Cu. Also, the area density of each thiol on Ag and Cu except that for DABT is basically in order of on Au > Ag > Cu surface though that for MBT on Au is comparable on Ag. In case for PFBT, the area density is 1.5 for Au, 0.97 for Ag, and 0.32 × 10^{14} cm^{-2} for Cu surface, respectively. This tendency is probably due to thin oxide layer on Ag and Cu surface. Since the oxide layer surface obstructs the bond formation between Ag or Cu and sulfur atom in thiol, the area density of thiol on a metal surface with oxide is small in comparison with a metal surface without oxide. Also, it is commonly known that oxide on Au is not formed. Therefore, the area density on Ag or Cu is smaller than on Au. Furthermore, since the oxidation reactivity of Cu is higher than Ag, oxide formed on Cu tends to be denser than on Ag. Therefore, the area density of thiol on Cu is possibly smaller than on Ag. In this work, oxide is probably formed by reacting metal with oxygen in air or water in ethanol solvent. To investigate the effect of thiol formation without the influence of oxide on Ag or Cu surface, the experiment using anhydrous solvent under an inert atmosphere is needed Contrary to other thiols, the area density for DABT is in order of Au < Ag < Cu. Although this reason is unclear, it may be related to an unshared electron pair in dimethyl amino group in DABT.

The work function of Ag and Cu surface in reference sample was 4.74 and 5.07 eV, which is high as compared with the normal work function of Ag and Cu. This is also probably due to the oxide layer on Ag or Cu surface. The change in the work function implies the presence of a dipole moment at the interface between a Ag or Cu layer and a thiol layer. We calculated the dipole moment of a Ag-O and a Cu-O model structures by quantum chemical calculation. These structures were optimized using B3LYP/LanL2DZ method. The calculation results showed that the dipole moment in Ag-O and Cu-O are 4.84 and 4.65 debye, respectively. The direction of both dipoles, which is from oxygen to Ag or Cu, increases the work function of metal. This result supports the presence of an oxide layer and a dipole moment induced by the oxide layer at the interface between a Ag or Cu layer and a thiol layer.

Table 6.2. Work function of Ag and Cu surface modified various substituted benzenethiols W_{sat}, calculated dipole moments of substituted benzene with a S-Ag group $d_{S\text{-}Ag}$ and a S-Cu group $d_{S\text{-}Cu}$, and estimated area density of molecules formed on Ag and Cu surface.

	Ag			Cu		
molecules	W_{sat} (eV)	$d_{S\text{-}Ag}$ (debye)	N (cm^{-2})	W_{sat} (eV)	$d_{S\text{-}Cu}$ (debye)	N (cm^{-2})
PFBT	5.61	−7.09	9.7×10^{13}	5.32	−6.17	3.2×10^{13}
FBT	5.36	−4.91	1.0×10^{14}	5.22	−4.70	2.6×10^{13}
MBT	4.15	3.93	1.2×10^{14}	4.75	3.87	6.4×10^{13}
DABT	4.34	4.81	6.5×10^{13}	4.24	4.75	1.5×10^{14}

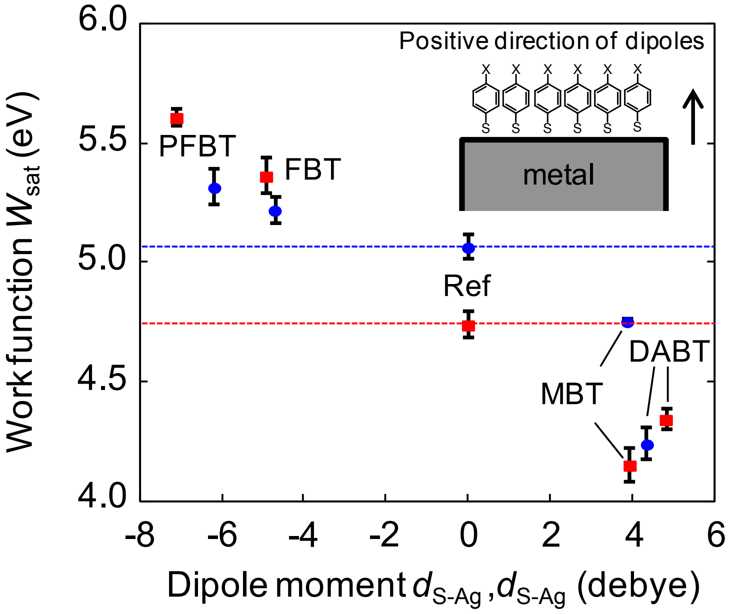

Fig. 6.4. Work function of Ag (red square) and Cu (blue circle) surfaces modified with PFBT, FBT, MBT, and DABT prepared under saturation condition, and unmodified Ag and Cu surface. The horizontal axis represents the dipole moment $d_{S\text{-}Ag}$ and $d_{S\text{-}Cu}$ in the substituted benzene with a S-Ag and S-Cu group obtained by DFT calculation, respectively. The saturated work function is average for four to eleven samples prepared at $tC \geq 10^{-3}$ min mol/L. The length of the error bars is of twice the standard deviation for the samples.

6.3.3 Thermal stability of modified Au surface

The thermal stability of a monolayer formed on a metal should be considered when the modified metal is applied for organic electronic devices. Thus, we investigated the work function of modified Au surface with which a substrate was annealed at temperatures T_a of 373 to 473 K for 10 min. Figure 6.5(a) shows the measured work function of annealed samples W_T. The work function for unmodified Au surface is also shown as a reference, and is close to 4.83 eV. The work functions for PFBT and FBT decrease to 4.83 eV with T_a. The W values at T_a = 373 K are close to those for the un-annealed substrates, respectively. On the other hand, the work functions for MBT and DABT gradually increase to 4.83 eV with T_a. Since work function change ΔW is proportional to area density of molecules N, the decrease and increase indicate desorption of substituted benzenethiolates from a Au surface. In addition, the work function seems to decrease and increase in accordance with a rule. On the other hand, the work function for ABT randomly closes to 4.83 eV with T_a. The behavior may be related to the low estimated area density for ABT in Table 6.1.

To estimate the activation energy of desorption, we represent work function W_T as $-\ln(\Delta W_T/\Delta W_{\mathrm{sat}})$ in Fig. 6.5(b), where $\Delta W_T = W_T - W_0$. Approximately, $-\ln(\Delta W_T/\Delta W_{\max})$ decrease exponentially with $1000/T$ except that for ABT. When desorption of species from a surface is a first-order process, the desorption rate k_d can be given by

$$k_d = \nu \exp\left(-E_a / k_B T\right), \tag{6.3}$$

where ν is the attempt frequency and k_B is the Boltzmann constant.[35)] Using (6.1) and (6.3), work function is expressed as

$$\ln\left(\Delta W_T / \Delta W_{\mathrm{sat}}\right) = -\nu \exp\left(-E_a / k_B T\right) t\,. \tag{6.4}$$

The relation of (6.4) and experimental result in Fig. 6.5(b) determine activation energy E_a. The estimated activation energy for PFBT, FBT, MBT, and DABT is 73.3, 43.3, 41.0, and 41.8 kJ/mol, respectively. The E_a values for FBT, MBT, and DABT are close to one another. On the other hand, the activation energy of 73.3 kJ/mol for PFBT is slightly greater than those for FBT, MBT, and DABT. The larger activation energy for PFBT is attributed to fluorine atoms in the PFBT. In particular, a fluorine atom in the ortho position of the benzene ring probably contributes to the increase in activation energy. Jiang et al. have demonstrated that ortho-fluorobezenethiolate on a gold surface is more stable than para-fluorobenzenethiolate by quantum chemical calculation.[30)] Some groups have estimated the activation energy for desorption of specimens from thiolate monoleyers on gold surfaces. The activation energy was 50 kJ/mol for methanethiol,[40)] 66 kJ/mol for alkanethiol,[41)] and 113 kJ/mol for BT.[25)] The values reported in this study are not far from these values.

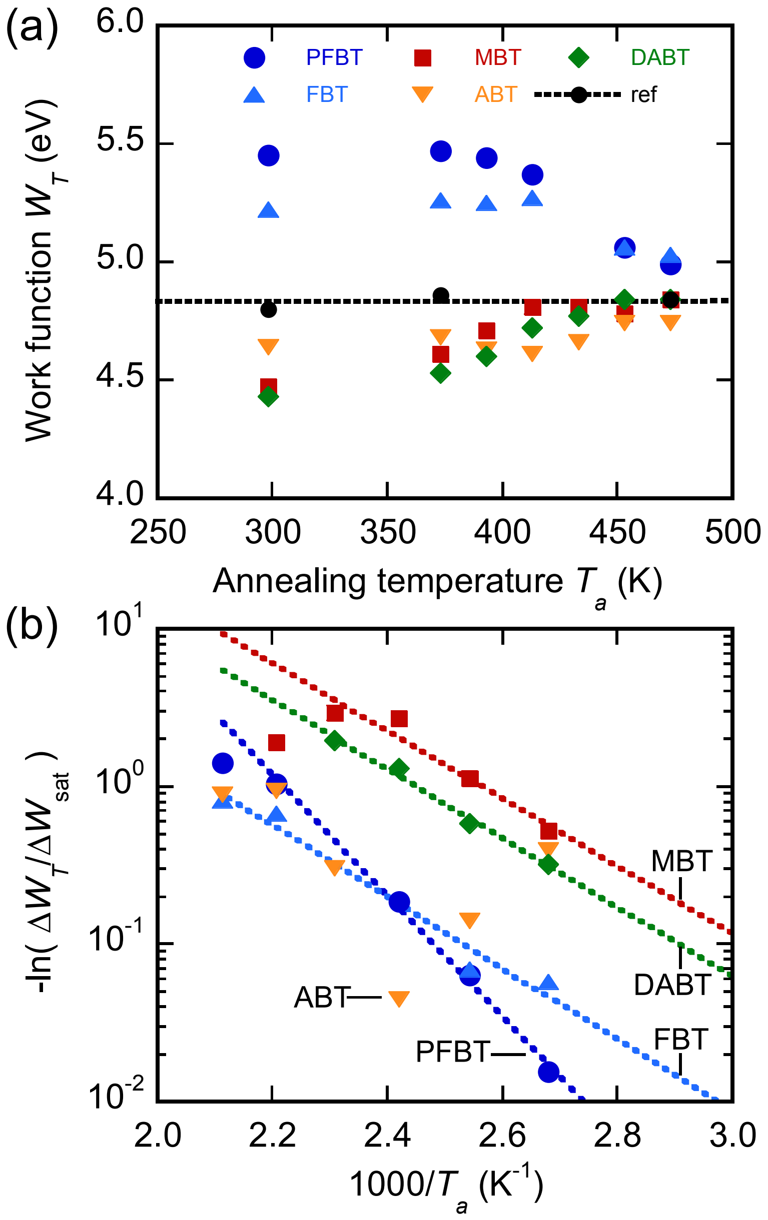

Fig. 6.5. (a) Work function of samples annealed at different temperatures for 10 min, W_T. (b) Arrhenius plots of $-\ln(\Delta W_T/\Delta W_{\mathrm{sat}})$, where $\Delta W_T = W_T - W_0$, $\Delta W_{\mathrm{sat}} = W_{\mathrm{sat}} - W_0$, W_{sat} is the saturated work function of an un-annealed sample and W_0 is the work function of unmodified Au surface.

Thermal desorption spectra were also measured with a gas chromatograph mass spectrometer to investigate species desorbing from modified Au surfaces. Figure 6.6 shows the measured thermal desorption spectra for samples prepared with t = 10 min and C = 1 mmol/L. Molecular formula expected from mass fragment is also shown in the figure. For all substituted BTs, the lower and the higher mass fragments correspond to sulfur-free and sulfur-containing species. The spectrum of the sulfur-containing species indicates the cleavage of the S-Au bond in the monolayer formed on the Au surface. Since ionization for quadrupole mass analysis induces disassociation of sulfur atoms from sulfur-containing species and produces sulfur-free species, a certain amount of signal for the sulfur-free species is attributed to the sulfur-containing species. For substituted thiols, signals for species produced by ionization are less than that of an original species. 42) In addition, the spectrum for the sulfur-free species has different shape from that for the sulfur-containing species. Therefore, the spectrum for the sulfur-free species in Fig. 6.6 indicates the cleavage of the C-S bond in the monolayer formed on the Au surface. Figure 6.6(f) shows illustration of sulfur-free and sulfur-containing species desorbing from the Au surface.

Some spectra shown in Figs. 6.6(a)-(e) have mainly two intense peaks, which suggest the presence of different adsorption sites on the Au surface.29,34) Here, we focus on the intense peak for the sulfur-free species at low temperature because of the higher intensity as compared to that for the sulfur-containing molecule. The intense peaks for FBT, MBT, and DABT are observed around 410 K. The temperature is slightly lower than 438 K for PFBT. The comparison indicates that the C-S bond in PFBT-molecule layer is more stable as compared to those for FBT, MBT and DABT. The indication is consistent with the comparison of activation energy estimated from work function change of annealed samples. The temperature of 410 and 438 K are close to that of 427 K for a BT-monolayer on a Au(111) surface.25) On the other hand, PFBT- and FBT-monolayers formed on Cu surfaces had an intense peak of about 370 K. 29) That result implies that a monolayer on a Au surface is more stable than that on a Cu surface.

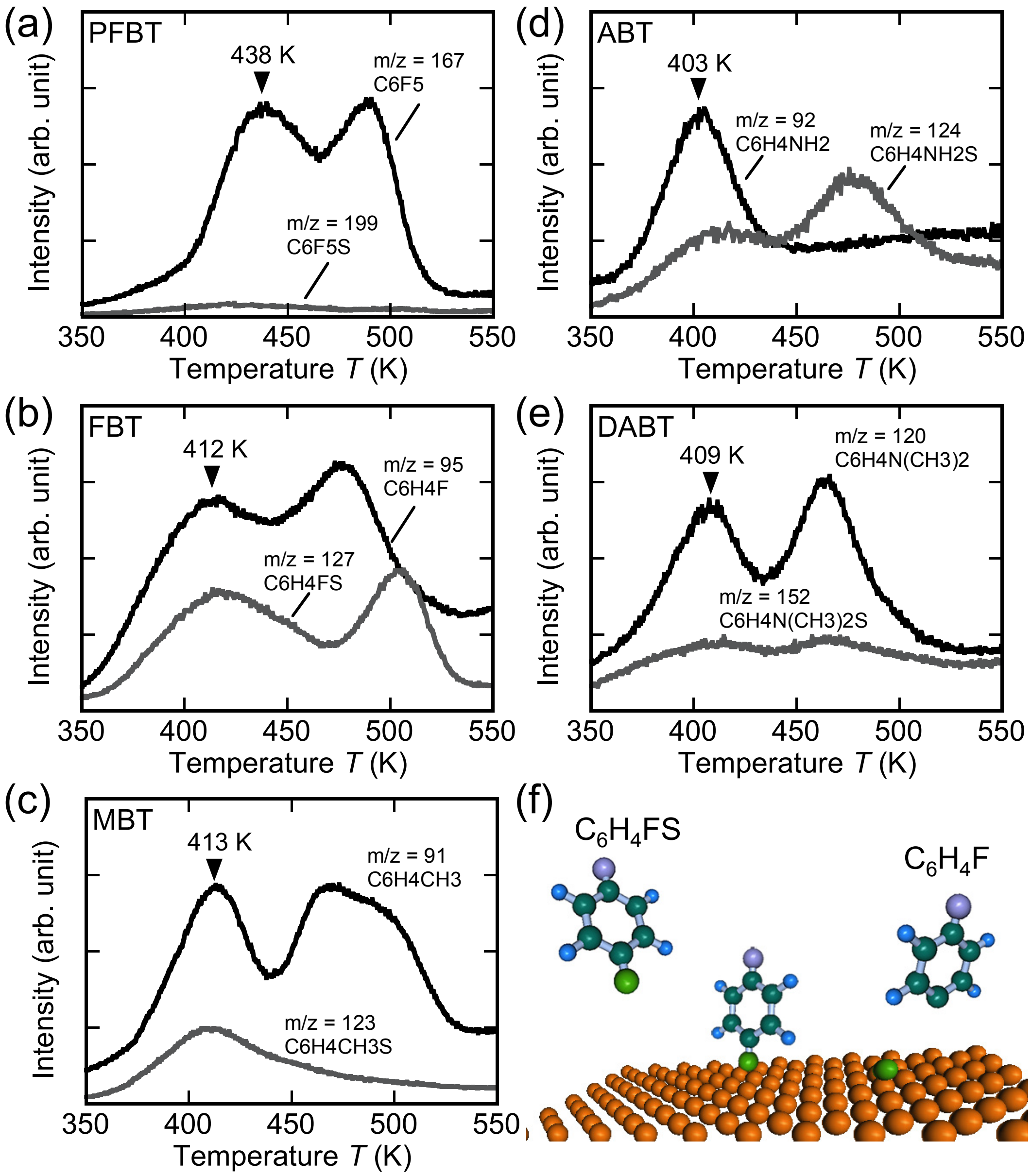

Fig. 6.6. Thermal desorption spectra measured for Au surfaces modified with (a) PFBT, (b) FBT, (c) MBT, (d) ABT, and (e) DABT. (f) Schematic illustration of sulfur-containing and sulfur-free molecules desorbing from a Au surface modified with FBT.

6.4 Conclusions

We demonstrated systematic investigation of work function for Au, Ag, and Cu surfaces modified with substituted benzenethiols: PFBT, FBT, MBT, ABT, and DABT. The Au work function for PFBT and MBT changed with product of reaction time and concentration on the basis of the Langmuir adsorption model. The Au surface modified with PFBT, FBT, MBT, ABT, and DABT had a work function in the range of 4.37 to 5.48 eV. The Ag and Cu surface modified with PFBT, FBT, MBT, and DABT had a work function in the range of 4.15 to 5.61 and 4.24 to 5.32 eV, respectively. The work function change depending on substituted benzenethiols is available for band alignment between metal electrodes and organic layers in organic devices. The thermal stability of modified Au surfaces was also investigated on the change of work function and thermal desorption spectra. Thermal annealing above 373 K of the substrate with the modified Au layer changed the work function to that of unmodified Au surface. Thermal desorption spectroscopy revealed presence of molecules desorbing from modified Au surfaces, indicating the cleavage of the C-S bond as well as the S-Au bond. We need to note the thermal stability when we use Au electrodes modified with substituted benzenethiols for organic devices for which substrate heating is required. The result for the thermal stability is useful for process design of organic electronic devices.

6.5 References

1) T. Sekitani and T. Someya: Jpn. J. Appl. Phys. **51** (2012) 100001.
2) M. Kitamura and Y. Arakawa: J. Phys.: Condens. Matter **20** (2008) 184011.
3) T. Tsutsui and N. Takada: Jpn. J. Appl. Phys. **52** (2013) 110001.
4) J. Shinar and R. Shinar: J. Phys. D: Appl. Phys. **41** (2008) 133001.
5) T. Ameri, G. Dennler, C. Lungenschmied and C. J. Brabec: Energy & Environmental Science **2** (2009) 347.
6) C. J. Brabec: Sol. Energy Mater. Sol. Cells **83** (2004) 273.
7) S. H. Kim, J. H. Lee, S. C. Lim, Y. S. Yang, T. Zyung: Jpn. J. Appl. Phys. **43** (2004) L60.
8) B. H. Hamadani, D. A. Corley, J. W. Ciszek, J. M. Tour, and D. Natelson: Nano Lett. **6** (2006) 1303.
9) X. Cheng, Y.-Y. Noh, J. Wang, M. Tello, J. Frisch, R.-P. Blum, A. Vollmer, J. P. Rabe, N. Koch, and H. Sirringhaus: Adv. Funct. Mater. **19** (2009) 2407.
10) P. Marmont, N. Battaglini, P. Lang, G. Horowitz, J. Hwang, A. Kahn, C. Amato, and P. Calas: Org. Electron. **9** (2008) 419.
11) B. de Boer, A. Hadipour, M. M. Mandoc, T. van Woudenbergh, and P. W. M. Blom: Adv. Mater. **17** (2005) 621.
12) L. Zhu, H. Tang, Y. Harima, K. Yamashita, D. Hirayama, Y. Aso, and T. Otsubo: Chem. Commun. **18** (2001) 1830.
13) S. D. Evans and A. Ulman: Chem. Phys. Lett. **170** (1990) 462.
14) I. H. Campbell, S. Rubin, T. A. Zawodzinski, J. D. Kress, R. L. Martin, and D. L. Smith: Phys. Rev. B **54** (1996) 14321.
15) E. Sabatani, J. Cohen-Boulakia, M. Bruening, and I. Rubinstein, Langmuir **9** (1993) 2974.
16) I. H. Campbell, J. D. Kress, R. L. Martin, D. L. Smith, N. N. Barashkov and J. P. Ferraris: Appl. Phys. Lett. **71** (1997) 3528.
17) D. J. Gundlach, L. Jia, and T. N. Jackson: IEEE Electron Device Lett. **22** (2001) 571.
18) S. K. Park , T. N. Jackson, J. E. Anthony, D. A. Mourey: Appl. Phys. Lett. **91** (2007) 063514.
19) M. Kitamura, Y. Kuzumoto, S. Aomori, M. Kamura, J. H. Na, and Y. Arakawa: Appl. Phys. Lett. **94** (2009) 083310.
20) J.-P. Hong, A.-Y. Park, S. Lee, J. Kang, N. Shin, and D. Y. Yoon: Appl. Phys. Lett. **92**

(2008) 143311.

21) M. Kitamura, Y. Kuzumoto, W. Kang, S. Aomori, and Y. Arakawa: Appl. Phys. Lett. **97** (2010) 033306.

22) L.-W. Chong, Y.-L. Lee, T.-C. Wen, and T.-F. Guo: Appl. Phys. Lett. **89** (2006) 233513.

23) C. M. Whelan, M. R. Smyth, and C. J. Barnes: Langmuir **15** (1999) 116.

24) B. S. Kim, J. M. Beebe, Y. Jun, X.-Y. Zhu, and C. D. Frisbie: J. Am. Chem. Soc. **128** (2006) 4970.

25) D. Käfer, A. Bashir, and G. Witte: J. Phys. Chem. C **111** (2007) 10546.

26) S. W. Han, S. J. Lee, and K. Kim: Langmuir **17** (2001) 6981.

27) S. Frey, V. Stadler, K. Heister, W. Eck, M. Zharnikov, M. Grunze, B. Zeysing, and A. Terfort: Langmuir **17** (2001) 2408.

28) Y. Kitaguchi, S. Habuka, T. Mitsui, H. Okuyama, S. Hatta, and T. Aruga: J. Chem. Phys. **139** (2013) 044708.

29) C. Schmidt, A. Witt, and G. Witte: J. Phys. Chem. A **115** (2011) 7234.

30) P. Jiang, K. Deng, D. Fichou, S.-S. Xie, A. Nion, and C. Wang: Langmuir **25** (2009) 5012.

31) Z. Jia, V. W. Lee, and I. Kymissis: Phys. Rev. B **82** (2010) 125457.

32) H. Kang, N.-S. Lee, E. Ito, M. Hara, and J. Noh: Langmuir **26** (2010) 2983.

33) W. Azzam, A. Bashir, P. U. Biedermann, and M. Rohwerder: Langmuir **28** (2012) 10192.

34) J. Noh, E. Ito, and H. Hara: J. Colloid Interface Sci. **342** (2010) 513.

35) H. Lüth: *Solid Surfaces, Interfaces and Thin Films* (Springer-Verlag Berlin Heidelberg, Germany, 2001) 4th ed., Chap. 10.

36) N. Gozlan, U. Tisch, and H. Haick: J. Phys. Chem. C **112** (2008) 12988.

37) M. J. Frisch, et al.: Gaussian 09, Revision B.01, Gaussian, Inc., Wallingford CT, 2010.

38) D. S. Karpovich and G. J. Blanchard: Langmuir **10** (1994) 3315.

39) Y. Ofir, N. Zenou, I. Goykhman, and S. Yitzchaik: J. Phys. Chem. B **110** (2006) 8002.

40) R. G. Nuzzo, B. R. Zegarski, and L. H. Dubois: J. Am. Chem. Soc. **109** (1987) 733.

41) G. Baralia, A. Duwez, B. Nysten, and A. Jonas: Langmuir **21** (2005) 6825.

42) F. G. Kitson, B. S. Larsen, and C. N. McEwen: *Gas Chromatography and Mass Spectrometry* (Academic Press, Orlando, 1996) Chap. 33.

Chapter 7

Conclusions

In this thesis, the potential of halogenated CuPc for OPV application has been investigated. The development of stable organic material has been desired for the practical use of OPV cell. Halogenated phthalocyanines are promising material for OPV use because some halogenated phthalocyanines are known as stable n-type organic semiconductor. Therefore, detail investigation about halogenated phthalocyanines and devices with a halogenated phthalocyanine contributes to the development of OPVs. In this thesis, we investigated the structural, electrical, and electronic properties of halogenated CuPc quantum chemically and experimentally. Also, the interface between organic semiconductor and metal electrode plays an important role in the organic device performance. The modification of metal electrode is useful to improve the carrier injection from an organic layer to an electrode in OPV device. One of the key factors is the work function of an electrode. Therefore, in this thesis, we also investigated the shift of work function of electrode by thiol modification of metal surface.

The conclusions in this thesis are described as follows.

In chapter 1, the HOMO and LUMO energy levels of fully halogenated CuPc (F_{16}CuPc, Cl_{16}CuPc, and Br_{16}CuPc) were quantum chemically calculated. The lowest HOMO and LUMO energies are obtained in F_{16}CuPc. This result shows that the fluorination is the most effective to tune the energy level over a wide range in halogenation.

In chapter 3, the electronic and vibrational structures of F_xCuPc (x= 0, 4, 8, 12, and 16) were investigated by density functional theory with B3LYP/LanL2DZ level. The HOMO and LUMO energies systematically depend on the number of fluorine atoms and their position on the benzene ring. The calculated HOMO (LUMO) energies vary in the range of −5.33 to −6.82 eV (−3.12 to −4.65 eV). The calculated bandgap energies and HOMO levels are consistent with experimental results.

In chapter 4, the electronic structures of F_xCuPc (x= 0, 8, and 16) dimer were examined by quantum chemical calculation. For each F_xCuPc (x= 0, 8, and 16) dimer aligned the π-conjugated plane of one molecule parallel to the other, it is found that the parallel displacement of one molecule along the line from copper to inner nitrogen of the other molecule or the line from copper to outer nitrogen of it substantially leads to low energy position. The experimental absorption spectra difference between α- and β-CuPc thin films was explained by intermolecular interaction. Assuming that the transformation from α-F_8CuPc to β-F_8CuPc take place in F_8CuPc thin film, it is inferred from the calculation results that similar spectra changes as in the case of CuPc is observed.

In chapter 5, the morphology and current-voltage characteristics of organic films with CuPc, F_8CuPc, and F_{16}CuPc prepared under different conditions were investigated. It is found that substrate heating improves the current-voltage characteristics of CuPc single layer devices and that the substrate heating from room temperature suppresses breakdown at low voltages in F_8CuPc and F_{16}CuPc devices. In addition, post-annealing effect under pressure on current-voltage characteristics of CuPc/F_{16}CuPc devices was investigated. For a CuPc/F_{16}CuPc device post-annealed at 300˚C under pressure, the rectifying property was drastically improved and the device worked as a photovoltaic cell.

In chapter 6, the work function of Au, Ag, and Cu surfaces modified with various substituted benzenethiols was systematically investigated. The work function varies in the range of 4.37 to 5.48, 4.15 to 5.61, and 4.24 to 5.32 eV for Au, Ag, and Cu surfaces depending on the substituted benzenethiol, respectively. The dependence of Au work function on concentration of substituted benzenethiol solution and on reaction time is explained by Langmuir absorption equation. Thermal annealing above 373 K of modified Au films influences the work function to that of unmodified Au surface. Thermal desorption spectroscopy revealed molecules desorbing from modified Au surfaces, indicating the cleavage of the C-S bond as well as the S-Au bond.

In conclusion, halogenation of CuPc is effective to fine energy level tuning. Therefore, halogenated CuPc is useful for band engineering in an organic device toward realizing high-efficiency OPV cell. Also, the rectifying property of a device with fluorinated CuPc is drastically improved by post-annealing under pressure. Further investigation for the influence of annealing under pressure may lead to further improvement of performance of the device with fluorinated CuPc layer. Also, the wide-range variation of the work function of Au, Ag, and Cu electrode by modification by substituted benzenethiols is useful to improve charge carrier injection between organic layer and electrode. The results about the thermal stability of

Au films modified by substituted benzenethiols and the work function dependence on the concentration and the reaction time is useful for process design of OPVs. The results in this thesis are helpful in developing high-efficiency OPV cell with halogenated CuPc molecule. Furthermore, the energy level tuning by halogenations may be applicable for other organic semiconductor materials. Also, post annealing under pressure is possibly useful to improve electric characteristics for other organic semiconductor films having rough surface. Work function tuning by substituted benzenthiols is also adaptable for other metal electrode. Therefore, the results in this thesis are of use for developing OPV cell with various organic semiconductor materials and electrodes.

List of Publications

Scientific Journals Related to This Work

1. Yasutaka Kuzumoto and Masatoshi Kitamura, "**Work Function of Gold Surfaces Modified using Substituted Benzenethiols: Reaction Time Dependence and Thermal Stability**", Applied Physics Express (submitted).

2. Yasutaka Kuzumoto, Hirotaka Matsuyama, and Masatoshi Kitamura, "**Structural and Electrical Properties of Fluorinated Copper Phthalocyanine toward Organic Photovoltaics: Post-Annealing Effect under Pressure**", Japanese Journal of Applied Physics (to be published).

3. Yasutaka Kuzumoto, Hirotaka Matsuyama, and Masatoshi Kitamura, "**Partially Fluorinated Copper Phthalocyanine toward Band Engineering for High-Efficiency OrganicPphotovoltaics**", Japanese Journal of Applied Physics **53**, 01AB03 (2014).

Scientific Journals Related to Other Work

1. Masatoshi Kitamura, Yasutaka Kuzumoto, and Yasuhiko Arakawa, "**Short-Channel, High-Mobility Organic Thin-Film Transistors with Alkylated Dinaphthothieno-thiophene**", physica status solidi (c) **10**, pp.1632-1635 (2013).

2. Masatoshi Kitamura, Yasutaka Kuzumoto, Shigeru Aomori, and Yasuhiko Arakawa, "**High-Frequency Organic Complementary Ring Oscillator Operating up to 200 kHz**", Applied Physics Express **4**, 051601 (2011).

3. Masatoshi Kitamura, Yasutaka Kuzumoto, Woogun Kang, Shigeru Aomori, and Yasuhiko Arakawa, "**High Conductance Bottom-Contact Pentacene Thin-Film Transistors with Gold-Nickel Adhesion Layers**", Applied Physics Letters **97**, 033306 (2010).

4. Masakazu Kamura, Yasutaka Kuzumoto, Shigeru Aomori, Hirohiko Houjou, Masatoshi Kitamura, and Yasuhiko Arakawa, "**Synthesis and Investigation of π-Conjugated Azomethine Self-Assembled Multilayers by Layer-by-Layer Growth**", Thin Solid Films **518**, pp.5115-5120 (2010).

5. Masatoshi Kitamura, Yasutaka Kuzumoto, Shigeru Aomori, Masakazu Kamura, Jong Ho Na, and Yasuhiko Arakawa, "**Threshold Voltage Control of Bottom-Contact n-Channel Organic Thin-Film Transistors using Modified Drain/Source Electrodes**", Applied Physics Letters **94**, 083310 (2009).

6. Masatoshi Kitamura, Yasutaka Kuzumoto, Masakazu Kamura, Shigeru Aomori, Jong Ho Na, and Yasuhiko Arakawa, "**Low-Voltage-Operating Fullerene C_{60} Thin-Film Transistors with Various Surface Treatments**", physica status solidi (c) 5, pp.3181-3183 (2008).

7. Masatoshi Kitamura, Yasutaka Kuzumoto, Masakazu Kamura, Shigeru Aomori, and Yasuhiko Arakawa, "**High-Performance Fullerene C_{60} Thin-Film Transistors Operating at Low Voltages**", Applied Physics Letters **91**, 183514 (2007).

International Conference Related to This Work

1. Yasutaka Kuzumoto, Hirotaka Matsuyama, and Masatoshi Kitamura, "**Structural and Electrical Properties of Fluorinated Copper Phthalocyanine for Organic Photovoltaics**", International Conference on Solid State Devices and Materials (SSDM 2013) Sept 24-27, 2013, Fukuoka, Japan, PS-15-8.

2. Yasutaka Kuzumoto, Hirotaka Matsuyama, and Masatoshi Kitamura, "**Fine Tuning of Energy Levels in Partially Fluorinated Copper Phthalocyanine for Organic Photovoltaics**", 40th International Symposium on Compound Semiconductors (ISCS 2013) May 19-23, 2013, Kobe, Japan, MoPC-09-02.

3. Yasutaka Kuzumoto, Hirotaka Matsuyama, and Masatoshi Kitamura, "**Partially**

Fluorinated Copper Phthalocyanine toward Band Engineering for High-Efficiency Organic Photovoltaics”, 7th International Conference Molecular Electronics and Bioelectronics (M&BE 7) March 17-19, 2012, Fukuoka, Japan, B-O11.

International Conference Related to Other Work

1. Masatoshi Kitamura, Yasutaka Kuzumoto, and Yasuhiko Arakawa, “**Short-Channel, High-Mobility Organic Thin-Film Transistors with Alkylated Dinaphthothienothiophene**”, 40th International Symposium on Compound Semiconductors (ISCS 2013) May 19-23, 2013, Kobe, Japan, TuB1-2.

2. Masakazu Kamura, Yasutaka Kuzumoto, Tetsuji Itoh, Shigeru Aomori, Masatoshi Kitamura, and Yasuhiko Arakawa, “**A Molecular Stacking Technique on the Substrate using Chemical Linkage for Organic Material Devices: Characterization of π-Conjugated Self-Assembled Layer with Oligo-Thiophene Moiety**”, The 37th International Symposium on Compound Semiconductors (iscs2010) May 31-June 4, 2010, Kagawa, Japan, WeE2-6.

3. Masatoshi Kitamura, Yasutaka Kuzumoto, Woogun Kang, Shigeru Aomori, and Yasuhiko Arakawa, “**Low Contact Resistance in Pentacene Thin-Film Transistors using Electrode Modification and Gold-Nickel Adhesion Layers**”, The 37th International Symposium on Compound Semiconductors (ISCS 2010), May 31-June 4, 2010, Kagawa, Japan, WeE2-4.

4. Masakazu Kamura, Shigeru Aomori, Yasutaka Kuzumoto, Hirohiko Houjou, Masatoshi Kitamura, and Yasuhiko Arakawa, “**Control of Molecular Orbital States of Self-Assembled Multilayer Films by Introducing Molecular Structures**”, International Symposium on Quantum Nanophotonics and Nanoelectronics (ISQNN 2009) Nov 18-20, 2009, Tokyo, Japan, WeP-6.

5. Masakazu Kamura, Shigeru Aomori, Yasutaka Kuzumoto, Yoshitaka Tomomura, Hirohiko Houjou, Masatoshi Kitamura, and Yasuhiko Arakawa, “**Fabrication and**

Characterization of pi-Conjugated Azomethine Self-Assembled Multilayers", IEEE Nanotechnology Materials and Devices Conference (NMDC 2008), Oct 20-22, 2008, Kyoto, Japan, WeB I-5.

6. Masatoshi Kitamura, Yasutaka Kuzumoto, Masakazu Kamura, Shigeru Aomori, Jong Ho Na, and Yasuhiko Arakawa, "**Low-Voltage-Operating Fullerene C_{60} Thin-Film Transistors with Various Surface Treatments**", The 34th International Symposium on Compound Semiconductors (ISCS 2007), Oct 15-18, 2007, Kyoto, Japan, TuC P38.

Acknowledgements

I would like to express my sincere gratitude to Associate Professor Masatoshi Kitamura. His advices, encouragement, and understanding greatly helped me to advance my research. Also, his efficient and logical approach toward solving issues in research, professional attitude to work, and teaching way to enhance the research capability of students have been very instructive for me.

I wish to express my deep gratitude to Professor Takashi Kita, Professor Atsunori Mori, and Professor Minoru Fujii, for serving on review committee for this thesis and for their constructive comments and advices about my work.

I greatly acknowledge Professor Yasuhiko Arakawa, The University of Tokyo, for special support to my work.

I express my heartfelt thanks to Dr. Akira Takahashi and Yoshitaka Tomomura, SHARP Corporation, for providing me the great opportunity to study in doctoral course. I would like to thank Dr. Makoto Izumi, SHARP Corporation, for his constructive comment based on his deep knowledge about my research and for his kind support to advance my work. I wish to acknowledge Dr. Masahito Oh-e, SHARP Corporation, for valuable discussions and comments about a basic study that became a basis of my work when I worked in Tokyo University. I also would like to thank Masakazu Kamura, Dr. Tetsuji Itoh, and Shigeru Aomori for fruitful discussions about the basic study. I deeply thank Dr. Katsumi Kondo, SHARP Corporation, for his encouragement to study in doctoral course. I also wish to thank Dr. Masataka Ohta, SHARP Corporation, for introducing me to useful experimental equipment and for giving me operating instruction of it.

I offer warm thanks to Associate Professor Ken Tokunaga, Kogakuin University, for his useful comments on the way of basic interpretation about calculation results.

I give a huge thanks to my colleagues in Kitamura laboratory. I extend deep gratitude to Hirotaka Matsuyama for his experimental assistance and discussion about the results. I owe sincere to Kazuma Katsuki and Yoshinari Kimura who have given me operating instruction of experimental equipments. I extend my thanks to Shouta Takayasu and Shota Mizuka who have given me questions about calculation that lead to improve my calculation skill. I sincerely thank Tetsuya Murakami, Shingo Tatara, Shun Aota, Yoku Tanaka, Shuhei Okuda, and Hiroaki Yamamoto who spent a lot of precious time in their life with me.

Last but not least, I wish to express my deep thanks to all my family; my parents for their numerous supports, my wife for her eternal love and support, my son for giving me a feeling of peace.

Doctor Thesis, Kobe University
“Quantum chemical and experimental study on halogenated copper phthalocyanine for organic photovoltaics application”, 115 pages
Submitted on January, 23rd, 2014
The date of publication is printed in cover of repository version published in Kobe University Repository Kernel.

©Yasutaka Kuzumoto
All Right Reserved, 2014